Astronomy Unit
School of Physics and Astronomy
Queen Mary University of London

Exact, Inhomogeneous Solutions to Gravitational Theories in Cosmology

Jessie Durk

Supervised by Dr. Timothy Clifton

Submitted in partial fulfillment of the requirements of the Degree of Doctor of Philosophy

To my mother, Debbie.
In memoriam. Ad astra.

“The stars look very different today.”

Declaration

I, Jessie Durk, confirm that the research included within this thesis is my own work or that where it has been carried out in collaboration with, or supported by others, that this is duly acknowledged below and my contribution indicated. Previously published material is also acknowledged below.

I attest that I have exercised reasonable care to ensure that the work is original, and does not to the best of my knowledge break any UK law, infringe any third party's copyright or other Intellectual Property Right, or contain any confidential material.

I accept that the College has the right to use plagiarism detection software to check the electronic version of the thesis.

I confirm that this thesis has not been previously submitted for the award of a degree by this or any other university. The copyright of this thesis rests with the author and no quotation from it or information derived from it may be published without the prior written consent of the author.

Details of collaboration and publications: Part of this work is done in collaboration with Timothy Clifton, Rashida Bibi, Eloisa Bentivegna, Mikołaj Korzyński and Kjell Rosquist. I have made a major contribution to the original research presented in this thesis. It is based on the following papers that have been published or submitted for publication:

- Discrete Cosmological Models in the Brans-Dicke Theory of Gravity
  J. Durk and T. Clifton, Submitted for publication in Class. Quantum Grav. Arxiv:1903.03043 [gr-qc]
- Black-Hole Lattices as Cosmological Models
  E. Bentivegna, T. Clifton, J. Durk, M. Korzyński and K. Rosquist,

Class. Quantum Grav. 35 (2018) 175004,
Arxiv:1801.01083 [gr-qc]

- A Quasi-Static Approach to Structure Formation in Black Hole Universes
  J. Durk and T. Clifton, *JCAP 10 (2017) 012*,
  Arxiv:1707.08056 [gr-qc]

- Cosmological Solutions with Charged Black Holes
  R. Bibi, T. Clifton and J. Durk, *Gen. Rel. Grav. 49 (2017) 98*,
  Arxiv:1705.01892 [gr-qc]

- Exact Initial Data for Black Hole Universes with a Cosmological Constant
  J. Durk and T. Clifton, *Class. Quant. Grav. 34 (2017) 065009*,
  Arxiv:1610.05635 [gr-qc]

Signature: Jessie Durk
Date: 21/06/2019

Abstract

Solving the backreaction and averaging problems is important as we enter the era of precision cosmology. Fundamentally, the idea that small-scale inhomogeneities can affect the large-scale dynamics of the Universe lies in the non-linearity and non-commutativity properties of the Einstein field equations. It is not necessarily the case that the dynamics of a perfectly homogeneous Friedmann universe are the same as an inhomogeneous one. However, difficulties arise in finding suitable inhomogeneous solutions to the Einstein field equations. Progress can be made by treating it as an initial data problem and solving the constraint equations. This gives rise to a family of solutions, the black hole lattices, which consist of linearly superposed Schwarzschild masses representing a universe with a discretised matter content. In this thesis, we present extensions and generalisations of these existing models. Firstly, we devised a novel way to include structure formation and its effects. We did this in a quasi-static approach that involved splitting the black holes up into more masses and moving them along parameterised trajectories. For small values of this parameter, we could induce clustering as the black holes were sufficiently close together. We found an extra apparent horizon encompassed the cluster and that in order to reduce backreaction, interaction energies within clustered masses needed to be included. Our next two extensions involved adding in extra fields, either electric charge or the cosmological constant. Finally we considered the lattices in an alternative scalar-tensor gravitational theory, Brans-Dicke. We found our lattices reduced to their relativistic versions in the appropriate limit, but for some values very far from general relativity, we could reduce backreaction to zero by altering the amount of background scalar field. For all of our analyses we found that increasing the number of masses reduces the discrepancy between our lattice cosmologies and continuous counterparts.

Acknowledgements

I would like to begin by thanking my supervisor Timothy Clifton for his continual help and support throughout my PhD and for the opportunity to work in such an exciting and growing field. I would also like to thank the other members of the Astronomy Unit, namely Karim Malik, David Mulryne, Chris Clarkson, Alkistis Pourtsidou, Bernard Carr, Reza Tavakol, Richard Nelson, Phil Bull and David Burgess. Among the wider Queen Mary Physics community I thank Costis Papageorgakis for his help and guidance, Jeanne Wilson for allowing me to contribute to the Equality, Diversity and Inclusivity Committee, and members of the School of Mathematical Sciences.

I wish to thank all of the PhD students in the Astronomy Unit, past and present. I thank former students and office colleagues Sophia Goldberg, Viraj Sanghai, John Ronayne, Pedro Carrilho, Shailee Imrith and Charalambos 'Charlie' Pittordis for their guidance, advice and wisdom. I also thank Kit Gallagher, Louis Coates, Eline de Weerd, Jorge Fuentes, Paul Hallam, John Strachan, Domenico Trotta, Sandy Zeng, Sanson Poon, Clark Baker, Franceso Lovascio, Callum Boocock, Rebeca Carrillo, Jack Skinner, Jesse Coburn, Paula Soares, Alice Giroul and George Montagnon for making my time at Queen Mary so enjoyable.

Outside of Queen Mary, I thank my friends Bex, Saina, Harpreet, Johann, Evan, Oliver, both Sams, Alek and Luci, as well extended friends, Martin, James and Lewis. Sincerest and deepest thanks must be extended to my previous colleagues at the Royal Observatory Greenwich, in particular Liz and Brendan for being so supportive and encouraging, and for giving me such fantastic opportunities. I also thank Hannah, Jo, Affelia, Roman, Tom, Dara, Greg, Ed, Nick and Radmila.

Finally I thank my closest loved ones - all of my family who have made this journey possible. I thank my dad Richard for our days out in London, my brother Sam for being a rock through difficult times and my sister Mia whose resilience inspires me everyday. I thank my auntie Ang for helping the three of us with all that we needed, Nan S and John for their generosity and hospitality, Nan J, my cousins Ella and Leoni, my uncle Danny and auntie Beckie, auntie Liz, and the dog Jeff. I also thank extended family and friends Chris, Bev, Rose, Sally and Sid. Thanks also to Paul, who is forevermore a part of our family.

My gratitude could not be greater for my partner, Tom 'Fletch' Fletcher, who has been by my side during my PhD and always helped me without fail. I thank him for giving up his time to listen to me practise my talks, for travelling with me, and for being my best friend. Without him this journey would not have been possible. I thank his parents Lynn and Peter for their kindness also.

I reserve my final and greatest thanks to my mum, Debbie, for she has selflessly given everything and every part of her to her three children, and encouraged me every step of the way to pursue a PhD and have confidence. I wish her all the strength

and health in the world and can only hope that she gets better. I write this thesis with her in mind, always.

It is not in anyone's imagining that words already written are suddenly no longer appropriate. I retain them as a reminder, and I still write this thesis with her in mind, always, and I will live my life with her in mind, always. This thesis is dedicated to my mum, Debbie, who was always so proud.

This work was supported by the Science and Technology Facilities Council (STFC), grant number ST/N504257/1.

Contents

List of Figures

List of Tables

1 Introduction

Ten years after publishing his theory of special relativity in 1905, Einstein presented a set of equations that would prove revolutionary in our understanding of gravity [4]. These field equations state that matter and spacetime curvature are inextricably linked, with gravity arising as a consequence of the curvature of spacetime, an idea that challenged the previous Newtonian school of thought. Shortly afterwards came the first non-trivial exact solution to the Einstein field equations - the Schwarzschild solution, describing a spherically symmetric spacetime with a vacuum exterior around a spherical mass [5]. This was followed by the addition of electric charge in 1916-18 [6–8], but it was not until 1963 that a solution for rotating black holes was discovered by Kerr [9].

Ever since its inception there has been a wealth of evidence to support Einstein's theory of gravitation, beginning with observations of gravitational lensing during a solar eclipse in 1919 [10], to more recently, observations of gravitational waves from both binary black hole mergers [11] and neutron star mergers [12], decades after gravitational waves were first theorised.

Perhaps the most important and exciting application of general relativity is in cosmology, which aims to understand our entire Universe and its evolution, across a vast range of scales. Finding a suitable solution to the Einstein field equations to describe our Universe, however, has historically presented its own challenges. Einstein proposed the idea of a static universe in 1917 but this became disfavoured as it contradicted findings by Hubble in 1929 [13]. The observed redshift of a galaxy seemed to increase with distance, a phenomena which can be attributed to an expanding universe. Independently, Friedmann, Lemaître, Robertson and Walker (FLRW) had already (or were in the process of) theorised an expanding universe [14–17]. This FLRW solution to the Einstein field equations would underpin modern cosmology and prove fundamental in our understanding of the Universe.

The standard model of cosmology, or ΛCDM concordance model, is the simplest and most successful description of our Universe to date. It assumes that our Universe can be modelled by the spatially homogeneous and isotropic FLRW solution to Einstein's equations on all scales, despite our Universe being only statistically homogeneous

and isotropic on large scales [18]. Furthermore, the large-scale expansion of space is assumed to have these properties as well, however, this has never been proven.

The successes of the standard model of cosmology come from its simplicity - the metric described above results in remarkably simple evolution, or Friedmann, equations that are used to derive observational relations - and its agreement with data. The model is consistent with many results from high precision measurements, from large-scale surveys such as SDSS [19] and DES [20], to CMB measurements, which also inform us that the Universe is spatially flat [21]. The late time accelerated expansion inferred from supernovae observations [22, 23], can be attributed to a simple component, the Λ in ΛCDM, or dark energy. The dark matter that is responsible for galaxy rotation curves is cold, which has implications for the growth of structure. Even the detection of gravitational waves is an independent nod towards our current model of cosmology and the Hubble constant [24].

Despite the success of the standard model of cosmology, it is not without its shortcomings. The dark sector, comprised of dark energy and dark matter, contributes 95% of the overall energy budget of the Universe, yet very little is known about either of these, despite decade long searches. A growing tension between high redshift and local measurements of the value of the Hubble constant, at more than 3σ, points either towards extensions to the standard model of cosmology, or revisiting systematic effects [25]. Finally, the ΛCDM model fails to predict both the observed number and mass of satellite galaxies [26].

A more subtle problem, and one that this thesis aims to address, lies in the Einstein field equations themselves. They are highly non-linear and non-commutative, in that averaging a tensor and calculating the evolution equations do not commute. This begs the question - could the small-scale inhomogeneities that are otherwise ignored in the FLRW solution have an effect on the large-scale dynamics of the Universe? This is known as the backreaction problem in cosmology, and has been the subject of intense debate over the last few years, see [27–29], and also [30, 31].

Observationally this may have implications for the propagation of light, and therefore our interpretations of cosmological observables. This is of particular importance as we enter an era where next generation large-scale surveys, such as Euclid [32] and the LSST [33], will map the Universe to an unprecedented level of precision. Recent studies on the propagation of light in inhomogeneous cosmologies have found differences in cosmological parameters with FLRW predictions by as much as 10% [34].

The standard model of cosmology is based on a spacetime metric that has remained unchanged since its inception nearly a hundred years ago. It is imperative we have

the correct underlying model to interpret future data. Until then, it should not be assumed that the background geometry of our Universe be so simply described. Thus we motivate the study of *inhomogeneous* cosmologies, which this thesis aims to contribute to. Inspired by approaches from relativity and finding exact solutions, we present a family of inhomogeneous cosmologies and investigate their similarities and differences with FLRW universes. Our approach is exact, requires no junction or matching conditions, and is fully relativistic.

In chapter 2 we review general relativity by looking at some of the main foundational assumptions. We also look at alternatives, such as scalar-tensor theories of gravity. Solving the Einstein field equations is no easy feat, therefore we introduce the ADM formalism and 3+1 decomposition techniques as a means of constructing initial data to instead solve the constraint equations. We present some of the existing exact and black hole solutions in chapter 2 also, as well as introducing the topic of inhomogeneous cosmology. This is done by giving a brief outline of the standard model of cosmology before looking at what work has been done so far to solve the backreaction problem, either numerically or analytically, and light propagation within these models.

A subset of inhomogeneous cosmologies, the black hole lattices, are introduced in chapter 3. We review the current literature, from their inception to the present day, and review some of the main calculations that will be referred to again in this chapter also.

Chapter 4 presents one of the generalisations of these lattices by introducing a novel way to add structure. It involves splitting each of the black holes up into a number of further masses and moving them along very well-defined, parameterised trajectories. By altering the value of this parameter we can consider lattices with clusters of black holes, and therefore investigate the cosmological effects of these. We look at different ways to calculate the apparent horizons in these models, the various definitions of mass, and the interaction energies. We find interaction energies appear to be important in reducing the amount of backreaction [35].

The remaining chapters follow a similar format to chapter 4, in that we present the constraint equations if necessary, solve them with an appropriate choice of initial data, before looking at the cosmological effects. Intermediately there may be a calculation of apparent horizons or mass parameters or similar. In chapter 5 we present initial data which solves the constraint equations with a cosmological constant term, Λ. We do this with an appropriate choice of the extrinsic curvature, and find the intrinsic geometry remains unchanged from the $\Lambda = 0$ case. Differences however lie in the location of the apparent horizons, which we calculate, as well as the quantities

we can compare with suitable FLRW counterparts. It turns our the deceleration parameter is one such quantity, and we find that for an increasing number of masses, the deceleration parameter for the lattice universes becomes identical to its FLRW version [36].

In chapter 6 we perform similar calculations but with the addition of electric charge. Again, we present the initial data and focus on a model that contains 8 black holes, the cubic lattice. Our FLRW comparison tells us that backreaction is at its smallest when the black holes are extremal [37].

Finally the last of the generalisations we wish to present can be found in chapter 7. Here we move on from general relativity, to look at a simple scalar-tensor theory of gravity, the Brans-Dicke theory. Our complexity increases twofold - firstly, by choosing to construct inhomogeneous cosmologies over FLRW as we have seen, but secondly, by now extending the gravitational theory to include a scalar field. As a result, very little has been done in the literature regarding this, so we begin by deriving the constraint equations for such a theory. We then solve them with initial data, and interpret the various parameters by comparing to the spherically symmetric Brans solution. We find a parameter that we interpret as controlling the background level of scalar field. We derive expressions for the proper mass and scalar charge, and perform a multilevel comparison. We find that in the general relativistic limit we are able to recover the previous quantities [38].

Finally we conclude all of our findings in chapter 8 as well as stating where this work may lead in the future.

1.1 Notation and Conventions

Throughout this thesis we use the metric signature $(-, +, +, +)$. We use geometrised units where $c = G = 1$, where c is the speed of light and G is the Newtonian gravitational constant. Spacetime coordinates are denoted by Greek indices (μ, ν, ρ) whilst spatial coordinates are denoted by Latin indices (i, j, k). We adopt the Einstein summation convention throughout, where repeated indices are summed over.

2 Background

2.1 General Relativity

Parts of section 2.1.5 are taken from [38] and parts of 2.2.4 are taken from [36] and [35].

2.1.1 Principles of General Relativity

The insight Einstein had regarding gravity and spacetime allowed him to develop his theory of general relativity. The spacetime metric is generalised from special relativity to deviate away from flatness and include curvature. As a result, the gravitational force is instead attributed to the curvature of spacetime. Although conceptually very different to the definition of the Newtonian gravitational force, general relativity is able to reproduce Newtonian gravity in the limit of weak fields and slow velocities, a stringent requirement from solar system tests [39].

The cornerstones of general relativity are the principles of equivalence [40–42]. The Weak Equivalence Principle states that once the initial positions and velocities have been prescribed for uncharged freely falling test particles, then they will follow the same trajectories, independent of internal composition and structure. The Einstein Equivalence Principle follows on from this and states that locally, and up to tidal gravitational forces, the same laws of special relativistic physics are recovered in all freely falling frames, independently of the velocity of the reference frame or location. Finally, the Strong Equivalence Principle extends these to include massive, self-gravitating objects as well as test particles, and that locally, the same laws of special relativistic physics are recovered in all freely falling frames, independently of the position or velocity of the reference frame [43].

Covariance also plays a large role in general relativity, as the laws of physics, and indeed gravity, should be invariant under transformations of coordinate systems. This motivates the use of tensors in general relativity. These provide physically meaningful equations as a tensor equation that holds in one coordinate system is true in another [44].

2.1.2 Differential Geometry

General relativity is a metric theory of gravity where spacetime is described by a 4-dimensional Lorentzian manifold $\mathcal{M}$. The metric tensor $g_{\mu\nu}$ is a symmetric, invertible $(0,2)$ tensor that provides the notion of measurable quantities, such as angles, norms and distances between two spacetime events, $ds^2 = g_{\mu\nu}dx^\mu dx^\nu$, and allows indices to be raised and lowered. Furthermore, the metric $g_{\mu\nu}$ defines in a unique way a metric-compatible covariant derivative ∇_μ on $\mathcal{M}$, the Levi-Civita connection. For a $(1,1)$ tensor it is defined as follows

$$\nabla_\mu T^\nu_\lambda = \partial_\mu T^\nu_\lambda + \Gamma^\nu_{\sigma\mu} T^\sigma_\lambda - \Gamma^\sigma_{\lambda\mu} T^\nu_\sigma, \tag{2.1}$$

where ∂_μ denotes the partial derivative with respect to the spacetime coordinates x^μ and the Christoffel symbols $\Gamma^\mu_{\nu\lambda}$ are defined as

$$\Gamma^\mu_{\nu\lambda} = \frac{1}{2} g^{\mu\rho} \left(\partial_\nu g_{\rho\lambda} + \partial_\lambda g_{\nu\rho} - \partial_\rho g_{\nu\lambda} \right). \tag{2.2}$$

The covariant derivative is torsion free and compatible with the metric, $\nabla_\mu g_{\nu\rho} = 0$. It is the natural generalisation of the partial derivative, from flat or Euclidean space, to curved geometry, and indeed reduces to the partial derivative for a scalar function, and in flat space.

Any spacetime is locally flat, and the quantity that characterises the deviation away from this simple geometry is curvature. The Riemann tensor $R^\mu{}_{\nu\lambda\rho}$ is defined as follows,

$$R^\mu{}_{\nu\lambda\rho} = \partial_\lambda \Gamma^\mu{}_{\nu\rho} - \partial_\rho \Gamma^\mu{}_{\nu\lambda} + \Gamma^\mu_{\lambda\sigma} \Gamma^\sigma{}_{\nu\rho} - \Gamma^\mu_{\rho\sigma} \Gamma^\sigma{}_{\nu\lambda}. \tag{2.3}$$

The Riemann tensor enjoys several symmetry relations and identities,

$$R_{\mu\nu\rho\sigma} = -R_{\nu\mu\rho\sigma}, \quad R_{\mu\nu\rho\sigma} = -R_{\mu\nu\sigma\rho}, \quad R_{\mu\nu\rho\sigma} = R_{\rho\sigma\mu\nu}, \tag{2.4}$$

including the first Bianchi identity,

$$R_{\mu\nu\rho\sigma} + R_{\mu\sigma\nu\rho} + R_{\mu\rho\sigma\nu} = 0, \tag{2.5}$$

and second Bianchi identity,

$$\nabla_\lambda R_{\mu\nu\rho\sigma} + \nabla_\sigma R_{\mu\nu\lambda\rho} + \nabla_\rho R_{\mu\nu\sigma\lambda} = 0. \tag{2.6}$$

Contracting the Riemann tensor once gives the Ricci tensor, $R_{\mu\nu} = R^\rho{}_{\mu\rho\nu}$, whilst

contracting again gives the Ricci scalar $R = R_{\mu\nu}g^{\mu\nu} = R^{\mu}_{\ \mu}$. Finally, by defining the Einstein tensor as $G_{\mu\nu} \equiv R_{\mu\nu} - \frac{1}{2}g_{\mu\nu}R$ we have that the Einstein field equations in the presence of the cosmological constant Λ can be written as

$$\boxed{G_{\mu\nu} + \Lambda g_{\mu\nu} = 8\pi T_{\mu\nu},} \tag{2.7}$$

where we have introduced the stress-energy tensor $T_{\mu\nu}$, which contains all non-gravitational sources of energy, such as radiation, fields and fluids. Thus gravity is a manifestation of the curvature of spacetime, where the presence of mass-energy generates this curvature. Matter moves on timelike geodesics, whilst photons travel along null geodesics. For cosmological applications, such as the expansion of the Universe, the Λ term in Equation (2.7) can be included, but due to its small magnitude it becomes unimportant for black hole studies [1].

Conservation of energy-momentum is implied from the second Bianchi identity and Equation (2.7), as $\nabla_\mu G^{\mu\nu} = 0$ and therefore

$$\nabla_\mu T^{\mu\nu} = 0, \tag{2.8}$$

where the compatibility of the covariant derivative with the metric has also been used.

The Einstein field equations can also be derived using variational principles, where the action for such a theory is given by the Einstein-Hilbert action,

$$S = \frac{1}{16\pi}\int \mathrm{d}^4x\sqrt{-g}(R - 2\Lambda) + \int \mathrm{d}^4x\sqrt{-g}\mathcal{L}_m, \tag{2.9}$$

where g is the determinant of the metric and $\mathcal{L}_m$ is the matter Lagrangian density. The only dynamical field is the metric tensor $g_{\mu\nu}$, which means varying the action with respect to the metric results in the Einstein field equations above.

2.1.3 Birkhoff's Theorem

Birkhoff's theorem is used to understand the gravitational field around isolated masses. It states that, in the absence of a cosmological constant, all asymptotically flat, spherically symmetric solutions of the vacuum Einstein field equations are static [45]. Asymptotic flatness means the spacetime becomes increasingly Minkowskian at spatial infinity, meaning the curvature vanishes. The geometry of such a spacetime is given by the Schwarzschild solution, which has a line element in standard Schwarzschild

coordinates as

$$ds^2 = -\left(1 - \frac{2m}{r}\right) dt^2 + \left(1 - \frac{2m}{r}\right)^{-1} dr^2 + r^2(d\theta^2 + \sin^2\theta d\phi^2), \tag{2.10}$$

where m is the mass of the object. The Schwarzschild spacetime can be described by several different coordinate systems. One of the most widely used of these is isotropic coordinates, which can be obtained by introducing an isotropic radial coordinate ρ as $r = \rho\left(1 + \frac{m}{2\rho}\right)^2$. This gives the line element in Equation (2.10) as being

$$ds^2 = -\left(\frac{1 - m/2\rho}{1 + m/2\rho}\right)^2 dt^2 + \left(1 + \frac{m}{2\rho}\right)^4 (d\rho^2 + \rho^2 d\theta^2 + \rho^2 \sin\theta^2 d\phi^2). \tag{2.11}$$

We will refer back to this particular line element in subsequent chapters when we construct the black hole lattices.

The Schwarzschild metric is a solution to the vacuum Einstein field equations and represents a spherically symmetric spacetime surrounding a mass, and by virtue of Birkhoff's theorem, can be applied to the vacuum exterior of static or collapsing stars. Birkhoff's theorem is not valid in many alternative gravitational theories however. An example is the *non-static* spherically symmetric vacuum solution to the scalar-tensor Brans-Dicke theory [46], which we introduce more in section 2.1.5.

2.1.4 Lovelock's Theorem

Lovelock's theorem is important in providing a stepping stone towards constructing alternative theories of gravity. It states that if we wish to construct a second-order 4-dimensional theory using only the metric tensor in the Lagrangian, then the resulting field equations are those of Einstein, with or without a cosmological constant [47, 48]. Consequently, if we seek a theory with different field equations, then we must do at least one of the following [46]:

- Include additional fields, such as scalar, vector or tensor.
- Include higher than second-order derivatives of the metric in the field equations.
- Allow more than 4 spacetime dimensions.
- Discard either rank-2 tensor field equations, their symmetries, or conservation laws.
- Allow non-locality.

The first of these points is the most natural way of extending the theory of relativity, and we will explain scalar-tensor theories in particular in the next section.

2.1.5 Scalar-Tensor Theories of Gravity

The only dynamical gravitational variable in general relativity is the metric tensor $g_{\mu\nu}$. Additional fields, such as scalar, vector or tensor can also be added by introducing a non-minimal coupling between the additional field and gravity. In order to pass solar system tests, these couplings need to either be weak, or involve screening mechanisms such that the effects of the additional field are not seen on solar system scales [46]. Cosmologically, one of the biggest motivations for studying the effects of extra fields is that they give can rise to the late time accelerated expansion of the Universe without the need for dark energy [49].

The simplest addition is naturally a scalar field, giving rise to a class of theories called scalar-tensor theories. Scalar-tensor theories of gravity are also among the oldest and best studied generalisations of Einstein's theory. They were originally introduced by Jordan in 1949 [50, 51], before being refined by Brans and Dicke in 1961 [52] and then being generalized to theories with arbitrary coupling parameters by Bergmann [53], Wagoner [54] and Nordtvedt [55]. They can be seen to contain the dimensionally reduced theories that one recovers from string theory [56], as well as the canonical version of the Horndeski class of scalar-tensor theories that have recently found popularity in cosmology [57]. Phenomenologically, scalar-tensor theories of gravity have found application in modelling the possible variations of the constants of nature [58, 59], as well as providing the archetypal class of theories that are used to quantify allowed deviations from Einstein's theory [43].

Usually, the coupling parameter is an arbitrary function of the scalar field. However, if one sets it to a constant value, one recovers the simplest example of a scalar-tensor theory, the Brans-Dicke theory. This has a Lagrangian density given by [46]

$$\mathcal{L} = \frac{1}{16\pi}\sqrt{-g}\left(\phi R - \frac{\omega}{\phi}\nabla_\mu\phi\nabla^\mu\phi\right) + \mathcal{L}_m(g_{\mu\nu},\psi), \tag{2.12}$$

where $g_{\mu\nu}$ is the metric, ϕ is the scalar field, ω is the constant coupling parameter of the theory, and $\mathcal{L}_m(g_{\mu\nu},\psi)$ is the Lagrangian density of the matter fields, ψ. The non-minimal coupling between ϕ and R results in new gravitational phenomena, while the coupling of only $g_{\mu\nu}$ to ψ ensures that the Einstein Equivalence Principle is maintained.

Varying the resulting action with respect to the metric $g_{\mu\nu}$, gives the following

field equations:

$$\phi\, G_{\mu\nu} + \left(\Box\phi + \frac{\omega}{2\phi}(\nabla\phi)^2\right) g_{\mu\nu} - \nabla_\mu\nabla_\nu\phi - \frac{\omega}{\phi}\nabla_\mu\phi\nabla_\nu\phi = 8\pi\, T_{\mu\nu}, \tag{2.13}$$

while varying with respect to the scalar field ϕ, yields

$$\Box\phi = \frac{8\pi\, T}{(3+2\omega)}, \tag{2.14}$$

where $T_{\mu\nu}$ are the components of the energy-momentum tensor, and T is its trace. The locally measured gravitational 'constant' in these theories can then be shown to be given by

$$G = \frac{(4+2\omega)}{(3+2\omega)}\frac{1}{\phi}, \tag{2.15}$$

and hence can vary in spacetime whenever ϕ is non-constant. These equations can be seen to reduce to Einstein's theory in the limit $\omega \to \infty$, when $\phi \to$ constant and Equation (2.13) reduces to Einstein's equations [60].

The Brans-Dicke theory of gravity will be considered in chapter 7 where we will use it to construct inhomogeneous cosmological models.

2.2 Solving the Einstein Field Equations

The problem of finding solutions to the Einstein field equations can be tackled by treating it as an initial value, or Cauchy problem, inspired by mathematical treatments of partial differential equations. In its 4-dimensional covariant form there are ten non-linear second-order partial differential equations to solve. Progress is instead made by slicing the 4-dimensional manifold into layers of 3-dimensional spatial hypersurfaces which foliate the spacetime and build up along a 1-dimensional time direction. This is known as the 3+1, or Arnowitt-Deser-Misner (ADM) decomposition. The gravitational field then obeys both what are known as the constraint and evolution equations. The constraint equations must be satisfied by the initial data (the spatial hypersurfaces) at an initial time. The evolution equations describe how this data evolves in time to give the full spacetime. It turns out that this picture is completely equivalent to the field equations of general relativity. Much of the early work can be attributed to Darmois [61], Lichnerowicz [62] and Foures-Bruhat [63], as well as Arnowitt et al [64], of which the equations bear their name. Choquet-Bruhat's pioneering work showed that indeed the initial value problem described above is well-posed, meaning given some initial data, the solution to the evolution equations

is uniquely determined by this initial data [65, 66].

In this section we review the 3+1 decomposition of general relativity and derive the constraint and evolution equations. We review approaches used to construct initial data in order to solve the constraint equations as well as give a few examples. An alternative approach is the orthonormal frame, or tetrad, approach, which contains the ADM constraint and evolution equations as a subset. We will briefly review this approach and how it is used to locate the apparent horizons of black holes.

2.2.1 3 + 1 Description

We follow the notation and derivations given in [1], [67] and [68]. We denote a 4-dimensional spacetime manifold by $\mathcal{M}$ and its metric by $g_{\mu\nu}$. Our aim is to express the curvature quantities in the 4-dimensional manifold into 3-dimensional quantities, which will give us the constraint and evolution equations. The spacetime $\mathcal{M}$ is foliated by spacelike hypersurfaces, or time slices, Σ_t, where $t \in \mathbb{R}$, which are non-intersecting and $\mathcal{M} = \bigcup_{t\in\mathbb{R}} \Sigma_t$. Σ_0 is the initial hypersurface on which the initial data is prescribed. The scalar function t can be thought of as a global time function as the hypersurfaces are the surfaces of constant t, or level surfaces of t, see Figure 2.1.

We can define a covector

$$\omega_\mu = \nabla_\mu t, \tag{2.16}$$

which is closed by definition, $\nabla_{[\mu}\omega_{\nu]} = \nabla_{[\mu}\nabla_{\nu]}t = 0$. We can use this to define the lapse function α via

$$g^{\mu\nu}\omega_\mu\omega_\nu \equiv -\frac{1}{\alpha^2}, \tag{2.17}$$

which measures how much time has elapsed between two adjacent time slices along the normal vector ω^μ, where $\omega^\mu = \nabla^\mu t$. The sign of the lapse function is $\alpha > 0$ such that ω_μ is timelike and the hypersurfaces Σ_t are spacelike everywhere.

We can define a unit normal vector n^μ as

$$n^\mu \equiv -\alpha\omega^\mu, \tag{2.18}$$

where n^μ is normalised and timelike such that $n^\mu n_\mu = -1$. We can interpret this unit normal as the 4-velocity of an observer whose worldlines are normal to the hypersurfaces.

A 3-dimensional spatial metric $h_{\mu\nu}$ is induced on the hypersurfaces by the metric

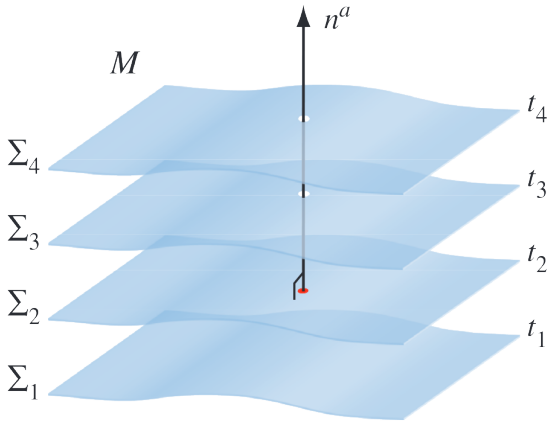

Figure 2.1: A manifold $\mathcal{M}$ foliated by surfaces Σ_t of constant time t. The unit normal here is denoted by n^a. This figure is taken from Numerical Relativity by Baumgarte and Shapiro [1], and is reproduced with permission of Cambridge University Press through PLSclear.

$g_{\mu\nu}$ as follows,

$$h_{\mu\nu} = g_{\mu\nu} + n_\mu n_\nu. \tag{2.19}$$

This metric lives completely within the hypersurfaces, and so is purely spatial, having no component along n^μ. To see this, we contract the metric with the unit normal as

$$n^\mu h_{\mu\nu} = n^\mu g_{\mu\nu} + n_\mu n^\mu n_\nu = n_\nu - n_\nu = 0. \tag{2.20}$$

Similarly the inverse 3-metric is defined as

$$h^{\mu\nu} = g^{\mu\nu} + n^\mu n^\nu. \tag{2.21}$$

The 3-metric is a projection tensor that projects out all geometric objects along n^μ. In order to perform the 3+1 decomposition, we contract with the unit normal to decompose quantities into a temporal part, and contract with the 3-metric to decompose quantities into a spatial part. The two projection operators that do this are formed by raising one index of the 3-metric,

$$h^\mu_{\ \nu} = g^\mu_{\ \nu} + n^\mu n_\nu = \delta^\mu_{\ \nu} + n^\mu n_\nu, \tag{2.22}$$

for the spatial projection, and defining

$$N^\mu_{\ \nu} = -n^\mu n_\nu = \delta^\mu_{\ \nu} - h^\mu_{\ \nu}, \tag{2.23}$$

for the temporal projection. Thus any object can be decomposed into its spatial and temporal parts, for example, consider the following arbitrary vector,

$$v^\mu = \delta^\mu_{\ \nu} v^\nu = (h^\mu_{\ \nu} + N^\mu_{\ \nu}) v^\nu = h^\mu_{\ \nu} v^\nu - n^\mu n_\nu v^\nu. \tag{2.24}$$

The 3-metric $h_{\mu\nu}$ uniquely defines a covariant derivative D_μ which for a scalar ϕ is defined as

$$D_\mu \phi \equiv h_\mu^{\ \nu} \nabla_\nu \phi, \tag{2.25}$$

and for a $(1,1)$ tensor is

$$D_\mu T_\nu^{\ \rho} \equiv h_\mu^{\ \alpha} h_\beta^{\ \rho} h_\nu^{\ \gamma} \nabla_\alpha T_\gamma^{\ \beta}. \tag{2.26}$$

This covariant derivative is torsion free and compatible with the metric, $D_\mu h_{\nu\rho} = 0$. It has an associated 3-dimensional curvature tensor $\mathcal{R}^\rho_{\ \sigma\mu\nu}$, defined as

$$D_\mu D_\nu v^\rho - D_\nu D_\mu v^\rho = \mathcal{R}^\rho_{\ \sigma\mu\nu} v^\sigma, \tag{2.27}$$

where $\mathcal{R}^\rho_{\ \sigma\mu\nu} n^\sigma = 0$. This tensor can be contracted to give the corresponding Ricci tensor, $\mathcal{R}_{\mu\nu} \equiv \mathcal{R}^\rho_{\ \mu\rho\nu}$, and Ricci scalar $\mathcal{R} \equiv g^{\mu\nu}\mathcal{R}_{\mu\nu} = \mathcal{R}^\mu_{\ \mu}$, of the associated 3-space.

Extrinsic Curvature

The 3-dimensional Riemann tensor $\mathcal{R}^\rho_{\ \sigma\mu\nu}$ introduced above measures the intrinsic curvature of the hypersurfaces Σ_t. It contains no information about how these are embedded in the full 4-dimensional spacetime manifold $\mathcal{M}$. Here we will introduce exactly this missing quantity, the extrinsic curvature. Together this forms the initial data that will satisfy the constraint equations. The metric $h_{\mu\nu}$ and the extrinsic curvature $K_{\mu\nu}$ are known as the first and second fundamental forms of the spacetime, respectively.

The extrinsic curvature measures the rate of deformation of the hypersurfaces along the unit normal, see Figure 2.2, and is defined as follows,

$$K_{\mu\nu} \equiv -h_\mu^{\ \rho} h_\nu^{\ \sigma} \nabla_{(\rho} n_{\sigma)} = -h_\mu^{\ \rho} h_\nu^{\ \sigma} \nabla_\rho n_\sigma. \tag{2.28}$$

From this we can define the mean curvature K as

$$K \equiv g^{\mu\nu} K_{\mu\nu} = h^{\mu\nu} K_{\mu\nu}, \tag{2.29}$$

which we note is just the trace of $K_{\mu\nu}$. Finally the extrinsic curvature is transverse, that is, $K_{\mu\nu} n^\nu = 0$.

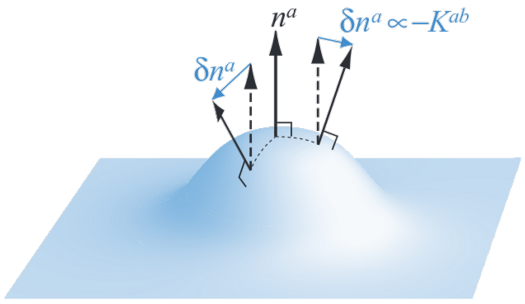

Figure 2.2: Diagram showing the extrinsic curvature measuring the rate of change of the hypersurface along the unit normal n^a. This figure is taken from Numerical Relativity by Baumgarte and Shapiro [1], and is reproduced with permission of Cambridge University Press through PLSclear.

2.2.2 ADM Constraint and Evolution Equations

We are now ready to derive the ADM constraint and evolution equations. First we need to relate the 3-dimensional curvature tensor to the 4-dimensional curvature tensor, and do this by first spatially projecting the 4-dimensional Riemann tensor. Using the previous definitions, we can write

$$D_\mu D_\nu v^\rho = h_\mu^{\ \alpha} h_\nu^{\ \beta} h_\gamma^{\ \rho} \nabla_\alpha \nabla_\beta v^\gamma - K_{\mu\nu} h_\gamma^{\ \rho} n^\alpha \nabla_\alpha v^\gamma - K_\mu^{\ \rho} K_{\nu\alpha} v^\alpha. \tag{2.30}$$

Using Equation (2.27) to introduce the second term on the left-hand side, this gives

$$\mathcal{R}_{\mu\nu\rho\sigma} + K_{\mu\rho} K_{\nu\sigma} - K_{\mu\sigma} K_{\rho\nu} = h_\mu^{\ \alpha} h_\nu^{\ \beta} h_\rho^{\ \gamma} h_\sigma^{\ \delta} R_{\alpha\beta\gamma\delta}, \tag{2.31}$$

which is known as the Gauss-Codazzi equation. This can be contracted to give

$$h^{\mu\rho} h_\beta^{\ \nu} h_\delta^{\ \sigma} R_{\mu\nu\rho\sigma} = \mathcal{R}_{\beta\delta} + K K_{\beta\delta} - K_\delta^{\ \gamma} K_{\gamma\beta}. \tag{2.32}$$

Further contracting gives

$$h^{\mu\rho} h^{\nu\sigma} R_{\mu\nu\rho\sigma} = \mathcal{R} + K^2 - K_{\mu\nu} K^{\mu\nu}. \tag{2.33}$$

Expanding out the left-hand side gives

$$\begin{aligned} h^{\mu\rho} h^{\nu\sigma} R_{\mu\nu\rho\sigma} &= \left(g^{\mu\rho} + n^\mu n^\rho\right)\left(g^{\nu\sigma} + n^\nu n^\sigma\right) R_{\mu\nu\rho\sigma} \\ &= R + 2 n^\mu n^\rho R_{\mu\rho} \end{aligned} \tag{2.34}$$

where we have omitted the last term, $n^\mu n^\nu n^\rho n^\sigma R_{\mu\nu\rho\sigma} = 0$, due to the symmetry properties of the Riemann tensor, i.e. $R_{\mu\nu\rho\sigma} = -R_{\nu\mu\rho\sigma}$. We can now use the Einstein field equation, Equation (2.7), to eliminate the 4-dimensional Riemann tensor. Doing this gives

$$\begin{aligned} 2n^\mu n^\nu G_{\mu\nu} &= 2n^\mu n^\nu R_{\mu\nu} - n^\mu n^\nu g_{\mu\nu} R \\ &= 2n^\mu n^\nu R_{\mu\nu} + R \\ &= h^{\mu\rho} h^{\nu\sigma} R_{\mu\nu\rho\sigma} \\ &= \mathcal{R} + K^2 - K_{\mu\nu} K^{\mu\nu}. \end{aligned} \tag{2.35}$$

Relating this to the stress energy tensor $T_{\mu\nu}$, where we define the total energy density as $\rho \equiv n_\mu n_\nu T^{\mu\nu}$, finally gives the first constraint equation as

$$\mathcal{R} + K^2 - K_{\mu\nu} K^{\mu\nu} = 16\pi\rho. \tag{2.36}$$

This is known as the **Hamiltonian constraint**.

There is one more constraint equation, where the derivation begins by projecting the 4-dimensional Riemann tensor along the normal direction to obtain $D_\mu K_{\nu\rho} = h_\mu^{\ \alpha} h_\nu^{\ \beta} h_\rho^{\ \gamma} \nabla_\alpha K_{\beta\gamma}$. This can be manipulated to give

$$D_\nu K_{\mu\rho} - D_\mu K_{\nu\rho} = h_\mu^{\ \alpha} h_\nu^{\ \beta} h_\rho^{\ \gamma} n^\delta R_{\alpha\beta\gamma\delta}, \tag{2.37}$$

which is known as the Codazzi-Mainardi equation. As before, this can be contracted to give

$$D^\nu K_{\mu\nu} - D_\mu K = h_\mu^{\ \alpha} h^{\beta\gamma} n^\delta R_{\alpha\beta\gamma\delta}. \tag{2.38}$$

Expanding out the right-hand side gives

$$\begin{aligned} h_\mu^{\ \alpha} h^{\beta\gamma} n^\delta R_{\alpha\beta\gamma\delta} &= -h_\mu^{\ \alpha} (g^{\beta\gamma} + n^\beta n^\gamma) n^\delta R_{\alpha\beta\gamma\delta} \\ &= -h_\mu^{\ \alpha} n^\delta R_{\alpha\delta}, \end{aligned} \tag{2.39}$$

where again the last term vanishes due to the symmetries of the Riemann tensor. Utilising the Einstein field equation (2.7) again we have

$$h_\mu^{\ \alpha} n^\delta G_{\alpha\delta} = h_\mu^{\ \alpha} n^\delta R_{\alpha\delta} - \frac{1}{2} h_\mu^{\ \alpha} n^\delta g_{\alpha\delta} R. \tag{2.40}$$

The last term can vanish due to $h_{\mu\delta} n^\delta = 0$, and once again, relating this result to the stress-energy tensor by defining $S_\mu = -h_\mu^{\ \alpha} n^\delta T_{\alpha\delta}$ we have the second constraint

equation,

$$D^\nu K_{\mu\nu} - D_\mu K = 8\pi S_\mu. \tag{2.41}$$

This is known as the **momentum constraint**, where S_μ is the momentum density measured by a normal observer. Both constraint equations involve the spatial metric, the extrinsic curvature, and spatial derivatives for both of these. In order for a set of initial data to be a solution to the Einstein field equations, it must satisfy these equations. In order to completely specify the full spacetime, information about how this initial data evolves is needed, and hence one can solve the evolution equations as well.

Adapted Coordinates

General expressions for the evolution equations involve Lie derivatives, which we will not state here, see [1] for details. Instead we can choose adapted coordinates such that this Lie derivative reduces to the partial derivative and the spatial metric is simply the spatial part of the metric tensor $g_{\mu\nu}$. In these coordinates, the spacetime metric can be written as

$$ds^2 = -\alpha^2 dt^2 + h_{ij}(dx^i + \beta^i dt)(dx^j + \beta^j dt), \tag{2.42}$$

which is known as the 3+1 form of the metric. Here α is the lapse function from before and β^i is the shift vector, which measures how much the spatial coordinates have shifted within a time slice. The lapse and shift are arbitrary and represent the coordinate freedom in the Einstein field equation manifesting as a gauge freedom in the ADM equations. This can be seen by realising that the lapse function is the choice of separation of time slices whilst the shift vector is the choice in relabelling the spatial coordinates arbitrarily.

The full set of constraint and evolution equations in these adapted coordinates, where the 3+1 decomposition naturally reveals a spatial part of the metric, are given by,

$$\mathcal{R} + K^2 - K_{ij}K^{ij} = 16\pi\rho, \tag{2.43}$$

$$D^j K_{ij} - D_i K = 8\pi S_i, \tag{2.44}$$

$$\begin{aligned}\partial_t K_{ij} = &-D_i D_j \alpha + \alpha(R_{ij} - 2K_{ik}K^k_{\ j} + K K_{ij}) \\ &- 8\pi\alpha(S_{ij} - \frac{1}{2}h_{ij}(S-\rho)) + \beta^k D_k K_{ij} \\ &+ K_{ik}D_j\beta^k + K_{kj}D_i\beta^k,\end{aligned} \tag{2.45}$$

$$\partial_t h_{ij} = -2\alpha K_{ij} + D_i\beta_j + D_j\beta_i, \tag{2.46}$$

where we have also defined the spatial stress and its trace respectively as

$$S_{ij} \equiv h_{ik}h_{jl}T^{kl}, \quad S \equiv h^{ij}S_{ij} = S^{i}_{\ i}. \tag{2.47}$$

Equation (2.45) is the evolution equation for the extrinsic curvature K_{ij} and Equation (2.46) is the evolution equation for the spatial metric h_{ij}.

2.2.3 Initial Data

In principle, Equations (2.43) and (2.44) can still be difficult to solve. Therefore we will now look at some of the approaches used to construct initial data that solves constraint equations. These include the main conformal approach of Lichnerowicz and York [62, 69], which forms the focus of this thesis, the conformal thin sandwich approach, gluing constructions, and the Friedrich-Butscher perturbative approach.

Conformal Method

This method is based on a conformal transformation of the spatial metric. Two metrics h_{ij} and $\tilde{h}_{ij}$ are said to be conformally related if there exists a conformal factor ψ such that

$$h_{ij} = \psi^4 \tilde{h}_{ij}. \tag{2.48}$$

The transformation for the inverse metric is then $h^{ij} = \psi^{-4}\tilde{h}^{ij}$. The corresponding connection coefficients, Riemann curvature tensor, Ricci tensor and scalar also transform, the latter being

$$\mathcal{R} = \psi^{-4}\tilde{\mathcal{R}} - 8\psi^{-5}\tilde{D}^2\psi, \tag{2.49}$$

where $\tilde{\mathcal{R}}$ is the Ricci scalar associated with the conformal metric $\tilde{h}_{ij}$ and $\tilde{D}^2$ is the covariant Laplacian also associated with this metric. Inserting this expression into Equation (2.43) gives the Hamiltonian constraint as

$$8\tilde{D}^2\psi - \psi\tilde{\mathcal{R}} - \psi^5 K^2 + \psi^5 K_{ij}K^{ij} = -16\pi\psi^5\rho. \tag{2.50}$$

This equation can be thought of as an equation for the conformal factor ψ, but is highly non-linear in ψ. A simplification can be made if one chooses a vacuum solution, such that the right-hand side is zero, and vanishing extrinsic curvature. Physically this corresponds to hypersurfaces at a moment of time symmetry, or time-symmetric slices. To see this, one can use adapted coordinates and consider the form

of the spatial metric evolution equation (2.46). Provided the shift vector vanishes, a time-symmetric metric has $\partial_t h_{ij} = 0$ which implies $K = K_{ij} = 0$ everywhere. The momentum constraint Equation (2.44) is solved trivially and the Hamiltonian constraint becomes

$$\tilde{D}^2\psi = \frac{\tilde{\mathcal{R}}}{8}\psi, \tag{2.51}$$

which is a linear, Helmholtz equation for ψ. Further simplifications can be made by taking the conformal metric $\tilde{h}_{ij}$ to be the metric of a 3-sphere. This is exactly what we will do in order to construct our black hole lattices, which are explained further in chapter 3.

The 3-sphere is the higher dimensional equivalent of the 2-sphere, which means we can relate the Cartesian coordinates in a 4-dimensional Euclidean embedding space to hyperspherical coordinates on a unit 3-dimensional sphere within that space as follows [3]:

$$\begin{aligned} w &= \cos\chi, \\ x &= \sin\chi\cos\theta, \\ y &= \sin\chi\sin\theta\cos\phi, \\ z &= \sin\chi\sin\theta\sin\phi. \end{aligned} \tag{2.52}$$

Thus the metric of a unit 3-sphere in these hyperspherical coordinates (χ, θ, ϕ) is given by

$$ds^2 = d\chi^2 + \sin^2\chi d\theta^2 + \sin^2\chi\sin^2\theta d\phi^2, \tag{2.53}$$

which has $\tilde{\mathcal{R}} = 6$. A general expression for the covariant Laplacian on the left hand side of Equation (2.51) is given by

$$\tilde{D}^2\psi = \frac{1}{\sqrt{\tilde{h}}}\frac{\partial}{\partial x^i}\left(\sqrt{\tilde{h}}\tilde{h}^{ij}\frac{\partial\psi}{\partial x^j}\right), \tag{2.54}$$

where $\tilde{h}$ is the determinant of the metric tensor h_{ij}, given in Equation (2.53).

Alternatively one can consider initial data with non-zero extrinsic curvature. In that case, one makes use of the conformal-transverse-traceless decomposition as a way to proceed. We have already introduced the conformal transformation in Equation (2.48), but one can also decompose the extrinsic curvature into its trace and trace-free parts, K and A_{ij}, as follows

$$K_{ij} = \frac{1}{3}h_{ij}K + A_{ij}. \tag{2.55}$$

Relating this to their conformal quantities gives

$$K_{ij} = \frac{1}{3}\tilde{h}_{ij}K + \psi^{-2}\tilde{A}_{ij}. \tag{2.56}$$

Substituting this and Equation (2.49) into the constraint Equations (2.43) and (2.44) gives

$$8\tilde{D}^2\psi - \psi\tilde{\mathcal{R}} - \frac{2}{3}\psi^5 K^2 + \psi^{-7}\tilde{A}_{ij}\tilde{A}^{ij} = -16\pi\psi^5\rho \tag{2.57}$$

$$\tilde{D}_i\tilde{A}^{ij} - \frac{2}{3}\psi^6\tilde{h}^{ij}\tilde{D}_i K = 8\pi\psi^{10}S^j. \tag{2.58}$$

These equations can be simplified by choosing to consider vacuum initial data such that the right-hand sides vanish, and by taking the conformal metric to be flat such that $\tilde{\mathcal{R}} = 0$. The resulting equations are highly non-linear in ψ and therefore progress can be made numerically. We review some of this work in chapter 3.

Conformal Thin Sandwich Method

This approach is similar to the previous conformal method, having been devised by York [70] but incorporates some degree of time evolution in specifying the initial data, and therefore is useful in simulating binary black hole collisions, for example [71]. Its name arises from prescribing the spatial metric on two time slices, instead of the metric and extrinsic curvature. On the second slice, the metric is weighted by a velocity tensor $u_{ij} = \dot{h}_{ij}$. The evolution equation for the spatial metric is then used, which contains the shift vector β^i. In this method therefore, the lapse and shift appear, whereas previously they were a completely independent choice. The lapse is given by the conformal transformation and the shift is given by solving the constraint equations. Suitable gauge conditions can then be chosen for numerical integration, for example, the geodesic slicing condition has $\alpha = 1$ and $\beta^i = 0$.

Gluing Methods

The gluing methods use existing solutions to construct new solutions to the constraint equations. [72]. Given two existing solutions $(\mathcal{M}_1, h_{ij\,1}, K_{ij\,1})$ and $(\mathcal{M}_2, h_{ij\,2}, K_{ij\,2})$, spherical regions around two points p_1 and p_2 are removed and conformally blown up into cylinders which are joined together. One then tries to find initial data on this new manifold that solves the constraint equations. This is known as IMP gluing, after Isenberg, Mazzeo and Pollack [73, 74]. An application of this method includes multi-black hole data sets, where the cylindrical region contains a minimal surface

and therefore apparent horizon [75]. There also exists the Corvino-Schoen method [76, 77], which is used to connect an interior region in an asymptotically Euclidean solution to an exterior Kerr or Schwarzschild solution.

Friedrich-Butscher Perturbative Method

As well as the Hamiltonian and momentum constraint equations, one can also project the second Bianchi identity onto the hypersurface, giving a set of two more equations [78]. Together these four equations form the extended constraint equations, which themselves are a subset of the full conformal constraint equations by Friedrich [79]. A perturbative approach is then used to generate solutions to these in the neighbourhood of known solutions. Recently this approach was used to look at non-linear perturbations of initial data in spatially closed analogues of the $k = -1$ FLRW spacetime [80].

2.2.4 Orthonormal Frame/Tetrad Description

The 3+1 decomposition can be thought of as a subset of a much larger group of equations, the orthonormal frame or tetrad approach, which are a complete set of equations. Analysing a problem using this orthonormal frame approach can offer more insight and may be useful in systems where preferred directions are needed. In this thesis, we will use this approach to calculate the position of the apparent horizons of the black holes. We will start by outlining a few basics of the orthonormal frame approach before applying it to locate the horizons.

We begin by considering a preferred timelike vector on the spacetime manifold, which allows us to define a unit timelike vector denoted $u^\mu = e^\mu_0$. We can then introduce three orthogonal spacelike unit vectors, $\{e^\mu_1, e^\mu_2, e^\mu_3, \}$, which together with u^μ complete our orthonormal frame.

The covariant derivative of the unit timelike vector can be decomposed as

$$\nabla_\mu u_\nu = -u_\mu \dot{u}_\nu + \sigma_{\mu\nu} + \frac{1}{3}\Theta h_{\mu\nu} - \omega_{\mu\nu}, \tag{2.59}$$

where $\dot{u}_\mu \equiv u^\nu \nabla_\nu u^\mu$ is the acceleration vector, $\sigma_{\mu\nu} \equiv \dot{u}_{(\mu} u_{\nu)} + \nabla_{(\mu} u_{\nu)} - \frac{1}{3}\Theta h_{\mu\nu}$ is the symmetric and trace free shear tensor, $\Theta \equiv \nabla_\mu u^\mu$ is the expansion scalar and $\omega_{\mu\nu} \equiv -u_{[\mu}\dot{u}_{\nu]} - \nabla_{[\mu} u_{\nu]}$ is the antisymmetric vorticity tensor. The magnitudes of these can be defined accordingly, as well as rotation and commutation relations for the orthonormal frame vectors.

Lastly, we will introduce the Weyl tensor, which is the trace free part of the

Riemann tensor (recall that the Ricci tensor is the trace part). In 4 dimensions it is given by [1]

$$C_{\mu\nu\rho\sigma} = R_{\mu\nu\rho\sigma} - \frac{1}{2}(g_{\mu\rho}R_{\nu\sigma} - g_{\mu\sigma}R_{\nu\rho} - g_{\nu\rho}R_{\mu\sigma} + g_{\nu\sigma}R_{\mu\rho}) + \frac{1}{6}(g_{\mu\rho}R_{\nu\sigma} - g_{\mu\sigma}R_{\nu\rho})R, \tag{2.60}$$

which is invariant under conformal transformations of the metric, vanishes if and only if the metric is conformally flat, and in vacuum spacetimes is equal to the Riemann tensor. The Weyl tensor can be decomposed into its electric and magnetic parts respectively,

$$E_{\mu\nu} \equiv C_{\mu\nu\rho\sigma}u^{\rho}u^{\sigma}, \tag{2.61}$$

$$H_{\mu\nu} \equiv \frac{1}{2}\epsilon_{\mu\rho\sigma}C^{\rho\sigma}{}_{\nu\tau}u^{\tau}. \tag{2.62}$$

The electric part contains information about tidal forces due to gravity, whilst the frame dependent magnetic part contains other information, for example, gravitational radiation or frame dragging.

The idea now is to use the quantities defined and the relations for the frame vectors to rewrite the field equations and the Jacobi and Bianchi identities. This gives rise to the orthonormal frame equations [81].

Time-Symmetric Hypersurfaces

We will now link our initial data for the hypersurfaces to the orthonormal frame approach and show that we arrive at the same constraint equations. We follow the derivation in [82]. We first choose the first term on the right-hand side of Equation (2.59) to vanish, i.e. $\dot{u}^{\mu} = 0$. Then, our choice of a time-symmetric hypersurface means we are considering the transformation $u^{\mu} \to -u^{\mu}$. We require quantities to be invariant under this and so set to zero quantities that are not. From Equation (2.59), none of the terms satisfy this and so we can set the shear tensor, the expansion scalar and the vorticity tensor to be zero. A relevant field equation from [81],

$$0 = -\frac{1}{3}\Theta^2 + \sigma^2 - \omega^2 - 2\omega_{\mu}\Omega^{\mu} - \frac{1}{2}\mathcal{R}, \tag{2.63}$$

where $\mathcal{R}$ is the trace part of the Ricci tensor $\mathcal{R}_{\mu\nu}$ of spacelike 3-surfaces orthogonal to u^{μ}, and Ω^{μ} is the angular velocity of the spatial frame vectors, tells us that $\mathcal{R} = 0$, which we identify as the Hamiltonian constraint from the 3+1 approach. Another

relevant constraint for the electric part of the Weyl tensor from [81] is

$$E_{\mu\nu} = \frac{1}{3}\Theta\sigma_{\mu\nu} - \sigma_{\mu\rho}\sigma^{\rho}_{\ \nu} - \omega_{\mu}\omega_{\nu} - 2\omega_{(\mu}\Omega_{\nu)} + \frac{1}{3}\delta_{\mu\nu}\left[2\sigma^2 + \omega^2 + 2\omega_{\rho}\Omega^{\rho}\right] + S_{\mu\nu}, \quad (2.64)$$

where $S_{\mu\nu}$ is the trace free part of the Ricci tensor $\mathcal{R}_{\mu\nu}$. Again, from our choices and $\mathcal{R} = 0$ we have that

$$E_{\mu\nu} = S_{\mu\nu} = \mathcal{R}_{\mu\nu}. \quad (2.65)$$

Finally, the Bianchi identities for the Weyl tensor allow us to write [81]

$$0 = (\mathbf{e}_{\nu} - 3a_{\nu})\left(E^{\mu\nu}\right) + 3\omega_{\nu}H^{\mu\nu} - \epsilon^{\mu\nu\sigma}\left[\sigma_{\nu\rho}H^{\rho}_{\sigma} + n_{\nu\rho}E^{\rho}_{\sigma}\right], \quad (2.66)$$

where $\mathbf{e}_{\nu}$ is a frame derivative and ω_{ν} is the vorticity vector, defined as $\omega^{\mu} \equiv \frac{1}{2}\eta^{\mu\nu\rho\sigma}\omega_{\nu\rho}u_{\sigma}$, with $\eta^{\mu\nu\rho\sigma}$ being the totally antisymmetric permutation tensor. The 3D totally antisymmetric permutation tensor is $\epsilon^{\mu\nu\sigma}$ with $\epsilon^{123} = 1$, $\epsilon^{132} = -1$, and we also have a 1-index object a_{ν} which we will relate to the expansion for apparent horizons in the next section, and a symmetric 2-index object, $n_{\nu\rho}$ [82]. We will return to these expressions once we have introduced the concept of an apparent horizon in the next section.

Apparent Horizons

Apparent horizons are defined as outermost marginally outer trapped surfaces where the expansion of outgoing null geodesics vanish. The precise location of apparent horizons can be found numerically [83], or located using approximate or analytic methods. We will briefly review the above definition in what follows, and follow the results in [1].

We can first of all consider a closed 2-dimensional spatial surface S in the hypersurface Σ, and define s^{μ} as an outward pointing unit normal lying in Σ, and we have that $s^{\mu}n_{\mu} = 0$, where n^{μ} is the unit normal to the hypersurface. Just as the 4-dimensional metric $g_{\mu\nu}$ induces a 3-dimensional metric $h_{\mu\nu}$ on the hypersurface, so does the 3-dimensional metric induce a 2-dimensional metric $m_{\mu\nu}$ on the surface S. This is also known as the screen space projector, and is given by

$$m_{\mu\nu} = h_{\mu\nu} - s_{\mu}s_{\nu}. \quad (2.67)$$

We can further define two future pointing null geodesic vectors k^{μ} and l^{μ}, where only k^{μ} will be of importance in our subsequent analyses as we take this to be the

outgoing geodesic. It is defined as

$$k^\mu \equiv \frac{1}{\sqrt{2}}\left(n^\mu + s^\mu\right). \tag{2.68}$$

Its expansion is given by $m^{\mu\nu}\nabla_\mu k_\nu$. A 2-dimensional surface on Σ where the expansion of null geodesics is negative everywhere is known as an outer trapped surface. There can exist multiple regions in Σ with outer trapped surfaces - these can form a connected region. Thus the boundary of this region is defined as a surface where the expansion of the outgoing null geodesics vanishes, and it is this that we call the apparent horizon, or outermost marginally outer trapped surface. For the Schwarzschild geometry, the apparent horizon coincides with the event horizon.

Our criteria for the apparent horizon is therefore given by

$$\begin{aligned} 0 &= m^{\mu\nu}\nabla_\mu k_\nu \\ &= \frac{1}{\sqrt{2}} m^{\mu\nu}\nabla_\mu(n_\nu + s_\nu) \\ &= \frac{1}{\sqrt{2}} m^{\mu\nu}\nabla_\mu(u_\nu + e_{1\,\nu}), \end{aligned} \tag{2.69}$$

where we used the definition of the outgoing null geodesic, Equation (2.68), and the fact that we can align the unit timelike vector u^μ with the unit normal n^μ and the frame vector e_1^μ with the outward unit normal s^μ from the surface S. The first of these terms we can identify as the trace of the extrinsic curvature, which by imposing a time-symmetric hypersurface vanishes. The second term is the expansion of e_1^μ in the screen space, which therefore vanishes also. We can now apply these results to the orthonormal frame equations we looked at in the previous section.

We can define a Ricci principal direction as being a Ricci direction proportional to the normal of a surface, specifically for a $(n-1)$-dimensional surface with indeterminate lines of curvature residing in a constant mean curvature n-dimensional space. We can quantify this as being equivalent to

$$\mathcal{R}^{\mu\nu} e_{1\,\mu} \propto e_1^\nu. \tag{2.70}$$

From this, we can immediately see that the components of the electric part of the Weyl tensor, E_{12} and E_{13}, immediately disappear at all points on the apparent

horizon, as if we perform the contraction,

$$\begin{aligned}\mathcal{R}_{12} &= \mathcal{R}^{\mu\nu} e_{1\,\mu} e_{2\,\nu} \\ &\propto e_1^{\nu} e_{2\,\nu} = 0 = E_{12},\end{aligned} \tag{2.71}$$

where we have used the definition of a Ricci principal direction, the fact that the orthonormal basis vectors are orthogonal, and Equation (2.65). Furthermore, time symmetry implies that the magnetic part of the Weyl tensor $H_{\mu\nu}$ vanishes. Finally, due to the choice of locally rotationally symmetric curves, the only non-zero components of the tensor $n_{\nu\rho}$ is n_{23} [2, 82]. Putting all of this together means Equation (2.66) becomes [82]

$$\mathbf{e}_1\left(E^{11}\right) = 3a_1 E^{11} + n_{23}\left(E_3^3 - E_2^2\right), \tag{2.72}$$

where $\mathbf{e}_1$ is a frame derivative in a direction normal to the apparent horizon and $2a_1 = -\nabla_\nu e_{1\mu} m^{\mu\nu}$ is the expansion of e_1^μ. The subscripts 1, 2 and 3 in this equation correspond to frame components. This is an important result that we will use in chapters 4 and 5 to calculate the positions of the apparent horizons in our cosmological models.

In the Presence of a Cosmological Constant

One can also include the cosmological constant Λ terms in the orthonormal frame constraint equations. This will be of relevance to chapter 5 where we add Λ to the black hole lattices and calculate the positions of their horizons. As in the time-symmetric case, the shear and vorticity tensors vanish, whilst the expansion scalar Θ is non-zero, as it is related to the trace of the extrinsic curvature. Using these results, we can see that Equation (2.63) in the presence of Λ becomes

$$\begin{aligned}0 &= -\frac{1}{3}\Theta^2 + \sigma^2 - \omega^2 - 2\omega_\mu \Omega^\mu - \frac{1}{2}\mathcal{R} + \Lambda \\ &= -\frac{1}{3}\Theta^2 - \frac{1}{2}\mathcal{R} + \Lambda.\end{aligned} \tag{2.73}$$

Using the definitions of the expansion scalar and the extrinsic curvature we see that $\Theta = -K$, and we show in chapter 5 that a suitable choice of cosmological constant is one where $K^2 = 3\Lambda$. Combining these results we simply have that $\mathcal{R} = 0$ as before, and therefore Equations (2.65) and (2.72) are unchanged from the time-symmetric case.

Previously, the definition of an apparent horizon, Equation (2.69), and the choice of time-symmetric hypersurfaces meant that both $K = 0$ and the expansion of e_1^μ

was zero. Now, we can instead derive a relation between both of these quantities, as they are both non-zero. Using Equation (2.69) we can instead write

$$\begin{aligned} -m^{\mu\nu}\nabla_\mu e_{1\,\nu} &= m^{\mu\nu}\nabla_\mu u_\nu \\ &= \frac{2}{3}\Theta, \end{aligned} \tag{2.74}$$

where we have used the fact that the screen space projector $m_{\mu\nu}$ contains only 2 of the 3 orthonormal basis vectors. We will return to these results in chapter 5, where we will apply it to Equation (2.72).

2.3 Exact Solutions

There have been many attempts at constructing solutions of the Einstein field equations, from simple solutions to more complicated configurations of black holes embedded in a background. In this section we review some of the main attempts so far and how they are related. Of course there are far too many to compile an exhaustive list, therefore we refer the reader to both [84] and [85] for complete overviews of the topic. We instead focus on solutions that are of interest from an inhomogeneous cosmological point of view, or that are related to our black hole lattices, such as the Einstein-Maxwell solutions.

2.3.1 Homogeneous Solutions

Minkowski Solution

The simplest solution to the Einstein field equations (2.7) is the Minkowski metric, denoted by $\eta_{\mu\nu}$ and is given by $\eta_{\mu\nu} = \text{diag}(-1, 1, 1, 1)$. Its line element is therefore

$$ds^2 = \eta_{\mu\nu}dx^\mu dx^\nu, \tag{2.75}$$

and is a solution to the vacuum field equations in the absence of Λ. It can also be used to describe weak-field solar system phenomena where Newtonian gravity is insufficient. Small perturbations around the Minkowski metric, where the global spacetime metric can be written as

$$g_{\mu\nu} = \eta_{\mu\nu} + h_{\mu\nu}, \tag{2.76}$$

with $h_{\mu\nu}$ denoting the deviation from Minkowski spacetime, can be used as post-Newtonian corrections and can account for the perihelion shift of Mercury [86].

FLRW Solution

If spatial homogeneity and isotropy is assumed, then such a spacetime is given uniquely by the FLRW metric with line element

$$ds^2 = -dt^2 + a^2(t)\left(\frac{dr^2}{1-kr^2} + r^2 d\Omega^2\right), \tag{2.77}$$

where $a(t)$ is the scale factor, denoting the expansion of the universe, $d\Omega^2 = d\theta^2 + \sin^2\theta d\phi^2$, and there are 3 possibilities for the curvature parameter k depending on the spatial geometry,

$$k = \begin{cases} 1, & \text{for a closed universe,} \\ 0, & \text{flat,} \\ -1, & \text{open.} \end{cases} \tag{2.78}$$

The reader may note that for a flat universe, the FLRW metric is conformally related to the previous Minkowski metric, with the scale factor $a(t)$ being the conformal factor.

The FLRW spacetime is a non-vacuum solution, which means the stress-energy tensor is chosen to be that of a perfect fluid, given by

$$T_{\mu\nu} = (\rho + P)u_\mu u_\nu + P g_{\mu\nu}, \tag{2.79}$$

where ρ is the energy density, P is the pressure, and u^μ is the 4-velocity of the fluid. The pressure and density can be related through an equation of state, $P = \omega\rho$, where the value of the parameter ω indicates the type of fluid considered,

$$\omega = \begin{cases} \frac{1}{3}, & \text{radiation,} \\ 0, & \text{dust,} \\ -1, & \text{dark energy.} \end{cases} \tag{2.80}$$

Dust is collisionless and non-relativistic, hence $P = 0$, and is also known as matter, whilst radiation is considered relativistic. The field equations for the metric in Equation (2.77) and the stress-energy tensor Equation (2.79) result in the Friedmann

equations in the presence of Λ as,

$$\left(\frac{\dot{a}}{a}\right)^2 = \frac{8\pi G}{3}\rho - \frac{k}{a^2} + \frac{\Lambda}{3}, \tag{2.81}$$

$$\frac{\ddot{a}}{a} = -\frac{4\pi G}{3}(\rho + 3p) + \frac{\Lambda}{3}, \tag{2.82}$$

where overdots denote differentiation with respect to proper time t. The solutions for the scale factors $a(t)$ then take different forms depending on the spatial geometry and the fluid under consideration, see [41] for details. For dust filled universes, only the closed case has a maximum of expansion, whilst the open and flat universes expand forever. This is analogous to the construction of initial data for the vacuum constraint equations in section 2.2.3, where time symmetry, or a maximum of expansion, restricted the solutions to have a curved conformal metric, whereas a non-zero extrinsic curvature admitted solutions with a flat conformal space.

2.3.2 Inhomogeneous Perfect Fluid Solutions

One can relax the assumption of homogeneity used in the Minkowski and FLRW spacetimes above to consider inhomogeneous solutions to the Einstein field equations. The motivation for doing so is discussed in more detail in section 2.4, but we will introduce the most commonly used metrics here.

Lemaître-Tolman-Bondi Solution

The Lemaître-Tolman-Bondi (LTB) solution represents a spherically symmetric dust spacetime and relaxes a degree of homogeneity compared to the FLRW metric. It can be written in comoving coordinates as [87]

$$ds^2 = -dt^2 + X^2(t, r)dr^2 + Y^2(t, r)d\Omega^2, \tag{2.83}$$

where $Y(t,\, r)$ is the areal radius. The function $X(t,\, r)$ is dependent on $Y(t,\, r)$ and through solving the Einstein field equations this relation is apparent through writing the metric as

$$ds^2 = -dt^2 + \frac{[Y'(t, r)]^2}{1 + 2E(r)}dr^2 + Y^2(t, r)d\Omega^2, \tag{2.84}$$

where $E(r)$ is now a function of radial coordinate only and $Y' = \partial Y/\partial r$. The function $E(r)$ determines the curvature of the space at each value of r. To see this, if $E = 0$, then the metric of the space $t =$ constant is flat. The evolution equation for $Y(t,\, r)$

is given by

$$\dot{Y}^2 = \frac{2M}{Y} + 2E, \tag{2.85}$$

where $\dot{Y} = \partial Y/\partial t$ and $M = M(r)$ is the gravitational mass within a radius r, whilst the energy density is given by

$$4\pi G\rho = \frac{M'}{Y^2 Y'}. \tag{2.86}$$

Equation (2.85) has three solutions based on the sign of E. These expressions involve a further function, $t_b(r)$, which is the local big bang time. Altogether the three functions of r completely characterise the solution. The FLRW metric can be obtained by choosing

$$Y(t,\, r) = a(t)r. \tag{2.87}$$

One of the aims of the LTB solution is to model the structures we observe in the Universe. However, it is spherically, not axially, symmetric and therefore cannot model rotation, meaning it is inadequate to describe single galaxies and even galaxy clusters [88]. The solution describes voids well, as these have been shown to have spherical symmetry as a stable property. Mustapha, Hellaby and Ellis [89] proved that the LTB solution can be fitted to any set of observed number densities and areal distances, together with the evolution functions for luminosity and mass per source, making it a viable choice for cosmology. Indeed, it has been shown that the LTB spacetime can explain the apparent accelerated expansion without the need for dark energy. However, a shortcoming of the LTB spacetime is that it requires a central observer, sometimes at the centre of a large void, which violates the Copernican principle [90].

Szekeres Solution

The Szekeres family of solutions are the most general known inhomogeneous, dust filled, exact solutions, exhibiting no symmetries and thus generalising solutions like LTB [91]. As a result, they can model more general shapes of voids and clusters, and overcome the restrictions imposed by spherical symmetry discussed above. The metric for the Szekeres solution is given by [88]

$$ds^2 = -dt^2 + e^{2\alpha}dr^2 + e^{2\beta}\left(dx^2 + dy^2\right), \tag{2.88}$$

where $\alpha = \alpha(t, x, y, r)$ and $\beta = \beta(t, x, y, r)$ are determined by solving the Einstein field equations. Defining $\beta' = \partial\beta/\partial r$ allows the Szekeres family to be divided into

two subclasses, those with $\beta' = 0$ and those with $\beta' \neq 0$. The latter of these contains the LTB solution as a subset, and has the metric functions written as

$$\begin{aligned} \mathrm{e}^{\beta} &= \Phi(t,r)\mathrm{e}^{\nu(r,x,y)}, \\ \mathrm{e}^{\alpha} &= h(r)\Phi(t,r)\beta' \equiv h(r)\left(\Phi' + \Phi\nu'\right), \\ \mathrm{e}^{-\nu} &= A(r)\left(x^2+y^2\right) + 2B_1(r)x + 2B_2(r)y + C(r), \end{aligned} \tag{2.89}$$

where $\Phi(t,r)$ is defined as being a solution to the following,

$$\dot{\Phi}^2 = -k(r) + \frac{2M(r)}{\Phi} + \frac{1}{3}\Lambda\Phi^2. \tag{2.90}$$

The functions $h(r), k(r), M(r), A(r), B_1(r), B_2(r)$ and $C(r)$ are arbitrary and obey

$$g(r) \equiv 4\left(AC - B_1^2 - B_2^2\right) = 1/h^2(r) + k(r), \tag{2.91}$$

where g is another arbitrary function of r. The sign of $g(r)$ in Equation (2.91) then further divides this class of Szekeres solutions. The most commonly studied are those with $g > 0$, called the quasi-spherical solutions, which have non-concentric spheres of constant mass. The quasi-plane solutions have $g = 0$, whilst the quasi-hyperbolic have $g < 0$. The FLRW metric is recovered when $B_1 = B_2 = 0$, $C = 4A = 1$ and $\Phi(t,r) = rR(t), k = k_0 r^2$ where k is a constant. In terms of applications, the Szekeres models have been used to study non-spherical collapse, light propagation and structure formation, see references within [92] and [93].

The LTB and Szkeres spacetimes aim to describe our Universe more realistically than the FLRW metric, and in particular provide conclusions about the effects of inhomogeneities on light propagation and whether this can account for the late time accelerated expansion. An alternative to these are the lattice toy models, which are also exact solutions but do not aim to describe the Universe as a whole. These black hole lattices, which we introduce more rigorously in chapter 3, are therefore simple testbeds for analysing the effects of inhomogeneities without trying to model the complexity of structures. Both approaches to modelling inhomogeneity are valuable contributions and can offer complementary results.

2.3.3 Swiss-Cheese Type Solutions

Swiss-Cheese solutions all involve a background FLRW spacetime with spherical regions removed and filled with spacetimes such as Schwarzschild, Schwarzschild-de Sitter, LTB, or Szekeres [87]. These regions can contain hierarchies of masses or

self-similar structures. The solutions enjoy many applications, from modelling voids in the large-scale structure of the Universe [94] to patchwork universes of different curvature [95]. Recently the optical properties have been studied in a cosmological context [96]. For further applications to cosmology see [87].

The aim of the Swiss-Cheese solutions is to model inhomogeneity as regions of inhomogeneity within a more general homogeneous background, rather than one large inhomogeneity as in the LTB or Szekeres metrics. This arguably is a more realistic way to think about structure in the Universe and sets the scene for our discussion of black hole lattices in chapter 3, which further require no embedding background.

McVittie Solution

The McVittie solution in 1933 was one of the first to consider compact objects in an expanding background [97]. This is achieved by constructing a solution describing a black hole embedded in an FLRW cosmology. The solution can be written as [93]

$$\mathrm{d}s^2 = -\left(\frac{1-\mu(t,r)}{1+\mu(t,r)}\right)^2 \mathrm{d}t^2 + R^2(t)\frac{(1+\mu(t,r))^4}{\left(1+\frac{1}{4}kr^2\right)^2}\left(\mathrm{d}r^2 + r^2 d\Omega^2\right), \tag{2.92}$$

where $R = R(t)$ is an arbitrary function, the function $\mu(t,r)$ is defined as

$$\mu(t,r) = \frac{m}{2rR}\sqrt{1+\frac{1}{4}kr^2}, \tag{2.93}$$

and m and k are constants. The former can be interpreted as the mass in an FLRW universe, whilst k is the spatial curvature. This solution reduces to the Schwarzschild line element in isotropic coordinates, Equation (2.11), for $k = 0$, $R = 1$, and the flat FLRW solution for $m = 0$. McVittie intended to analyse the effect of cosmological expansion on planetary orbits, and it was found that the effect was zero. However, many authors have since pointed out that a physical interpretation is limited due to the coordinate dependence and therefore non-covariant approach [98, 99]. Moreover, for $k = 0$, instead of being a horizon as in the Schwarzschild metric, the surface $r(1+\mu)^2 = 2m$ is singular [44].

In terms of cosmology, the spatial volume of a McVittie universe with n singularities compared to the total volume of an Einstein static universe V_{Einstein}, is given by [100]

$$V = \frac{16M^3}{\pi}\left(1+\frac{2nm}{M}\right) > \frac{16M^3}{\pi} = V_{\text{Einstein}}, \tag{2.94}$$

where M is the total mass. This can be interpreted as the scale of such a discrete cosmological solution being altered by the presence of the singularities, or masses.

Einstein-Straus Solution

A solution to the above problems in the McVittie solution was provided by Einstein and Straus, [101, 102], whereby a spherical region of Schwarzschild was matched to a Friedmann background. This was done by ensuring the mass in the Schwarzschild region was equal to the mass removed from the FLRW region. This mass M is then related to the radius R_h of the removed region, via the following [103]

$$M = \frac{4\pi}{3}\rho\left(RR_{\mathrm{h}}\right)^3, \tag{2.95}$$

where ρ is the average density and R the scale factor from before. Matching the induced metric and extrinsic curvature, and imposing Equation (2.95) at the boundary ensures the spacetimes are smoothly matched, and is based on the Darmois-Israel junction conditions. Again, no effect was found from the global expansion on planetary orbits in the Schwarzschild regions. However, this is true by design and occurs due to the matching of the two spacetimes and requiring that the boundary evolves in a Friedmannian way [87, 100]. Furthermore, the solution is unstable to perturbations of this expression for mass, and so still has limitations [98].

The black hole lattices overcome the problems encountered in these Swiss-Cheese cosmologies in that they do not rely on an FLRW background, and are constructed purely out of inhomogeneities, in order to best analyse their effects on the cosmology.

2.3.4 Einstein-Maxwell Solutions

Majumdar-Papapetrou Solution

If one includes electromagnetism, further solutions can be found to the source-free vacuum Einstein-Maxwell equations. This is known as the Majumdar-Papapetrou solution, [104, 105], and has a line element given by

$$ds^2 = -U^{-2}dt^2 + U^2\left(dx^2 + dy^2 + dz^2\right), \tag{2.96}$$

where m_i are the masses of the black holes, the coordinate r is related to the coordinates x, y, z by $r_i = \sqrt{(x-x_i)^2 + (y-y_i)^2 + (z-z_i)^2}$, and the function U is

given by

$$U = 1 + \sum_i m_i / r_i. \tag{2.97}$$

The relation between the scalar potential A_t and the metric is given by $A_t = U^{-1}$. Given the line element in Equation (2.96), the source-free Einstein-Maxwell equations reduce to the Laplace equation for the function U [106],

$$\nabla^2 U = \frac{\partial^2 U}{\partial x^2} + \frac{\partial^2 U}{\partial y^2} + \frac{\partial^2 U}{\partial z^2} = 0, \tag{2.98}$$

thus demonstrating the superposition of point masses in the form of the expression for U, Equation (2.97).

The black holes in this solution are extremal, that is, they have charge q equal to their mass m. Physically this corresponds to the black holes being in static equilibrium, with the gravitational attraction balanced by the electrostatic repulsion. The Majumdar-Papapetrou solution was extended and interpreted by Hartle and Hawking as a system of charged black holes [106]. Finally, for the case of one point mass, the solution can be seen to reduce to the Reissner-Nordström spacetime with equal charge and mass under the coordinate transformation $r \to r - m$. In chapter 6 we extend this existing work to a cosmological setting and construct lattices of charged black holes that have non-extremal charge.

Kastor-Traschen Solution

The Kastor-Traschen solution generalises the Majumdar-Papapetrou solution to include a positive cosmological constant, Λ, whilst still having equal charge and mass [107]. The black holes are no longer in static equilibrium, but instead are dynamic, and can either move out of causal contact with one another or merge completely. The Kastor-Traschen solution, and hence the Majumdar-Papapetrou solution, has also seen cosmological applications. These include that of Bonnor, with a background FLRW cosmology with arbitrary spatial curvature [108], as well as the construction of a Kastor-Traschen-FLRW hybrid solution in [109]. Again, we emphasise the reliance on a Friedmann background in these solutions for cosmological applications.

Israel-Khan Solution

The Majumdar-Papapetrou solution introduced above extends the well known Weyl class of solutions [7], which describes a static, axisymmetric vacuum spacetime in Einstein-Maxwell theory, to spacetimes exhibiting no spatial symmetry.

Another solution of interest also belongs to this Weyl class, and is known as the Israel-Khan solution [110]. This describes two or more finitely many collinear Schwarzschild black holes in equilibrium. The sources for U in Equation (2.97) are taken to be thin rods, all lying in the axis of symmetry, which are connected by struts. The distance between neighbouring black holes stays constant due to the struts exerting an outward pressure which cancels the gravitational attraction between the black holes [111]. However, there exist conical singularities in the struts between the black holes, making this solution unfeasible for cosmological purposes if we wish to investigate the effect of discrete sources on the surrounding expansion.

A way around the problem of conical singularities is to consider infinitely many black holes equally spaced. In [112] this was interpreted as a higher dimensional solution to Kaluza-Klein theory (a 5-dimensional unification of gravity and electromagnetism) with one spatial dimension compactified to a circle, representing a black hole localised on the circle [113]. Korotkin and Nicolai independently construct a vacuum black hole solution which is periodic in one direction and asymptotes to the Kasner vacuum anisotropic spacetime [114]. This can also be interpreted as an infinite line of black holes without conical singularities, however the authors note that the trade-off is instability under non-periodic perturbations.

2.4 Inhomogeneous Cosmology

2.4.1 The Standard Cosmological Model

The main foundational assumption underpinning the ΛCDM standard model of cosmology is the cosmological principle. This states that the Universe is spatially homogeneous and isotropic, allowing the FLRW metric (2.77) to be used as the solution to the Einstein field equations. This is supported by two ingredients - assuming the Copernican principle, and temperature anisotropy measurements of the CMB. The former of these states that we do not live in a special place in the Universe. Any observations made by us are the same as any other measurements made elsewhere. The latter reveals that temperature variations of the CMB are of the order of $< 10^{-5}$ [115]. Thus, we can assume the CMB is close to isotropic about all points, and mathematically this implies homogeneity, and allows the cosmological principle to be adopted.

However, the Universe we observe is only homogeneous and isotropic in a statistical sense. One can derive a homogeneity scale for the Universe, where above this, structures are statistically homogeneous. Currently this is found to be at $70h^{-1}$ Mpc,

or 100Mpc, where h is the dimensionless Hubble parameter [18]. Below this, and on small scales, it is manifest that our Universe is highly inhomogeneous and anisotropic, and the use of the FLRW metric is a coarse-grained description of reality.

2.4.2 The Backreaction Problem

The problem with assuming a perfectly homogeneous and isotropic background spacetime for all scales, and as a result homogeneous and isotropic expansion, lies in the Einstein field equations. The FLRW assumption leads to the equations as being

$$G[\langle g\rangle] = T^{\text{eff}}, \tag{2.99}$$

where G denotes the Einstein tensor, g the spacetime metric and T^{eff} an effective stress energy tensor. The angular brackets denote that the FLRW solution is in some sense an averaged spacetime, as it does not include any small-scale inhomogeneities. Averaging and evolution do not commute which means we can also write

$$\langle G[g]\rangle = \langle T\rangle, \tag{2.100}$$

which, in general, may be different to Equation (2.99). The reason for this becomes clear if we first realise that the Christoffel connection, Equation (2.2), can be written as $\Gamma \sim \partial g$ [116]. This implies the Riemann tensor and its contractions can be written as $R \sim \partial\Gamma + \Gamma^2$. As a result, Equation (2.99) will give us

$$G[\langle g\rangle] = \partial\langle\Gamma\rangle + \langle\Gamma\rangle^2, \tag{2.101}$$

whilst Equation (2.100) gives

$$\langle G[g]\rangle = \partial\langle\Gamma\rangle + \langle\Gamma^2\rangle. \tag{2.102}$$

The difference between these two can then be quantified as backreaction, by defining $B \equiv T^{\text{eff}} - \langle T\rangle = \langle\Gamma\rangle^2 - \langle\Gamma^2\rangle$, and physically corresponds to the small-scale inhomogeneities that were otherwise ignored in adopting the FLRW spacetime, contributing to and affecting the large-scale dynamics of the Universe over time. Furthermore, general relativity is valid locally, yet concordance cosmology assumes averaged quantities such as density follow the same equations. As yet there is little consensus on concrete conclusions that can be drawn about backreaction and the magnitude of its effects. What can be agreed on however, is the common goal of implementing

general relativity correctly on all scales. This leads to the discussion of the averaging, coarse-graining, and fitting problems [117, 118].

The averaging problem asks how best to average the tensors in the above equations such that the effects of small-scale structures on the dynamics of the Universe have been included? Pioneering progress in devising a suitable averaging scheme was made by Buchert [119, 120]. This involves foliating the spacetime by hypersurfaces and defining the spatial average of a scalar function Ψ,

$$\left\langle \Psi\left(t, X^i\right)\right\rangle_{\mathcal{D}} := \frac{1}{V_{\mathcal{D}}}\int_{\mathcal{D}} dV \Psi\left(t, X^i\right), \tag{2.103}$$

over a domain $\mathcal{D}(t)$. Using this and defining a dimensionless effective scale factor $a_{\mathcal{D}}$, the scalar part of the Raychaudhuri equation (an equation for the expansion scalar θ and its kinematics) and Hamiltonian constraint result in two Friedmann like equations,

$$3\frac{\ddot{a}_{\mathcal{D}}}{a_{\mathcal{D}}} + 4\pi G\langle\rho\rangle_{\mathcal{D}} = \mathcal{Q}_{\mathcal{D}} \tag{2.104}$$

$$3\left(\frac{\dot{a}_{\mathcal{D}}}{a_{\mathcal{D}}}\right)^2 - 8\pi G\langle\rho\rangle_{\mathcal{D}} + \frac{1}{2}\langle\mathcal{R}\rangle_{\mathcal{D}} = -\frac{\mathcal{Q}_{\mathcal{D}}}{2}, \tag{2.105}$$

where $\mathcal{R}$ is the spatial Ricci scalar. The backreaction term, $\mathcal{Q}_{\mathcal{D}}$, is defined as

$$\mathcal{Q}_{\mathcal{D}} \equiv \frac{2}{3}\left\langle\left(\theta - \langle\theta\rangle_{\mathcal{D}}\right)^2\right\rangle_{\mathcal{D}} - 2\left\langle\sigma^2\right\rangle_{\mathcal{D}}, \tag{2.106}$$

where $\langle\theta\rangle_{\mathcal{D}}$ is the averaged expansion rate, defined as $\langle\theta\rangle_{\mathcal{D}} = \frac{\dot{V}_{\mathcal{D}}}{V_{\mathcal{D}}} = 3\frac{\dot{a}_{\mathcal{D}}}{a_{\mathcal{D}}}$, θ is the expansion scalar and σ^2 is defined using the shear tensor, $\sigma^2 \equiv \frac{1}{2}\sigma^{ij}\sigma_{ij}$.

The average expansion rate can differ from the local one. However, the scheme depends on the choice of foliation, and there are no clear interpretations for what this means in terms of observables [118]. Recent work has seen a clarification of the dependence on spacetime foliation [121].

Coarse-graining, although similar to the averaging problem, differs in that it is more 'bottom-up' and asks what this smoothing process looks like at each scale of the Universe. Our Universe has a complex hierarchy of structure, and schematically a coarse-graining approach to this may look like the following [117],

$$\left.\begin{array}{l} g_{\mu\nu}^{\text{stellar}} \rightarrow g_{\mu\nu}^{\text{galaxy}} \rightarrow g_{\mu\nu}^{\text{cluster}} \rightarrow g_{\mu\nu}^{\text{wall}} \\ \qquad\qquad\qquad\qquad\qquad\quad \vdots \\ \qquad\qquad\qquad\qquad\qquad\quad g_{\mu\nu}^{\text{void}} \end{array}\right\} \rightarrow g_{\mu\nu}^{\text{Universe}}, \tag{2.107}$$

where the ellipsis indicates that more than one metric might be used to describe structures such as walls or voids. Due to the complexity of this problem, most studies are limited to analysing one level of hierarchy. The black hole lattices we will introduce in chapter 3 typically have a much more simple $g_{\mu\nu}^{\text{stellar}} \rightarrow g_{\mu\nu}^{\text{universe}}$ [117].

Finally, the fitting problem asks which spacetime best represents the real Universe. As this is a complex problem, progress is made by instead assuming FLRW from the outset, and asking, what errors have been introduced in doing so. This quantifies the definition of backreaction above.

2.4.3 Current Approaches

Whilst inhomogeneous cosmologies have been around for a number of decades, see section 2.3 and [84], the debate about backreaction within inhomogeneous cosmological models has only been around for the last 10 years or so. Despite the claims otherwise, [27, 29, 30], it is generally accepted that backreaction is a relevant effect in cosmology [28]. The question now being addressed is, how relevant? There exist many different approaches, which we will review in this section, resulting in varying degrees of relevance, from one-percent effects to much larger order-unity effects. A unified consensus should be reached in terms of how backreaction should be measured, and consequently, the magnitude of its effect [122]. A survey of around 50 academics working in the field of inhomogeneous cosmologies revealed that 40% surveyed feel that backreaction was the most important topic to study, in particular how it is defined and how nonlinearities and inhomogeneities affect the expansion. A similar proportion of people feel this is where the field should focus within the next 5-10 years [123].

In this section we review some of the more recent approaches to addressing backreaction. These approaches loosely fall under the categories of exact models, numerical cosmology, perturbative approaches, as well as N-body simulations. Note however, that there exist perturbative numerical studies, for example.

Exact Models

The exact model approaches broadly fall into two camps - those based on exact solutions, such as LTB or Szekeres [123–128] (see section 2.3 and references within [93] and [88]), and the family of black hole lattices. The latter of these form the basis of this thesis, and are discussed in more detail in section 3, for a review see [129]. They are also exact solutions to the Einstein field equations, but from an initial data construction, and involve superpositions of Schwarzschild masses in

various configurations. Embedding the LTB or Szekeres spacetimes via Swiss-Cheese methods, as introduced in the previous section, still requires a background spacetime, usually FLRW, so is not a fully independent approach to addressing backreaction. For purely LTB or Szekeres models, structure formation can evolve differently to a corresponding FLRW solution, but generally backreaction remains small in models that are suitable cosmologies.

In [130], a slightly different analysis was performed based on the Swiss-Cheese model. An exact dust solution was considered consisting of spherical masses of constant density placed inside a Schwarzschild spacetime, and this procedure was repeated inside the mass to give a self-similar solution of nested voids and overdensities. A large difference was found between the ADM mass and the sum of masses inside, suggesting the nonlinear effects of general relativity are amplified over sufficiently many scales and give rise to a backreaction effect in the form of a mass deficit.

Numerical Cosmology

Numerical cosmology aims to use the techniques developed in numerical relativity to solve the Einstein field equations for inhomogeneous cosmological models. This has an advantage over the previous toy models in that more realistic scenarios can be considered, as well as allowing for the full time evolution to be calculated. Notable works include that of Bentivegna and Bruni [131], who considered an inhomogeneous distribution of dust in a perturbed Einstein-de Sitter model. They investigated the departure of the evolution from a reference FLRW model by looking at several quantities, including the average expansion rate, which deviated locally by as much as 28% at an underdensity. Complementary studies by Macpherson et al [132–134], have also shown interesting results. They find no global backreaction, but deviations from FLRW predictions in cosmological parameters of: $6-31\%$ on small scales, $2-5\%$ on scales above the homogeneity scale. The inhomogeneities are also unable to resolve the Hubble tension. Other works include a silent universe simulation [123], as well as approaches based on the BSSN formalism of numerical relativity by Giblin, Mertens and Starkman [135, 136]. Numerical studies of the black hole lattices by Bentivegna, Korzyński and Yoo are described in more detail in chapter 3.

A recent aim of the numerical studies is to investigate whether the approximations employed in relativistic N-body simulations are valid. Traditional N-body simulations model astrophysical or cosmological systems as dynamical systems of particles under gravity. They are used to study galaxy formation and dark matter haloes, as well as reproduce filaments and void-like structures that are observed in large-scale surveys.

Recent advancements have involved extending these to include relativistic effects [137–139]. The simulations are based on the weak field approximation only, so cannot be used to model black holes or large sources of gravitational fields. Non-Newtonian effects such as frame-dragging are found to be small. The authors state that their simulations are fully relativistic, however, Macpherson et al point out their studies are based on the weak field approximation, and a quantitative comparison is needed to assess whether this is sufficient or if full numerical relativity is needed [134]. A comparison of fully relativistic and Newtonian simulations did reveal agreement between the two, except in regions where the weak field approximation was no longer valid, as expected [140].

Perturbative Methods

Approximate or perturbative approaches to inhomogeneous cosmology usually involve constructing lattices of discrete masses in various ways, and calculating how these differ to a corresponding FLRW universe. One such perturbative approach was carried out by Bruneton and Larena [141] with an inhomogeneous cosmology modelled by an infinite cubic lattice. The authors used a Fourier series to describe a periodic distribution of masses, and expanded the metric perturbatively in powers of $\sqrt{M/L}$, where L was the size of the lattice and M denoted the mass at the centre of each cell. The solution was exact at second-order, and they found that at order $(M/L)^{3/2}$ the expansion is that of a dust filled FLRW universe. However, this result is only valid up to a certain order, and that higher order terms may introduce a small amount of backreaction through mode couplings.

An alternative approach was begun in [100] and followed up by Sanghai in [142]. An infinite cubic lattice was constructed by gluing together regular cells of perturbed Minkowski spacetime, with the gravitational field inside described by post-Newtonian gravity in terms of a smallness parameter. The cells are matched together by reflection-symmetric boundaries. These lattices therefore are constructed from a 'bottom-up' approach, relying on no FLRW background or averaging techniques. The authors find a Friedmann-like equation modelling the large-scale expansion, with a small radiation term appearing as a relativistic correction. Physically this has a negative energy density, resulting in a decrease in the expansion rate. Further extensions include the addition of radiation and a cosmological constant [143] as well as alternative gravitational theories [144].

2.4.4 Optical Properties

As well as the expansion and dynamics of the above inhomogeneous cosmological models, the propagation of light must also be studied, as in general these two areas can differ in the extent to which they agree with FLRW cosmologies. This is important because next-generation surveys will have the precision to reveal deviations from FLRW predictions, and if inhomogeneities do indeed affect observables then these effects need to be taken into account in light of new data.

Recent works have seen ray-tracing in the perturbed Minkowski models by Sanghai [34], optical properties of the perturbed lattices by Bruneton [145], as well as stochastic treatments of light in Swiss-Cheese models, [96, 146, 147].

Optical properties of the black hole lattices that were pioneered by Lindquist and Wheeler were studied in [148] with the inclusion of arbitrary curvature and a cosmological constant. They calculated the angular diameter distance, luminosity distance, and redshifts for observers within the lattice universe, and found despite the large-scale dynamics agreeing with FLRW, the optical properties did not. However, the discrepancy was not enough to account for the effects of dark energy. More recently, numerical relativity was used to study light propagation in the black hole lattices along two curves - along a cell edge and diagonally between two vertices [149]. The results were compared to both FLRW predictions and the Empty Beam approximation, which showed the best agreement. Furthermore, for different arrangements of masses and separations, as much as 5% deviation from FLRW predictions is found by redshift 0.06. The authors note that their results are a magnitude larger than that of Sanghai, due to an intrinsically different setup, and so further comparison is needed to draw more conclusive statements.

3 Introduction to Black Hole Lattices

In this chapter we review and describe in detail the existing work on the black hole lattices and how they are used to model inhomogeneous cosmologies, first introduced more than 60 years ago, and currently being revived by a number of authors. The reader should note that some authors define inhomogeneous cosmologies as having an FLRW limit [84, 93] however, this is restrictive as it excludes the family of black hole lattices and indeed perturbative lattices that were introduced in the previous section. The lattices studied here form a valuable contribution as they require no approximations or matching across boundaries, and include all relativistic effects at all orders. Parts of section 3.2.1 are taken from [35].

3.1 Lindquist-Wheeler Models

The first attempt at an inhomogeneous model of black holes was that of Lindquist and Wheeler in 1957 [150], and was based on the Wigner Seitz construction of solid state physics. In this, they modelled a closed universe by tessellating a 3-sphere with regular polyhedra and placed a mass at the centre of each. There are only six ways of doing this, either with $N = 5$, 8, 16, 24, 120 or 600 masses, which then determines the type of polyhedra used [151]. The zone around each mass was approximated to be spherical and therefore described by the Schwarschild geometry with a Schwarzschild gravitational potential. At the boundaries, the Schwarzschild solutions were glued together with matching conditions, introducing a 'no man's land', and therefore globally the lattices were not a solution to the Einstein field equations. Nevertheless the expansion of the radius of the lattice was found to be similar to a corresponding Friedmann-like universe.

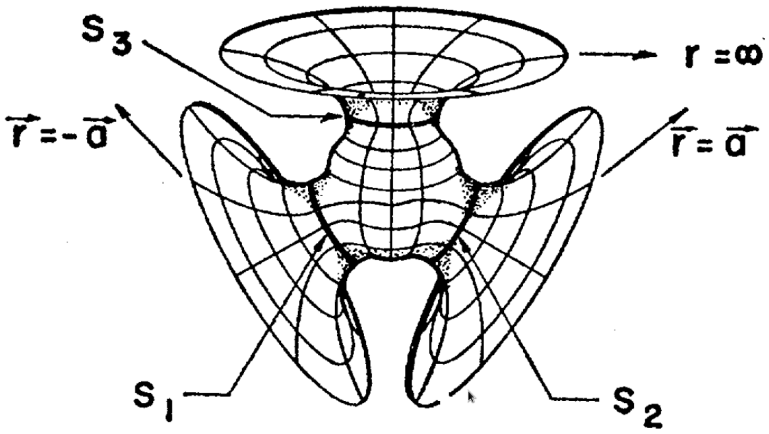

Figure 3.1: An embedding diagram of a 'closed universe' containing 3 black holes represented by the minimal surfaces S_1, S_2 and S_3, along with 3 asymptotically flat regions. This figure is taken from Interaction Energy in Geometrostatics by Brill and Lindquist http://dx.doi.org/10.1103/PhysRev.131.471, and is reproduced with permission by D. Brill.

3.2 Exact Methods

Considerable progress can and has been made in constructing viable black hole lattices by treating it as an initial value problem, and therefore solving the Einstein constraint equations. This circumvents the issues arising with junction conditions as described above, by definition. Misner first looked at instances of momentarily static, or time-symmetric solutions, and dubbed this geometrostatics [152], analogous to work in electrostatics. Brill and Lindquist also constructed time-symmetric initial data for N punctures. This can be thought of as a cosmological region with N black holes corresponding to N asymptotic regions, see Figure 3.1. Additionally, the 5-mass case was looked at in detail by Wheeler in [153].

3.2.1 Time-Symmetric Hypersurfaces

The construction of initial data in order to solve the constraint equations is a relatively simple concept which is used extensively in these lattices. We have already introduced how this works, see section 2.2.2, and we remind the reader that for the vacuum, time-symmetric case we seek solutions ψ to the Helmholtz equation (2.51). We do this by reviewing the lattices in [3] by first linking Equation (2.51) and the conformal factor ψ to a physically suitable choice of solution, that of the Schwarzschild spacetime in isotropic coordinates, see Equation (2.11). In order to

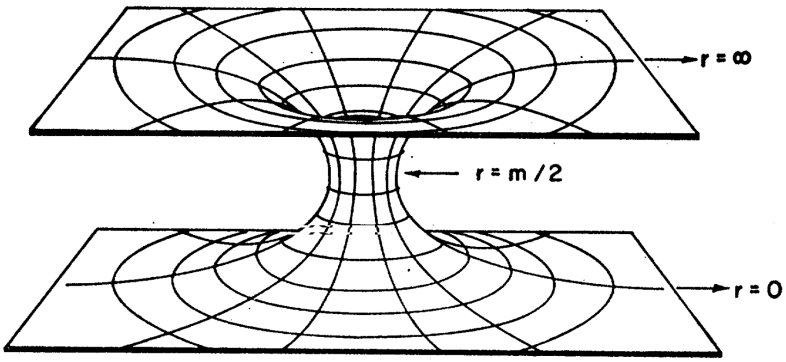

Figure 3.2: An embedding diagram of the Schwarzschild solution, with the singularity $r \to 0$ being mapped to asymptotic infinity. The r coordinate here represents the ρ coordinate from Equation (3.1). This figure is taken from Interaction Energy in Geometrostatics by Brill and Lindquist http://dx.doi.org/10.1103/PhysRev.131.471, and is reproduced with permission by D. Brill.

carry out the 3+1 decomposition on this spacetime we consider a static, spacelike slice of this,

$$ds^2 = \left(1 + \frac{m}{2\rho}\right)^4 (d\rho^2 + \rho^2 d\theta^2 + \rho^2 \sin^2\theta d\phi^2), \tag{3.1}$$

where we can see a factor that resembles a conformal factor of the hypersurface. This hypersurface has a singularity at $\rho = 0$. The following coordinate transformation, which is just an inversion, $\rho = m^2/(4r')$, produces the following metric,

$$ds^2 = \left(1 + \frac{m}{2r'}\right)^4 (dr'^2 + r'^2 d\theta^2 + r'^2 \sin^2\theta d\phi^2), \tag{3.2}$$

that is, the inversion is an isometry of the metric. More importantly, the point $\rho \to 0$ maps to $r' \to \infty$ and so the previous singularity is now the infinity of an asymptotically flat region. This is illustrated in Figure 3.2.

Proceeding as in [3], another coordinate transformation into hyperspherical polar coordinates, $\rho = \frac{m}{2}\tan(\chi/2)$, gives Equation (3.1) as

$$ds^2 = \left(\frac{\sqrt{m}}{2\sin(\chi/2)} + \frac{\sqrt{m}}{2\cos(\chi/2)}\right)^4 (d\chi^2 + \sin^2\chi d\Omega^2), \tag{3.3}$$

where the solid angle element is given by $d\Omega^2 = d\theta^2 + \sin^2\theta d\phi^2$. The first of the two terms in the conformal factor of this geometry diverges at $\chi = 0$, and the second diverges at $\chi = \pi$. These two terms clearly satisfy the Helmholtz equation, Equation (2.51) both individually and as a sum. They are also related to each through the

transformation $\chi \to \pi - \chi$, which corresponds to a rotation of the 3-sphere by an angle π.

We can generate any number of additional terms in the conformal factor ψ by rotating the 3-sphere by any arbitrary angle, and by adding a new term of the form $1/\sin(\chi/2)$ in the new coordinates that result. Moreover, we can exploit the linearity of the Helmholtz equation by summing any n such terms together, in order to obtain a new solution. This generates the conformal factor ψ as follows

$$\psi(\chi,\, \theta,\, \phi) = \sum_{i=1}^{n} \frac{\sqrt{\tilde{m}_i}}{2f_i(\chi,\, \theta,\, \phi)}, \tag{3.4}$$

where i labels a mass, n is the total number of masses, the $\tilde{m}_i$ are the mass parameters which are arbitrary constants, and the f_i are source functions,

$$f_i = \sin\left(\frac{1}{2}\arccos(h_i)\right). \tag{3.5}$$

The terms h_i are given by

$$h_i = w_i \cos\chi + x_i \sin\chi\cos\theta + y_i \sin\chi\sin\theta\cos\phi + z_i \sin\chi\sin\theta\sin\phi, \tag{3.6}$$

for a term that diverges at the position (w_i, x_i, y_i, z_i). Each such position corresponds to the location of a point-like mass in the initial data, and should be accounted for by including a corresponding term in ψ. Any number of masses can be included in the model in this way.

The proof of this is as follows and is taken from [35]: consider rotating the lattice such that one of the masses appears at position $(1, 0, 0, 0)$. Then, the source function for this mass is $h_1 = \cos\chi$ so that $f_1 = \sin(\chi/2)$. Recall now the transformation between Cartesian coordinates and hyperspherical coordinates given in Equation (2.52) which we will restate here,

$$\begin{aligned} w &= \cos\chi, \\ x &= \sin\chi\cos\theta, \\ y &= \sin\chi\sin\theta\cos\phi, \\ z &= \sin\chi\sin\theta\sin\phi. \end{aligned} \tag{3.7}$$

This must then also mean that $w = h_1$. Any subsequent i^{th} mass can be rotated to be at position $(1, 0, 0, 0)$, and in the coordinates after the rotation must have $w' = h_i$.

The general matrix transformation for this rotation is,

$$\begin{pmatrix} w_i' \\ x_i' \\ y_i' \\ z_i' \end{pmatrix} = \begin{pmatrix} \alpha_i & \beta_i & \gamma_i & \delta_i \\ - & - & - & - \\ - & - & - & - \\ - & - & - & - \end{pmatrix} \begin{pmatrix} w_i \\ x_i \\ y_i \\ z_i \end{pmatrix} \tag{3.8}$$

where for ease of presentation we have neglected to include any terms beyond the top line of the matrix. Multiplying out we have

$$w_i' = \alpha_i w_i + \beta_i x_i + \gamma_i y_i + \delta_i z_i \tag{3.9}$$

which can be compared to the requirement $w_i^2 + x_i^2 + y_i^2 + z_i^2 = 1$ for the position of the i^{th} mass on the unit 3-sphere. For both of these equations to be true when $\{w,\, x,\, y,\, z\} = \{w_i,\, x_i,\, y_i,\, z_i\}$, (which means when $w' = 1$), requires $\{\alpha_i,\, \beta_i,\, \gamma_i,\, \delta_i\} = \{w_i,\, x_i,\, y_i,\, z_i\}$. Using this result together with Equations (2.52) and (3.9) then gives

$$w_i' = w_i \cos\chi + x_i \sin\chi \cos\theta + y_i \sin\chi \sin\theta \cos\phi + z_i \sin\chi \sin\theta \sin\phi, \tag{3.10}$$

which upon recalling $w' = h_i$ can be seen to give Equation (3.6) directly. This completes the proof.

We now seek to determine where we will place the n masses on the surface of the 3-sphere. Analogously to [150] we will tessellate the 3-sphere with identical regular, polyhedra, and place a Schwarzschild mass at the centre of each. The positions of these masses will then give us the source functions, and hence the conformal factor as we have seen. This means there are 6 inhomogeneous cosmological models to choose from, those with $n = 5,\, 8,\, 16,\, 24,\, 120$ or 600 masses.

5-Mass Model

The 5-mass model consists of 5 tetrahedra and is known as a 4-simplex. An example set of positions of the 5 masses in such a model, in Cartesian $(w,\, x,\, y,\, z)$ coordinates,

are given below in Equation (3.11) and are taken from [3],

$$\begin{aligned} &i) \quad (1,0,0,0), \\ &ii) \quad \left(-\frac{1}{4}, \frac{\sqrt{15}}{4}, 0, 0\right), \\ &iii) \quad \left(-\frac{1}{4}, -\sqrt{\frac{5}{48}}, \sqrt{\frac{5}{6}}, 0\right), \\ &iv) \quad \left(-\frac{1}{4}, -\sqrt{\frac{5}{48}}, -\sqrt{\frac{5}{24}}, \sqrt{\frac{5}{8}}\right), \\ &v) \quad \left(-\frac{1}{4}, -\sqrt{\frac{5}{48}}, -\sqrt{\frac{5}{24}}, -\sqrt{\frac{5}{8}}\right). \end{aligned} \tag{3.11}$$

We can immediately see that by using Equation (3.6), the functions h_i for this model are given by

$$\begin{aligned} h_1 &= \cos\chi, \\ h_2 &= \frac{\sqrt{15}}{4}\sin\chi\cos\theta - \frac{\cos\chi}{4}, \\ h_3 &= \sqrt{\frac{5}{6}}\sin\chi\sin\theta\cos\phi - \sqrt{\frac{5}{48}}\sin\chi\cos\theta - \frac{\cos\chi}{4}, \\ h_4 &= \sqrt{\frac{5}{6}}\sin\chi\sin\theta\sin\left(\phi - \frac{\pi}{6}\right) - \sqrt{\frac{5}{48}}\sin\chi\cos\theta - \frac{\cos\chi}{4}, \\ h_5 &= \sqrt{\frac{5}{6}}\sin\chi\sin\theta\sin\left(\phi + \frac{\pi}{6}\right) - \sqrt{\frac{5}{48}}\sin\chi\cos\theta - \frac{\cos\chi}{4}, \end{aligned} \tag{3.12}$$

which are exactly the ones given in [3]. For the subsequent models, we refer the reader to chapter 4, section 4.2.1 where we describe in detail the other lattices and the positions of their masses.

We can visually represent the hypersurfaces of the 6 lattices as follows: as the conformal factor ψ is a function of 3 angular coordinates, (χ, θ, ϕ), we choose a fixed $\chi = \chi_0$ coordinate and plot the surface $\psi(\chi_0, \theta, \phi)$ for each of the lattices in Figure 3.3. These hypersurfaces show that increasing the number of masses increases the degree of homogeneity already, as the tubes become smaller and contribute less to the overall geometry, and the hypersurface becomes more spherical.

Table 3.1 summarises all of the possible tilings, not just those of the 3-sphere we have considered. The final column denotes the Schläfi symbol $\{pqr\}$ where p is the number of edges to a cell face, q is the number of cell faces that meet at a corner of a cell, and r is the number of cells meeting along a cell edge. For the 3-spheres

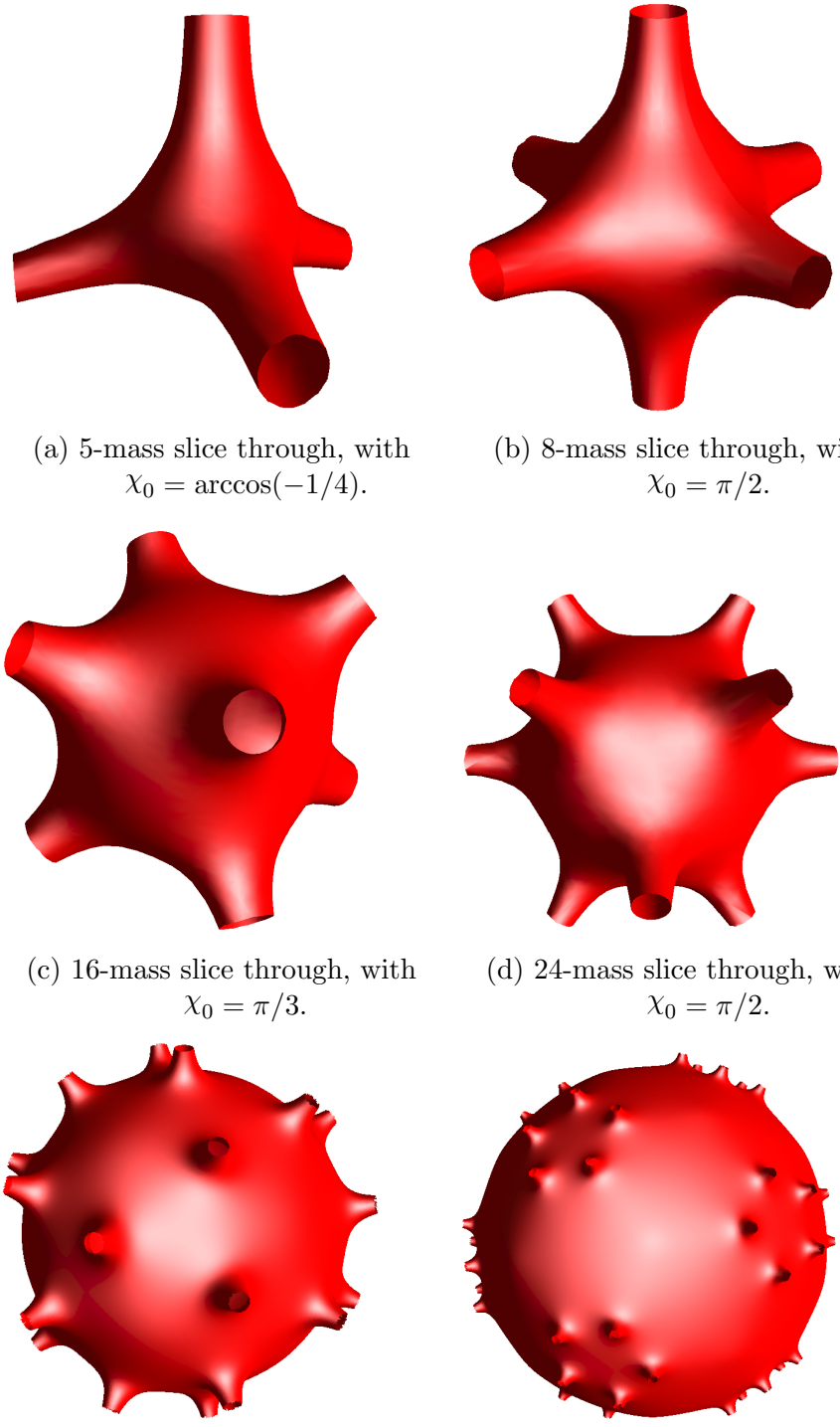

(a) 5-mass slice through, with $\chi_0 = \arccos(-1/4)$.

(b) 8-mass slice through, with $\chi_0 = \pi/2$.

(c) 16-mass slice through, with $\chi_0 = \pi/3$.

(d) 24-mass slice through, with $\chi_0 = \pi/2$.

(e) 120-mass slice through, with $\chi_0 = \pi/2$.

(f) 600-mass slice through, with $\chi_0 = \pi/2$.

Figure 3.3: Slices through the 6 lattice hypersurfaces, where the tubes represent the positions of the masses. This figure is taken from An exact quantification of backreaction in relativistic cosmology by Clifton et. al. http://dx.doi.org/10.1103/PhysRevD.86.043506, and is reproduced with permission by T. Clifton.

Nº of cells	Background Curvature	Cell Shape	Lattice Structure
5	+	Tetrahedron	{333}
8	+	Cube	{433}
16	+	Tetrahedron	{334}
24	+	Octahedron	{343}
120	+	Dodecahedron	{533}
600	+	Tetrahedron	{335}
∞	0	Cube	{434}
∞	-	Cube	{435}
∞	-	Dodecahedron	{534}
∞	-	Dodecahedron	{535}
∞	-	Icosahedron	{353}

Table 3.1: Summary of all possible tilings of 3-dimensional spaces with either constant positive (+), constant negative (-) or zero curvature (0), as well as the cells comprising the tilings and their number. The last column denotes the Schläfi symbols, which denote the number of edges to each cell face, number of cell faces meeting at a vertex, and number of cells meeting along an edge. This table is taken from [2].

we have been considering, there are only 6 ways of tiling the 3-space using a finite amount of polyhedra, whereas an infinite amount of cells are needed to tile 3-spaces with either zero or negative curvature. In section 3.2.2 we discuss work related to these infinite lattices.

Proper Mass

An important calculation of these black hole lattices is the measure of the mass of one of the black holes, which can then be used for comparisons to FLRW cosmologies. The $\tilde{m}_i$ in Equation (3.4) refers to the mass parameters of the black holes. The proper masses, however, corresponds to the mass that an observer in the asymptotically flat region on the far-side of the Einstein-Rosen bridge would infer by looking at how the gravitational field drops off at infinity. Therefore in order to calculate this, the leading order term in the metric in the limit $\chi \to 0$ is compared to the Schwarzschild geometry, where a value for the mass can be read off. The conformal factor in

Equation (3.4) in the limit $\chi_i \to 0$ is

$$\psi \to \sum_{j \neq i}^{N} \frac{\sqrt{\tilde{m}_j}}{2 \sin\left(\frac{\chi_{ij}}{2}\right)} + \frac{\sqrt{\tilde{m}_i}}{\chi_i}. \tag{3.13}$$

Defining $\hat{\chi}_i = A_i^2 \chi_i$, where A_i is the first term on the right-hand side of Equation (3.13) then gives

$$ds^2 \to \left(1 + \frac{A_i \sqrt{\tilde{m}_i}}{\hat{\chi}_i}\right)^4 \left(d\hat{\chi}_i^2 + \hat{\chi}_i^2 d\Omega_i^2\right), \tag{3.14}$$

which can be compared to Equation (3.2) to give an expression for the proper mass of the i^{th} black hole as

$$m_i = \sum_{j \neq i}^{N} \frac{\sqrt{\tilde{m}_i \tilde{m}_j}}{2 \sin\left(\frac{\chi_{ij}}{2}\right)}, \tag{3.15}$$

where the index j labels all other masses and χ_{ij} is the coordinate distance between points i and j (after rotating so that mass i appears at $\chi = 0$). We will refer back to this expression and the above derivation, as well as generalisations of it, in subsequent chapters.

Comparison with FLRW Geometry

We will now review in detail how these lattices are compared with equivalent FLRW counterpart universes [3], as again, these analyses will be repeated in subsequent chapters to come. The equivalent FLRW universes are also positively curved, and have a total proper mass equal to $M = nm$, where n is the number of masses and m is the proper mass of each. The difference lies in how this mass is distributed, instead of discrete packets, it is in the form of a perfect fluid, or dust. It is easy to show that the line element for such a universe takes the following form,

$$ds^2 = \frac{16M^2}{9\pi^2} \left(d\chi^2 + \sin^2\chi d\theta^2 + \sin^2\chi \sin^2\theta d\phi^2\right), \tag{3.16}$$

which can immediately be compared to $ds^2 = \psi^4 d\tilde{s}^2$ where ψ is given by Equation (3.4). This gives a straightforward comparison of the length of scales between the two cosmologies. As the conformal factor is a function of position, there is a degree of ambiguity in specifying this for the discrete case, therefore we can identify two natural choices. The first is to calculate the line element at a point furthest away from the masses, which in this case is given by a vertex of a cell, which we will denote D1. The second is to calculate the length of a cell edge and is denoted D2.

Cell shape	N^o masses	$\left(\frac{a_0^{\text{Discrete}}}{a_0^{\text{FLRW}}}\right)_{\text{D1}}$	$\left(\frac{a_0^{\text{Discrete}}}{a_0^{\text{FLRW}}}\right)_{\text{D2}}$
Tetrahedron	5	1.321	1.360
Cube	8	1.236	1.248
Tetrahedron	16	1.061	1.097
Octahedron	24	1.083	1.099
Dodecahedron	120	1.033	1.034
Tetrahedron	600	0.996	1.002

Table 3.2: Ratios of the scales of lattice to fluid universes for each of the two definitions D1 and D2, for different numbers of masses. This table is taken from [3].

Definition D1 gives us immediately

$$ds^{\text{Discrete}}_{\text{D1}} = \frac{\tilde{m}_i}{4}\left(\sum_{i=1}^{n} f_i^{-1}\right)^2, \tag{3.17}$$

where f_i are the source functions from Equation (3.5). Definition D2 gives us

$$ds^{\text{Discrete}}_{\text{D2}} = \int \psi^2 d\chi. \tag{3.18}$$

The results for both of these are shown in Table 3.2 for each of the 6 cosmological models. It is manifest that increasing the numbers of masses reduces the discrepancy between the scales of lattice to FLRW models, for both definitions, and thus we can conclude that for the order of a few hundred masses, backreaction remains negligible. These definitions will be returned to in later chapters, either one or both, as we generalise the existing models.

The models in [3] and introduced here have enjoyed a wide range of extensions and advancements. This includes the time evolution along specific curves [2, 82, 154], as well as the addition of extra fields, in the form of a cosmological constant [36], electric charge [37] or a scalar field [155, 156]. A novel way to include structure formation was performed in [35] whilst extending the gravitational theory itself to that of a scalar-tensor one was considered in [38].

3.2.2 Non-Time-Symmetric Hypersurfaces

Now we will briefly review the work on non-zero extrinsic curvature lattices. Several authors have investigated this route by aiming to solve the non-linear constraint

equations already introduced, Equations (2.57) and (2.58). One of the first groups was that of Yoo et al [157], who used the conformal-transverse-traceless Lichnerowicz-York scheme whereby the trace-free part of the extrinsic curvature A_{ij} is further decomposed into longitudinal and transverse trace-free parts. The latter of these is set to zero, and the hypersurface is chosen to be trivial, $h_{ij} = \psi^4 \delta_{ij}$, meaning they consider an infinite, cubic lattice with periodic boundary conditions and a black hole at the centre of each cube. Near each black hole the solution is Schwarzschild whilst at the cell faces the expansion is homogeneous and isotropic. This is ensured by choosing a piecewise function for the form of K, which varies smoothly from 0 at the centre of the cells to a constant negative value at the boundaries,

$$K = K_c T(r) = K_c \begin{cases} 0 & \text{for } 0 \leq r \leq l \\ \left(\frac{(r-l-\sigma)^6}{\sigma^6} - 1 \right)^6 & \text{for } l \leq r \leq l + \sigma \\ 1 & \text{for } l + \sigma \leq r \end{cases} , \tag{3.19}$$

where K_c, l and σ are parameters. The constraint equations were then solved numerically and compared with cosmological N-body simulations and a corresponding Einstein-de Sitter universe.

The above prescription was also used by Bentivegna and Korzyński in [158], in a conformally flat, infinite, expanding cubic lattice, with a similar choice for the trace of the extrinsic curvature. Slight differences in variable definitions and boundary conditions were used, and the constraint equations were solved numerically using the Einstein Toolkit, which utilises the BSSN formalism to evolve the initial data. They found little difference with a corresponding FLRW universe with the same initial energy density, only higher-order oscillations which affected the subsequent evolution - a possible artefact of the choice of initial data.

Numerically solving the constraint equations is not the only way to make progress in the case of non-time-symmetric initial data. In chapter 5 we demonstrate how to analytically construct lattices in the presence of a cosmological constant Λ, which means the extrinsic curvature no longer vanishes.

3.2.3 Alternative Configurations of Masses

Tessellating the 3-sphere with regular polyhedra is not the only way to construct these lattices. Work by Korzyński in [159] consisted of exact analyses of arbitrary arrangements of masses, and investigated the limit as the number of masses $n \to \infty$. The 3-sphere was divided into quasi-cubes, which were then partitioned into domains,

allowing $8k^3$ black holes where k is an integer. This meant the $n = 1$ case could be compared to the 8-mass cubic lattice we have already been introduced to. Volume averages were used to look at this continuum limit, and it was found that as $n \to \infty$, the spatial part of the metric asymptotes to a closed FLRW metric (except in the vicinity immediately around the black holes, where it was Schwarzschild), suggesting backreaction tends to zero.

More recently the field has seen interesting work by [160] and [161]. The former of these involves again, the time-symmetric S^3 lattice but with the black holes placed both randomly and regularly, so as to compare between different configurations but also to the FLRW universes. They found backreaction, as expressed by comparing the ADM masses to the total Friedmann mass, was smaller for the random configurations than for regular, with both sets approaching FLRW as the number of masses increased. The local curvature was also studied by looking at second derivatives of the metric. The work by Jolin and Rosquist [161] uses an alternative way of tessellating the 3-sphere. It is divided into 8 equally sized wedges, similar to an orange, whereby in one wedge, or cell, masses are randomly placed and the remaining cells are identical mirror images to this. Thus it can be compared to the regular 8-mass lattice if each wedge has only one black hole, but also the 16, 24, 120, and 600 cases as well as others. Analogously to the calculations used for Table 3.2, they found the FLRW limit was approached as the number of masses increased, but from below, due to the choice of tessellation. The evolution along a local rotationally symmetric curve was calculated as in [82] as well as clustered configurations. In this, the behaviour deviated from FLRW more.

In chapter 4 we provide a complementary approach to the ones discussed above, which still retains the regularity of the original lattices but looks at the effects of clusters of masses on the scale of the cosmology. This is achieved by splitting the masses up and moving them along parameterised trajectories.

3.3 Numerical Approaches

Finally, the 8-mass cubic S^3 lattice was numerically evolved in full for the first time by Bentivegna and Korzyński in [162]. The initial data was set up in the same way as in [3], whilst the full evolution was carried out using the Einstein Toolkit. The length of a cell edge as a function of proper time was calculated and matched the corresponding FLRW evolution up to a time where resolution was lost and numerical errors became too large. Finally, the total effective mass was approximately 25%

larger than the sum of ADM masses of the black holes, suggesting this particular lattice initial data mimicked FLRW but only if there existed a quarter more mass than that of the black holes alone.

4 A Quasi-Static Approach to Structure Formation

This chapter is based on [35].

4.1 Introduction

The lattices described in chapter 3 are artificial toy models and contain many symmetries, as they are one of the six regularly arranged models. We can begin to relax the regularity and assumption of perfectly equidistant spacing by positioning the masses differently in order to create clusters of masses, or *structure*. This will allow for larger numbers of black holes to be considered, and for the effects of clustering of the black holes to be studied. Our aim here is to perform a controlled investigation of the effects that clusters of masses have on the scale and properties of the cosmology within these black hole lattices. While such situations are still far too simple to model the full hierarchy of structures in the real Universe, they do provide a well-defined way to study some of the questions involving coarse-graining and average expansion. The approach we will follow in this paper adds an extra level of structure to these models, so that they essentially have three length scales: (i) the curvature radius of each of the black holes, (ii) the radius of a cluster of black holes, and (iii) the cosmological curvature scale.

The growth of structure has long been speculated to be a potential cause of deviations from the predictions of FLRW cosmology in the real Universe [163], and our models provide a type of quasi-static approximation that could be used to test some of these ideas within the context of exact solutions to Einstein's field equations at moments of instantaneous staticity. This chapter builds on the work involving hierarchical structures that was recently performed in a similar context in [130], as well as the random distributions of black holes that were considered in [159]. As with these previous studies, we find situations in which hierarchies of structures can significantly alter the large-scale properties of the universe. We interpret these

findings in terms of the gravitational interaction energies between massive bodies, and the effects that they have on cosmology.

The rest of this chapter is organised as follows: in section 4.2 we describe the method used to split each mass up into a cluster of masses. Section 4.3 then contains calculations of the positions of the different apparent horizons (individual and collective). The results of this are then used to calculate three different mass parameters in section 4.4.1, and to derive expressions for the different interaction energies in section 4.4.2. In section 4.5 we compare our black hole universe models to their FLRW counterparts and to each other, in order to investigate the effect of the clustering of masses, before discussing our findings in section 4.6

4.2 Creating Clusters of Masses

We create structure in a very specific and precise way such that our initial data solves the constraint equations exactly whilst still being relatively simple analytically. For each of the 6 lattice models, we take each of the black holes that are sitting at the centre of their polyhedra, and split (or explode) them into a number of further masses. Specifically, the number of masses they are split into is the number of vertices of the polyhedra used to construct that lattice. The individual black holes are then moved along parameterised trajectories towards these vertices. Our basic aim is to be able to consider instants of time at which the black holes will be positioned at different points along the curves that connect the centres of our lattice cells to their vertices. We have euphemistically referred to this as 'moving' the black holes along these trajectories, but the reader should be aware that what we are really doing is comparing different configurations of black hole positions in different universes, each at their maximum of expansion. We consider this to be a type of quasi-static approach to structure formation, where the dynamics themselves are neglected, but the consequences of clustering in these instantaneously static configurations can be explored in detail (akin to the study in [164], where instantaneously static black holes at different spatial separations in an asymptotically flat space were compared).

The trajectories we are considering are examples of the locally rotationally symmetric curves identified in [82]. These are curves about which the lattices are symmetric under rotations by a discrete angle, e.g. the length of a cell edge. At least two reflection symmetric planes will always intersect along each of these paths [2], and the property than any reflection symmetric surface is totally geodesic [165] means that these trajectories must themselves be geodesics in the geometry of the initial

3-space. This follows for both the full geometry and the conformal geometry. In terms of parameterising these trajectories, it is more straightforward to consider them in the 3-sphere geometry that constitutes the conformal space. We therefore require $\ddot{x}^\mu + \widetilde{\Gamma}^\mu_{\rho\sigma}\dot{x}^\rho\dot{x}^\sigma = 0$ along each trajectory, where $\tilde{\Gamma}^\mu_{\rho\sigma}$ are the Christoffel symbols for the round metric of a 3-sphere, and over-dots are derivatives with respect to an affine parameter.

A simple way to determine the position at any point along our chosen trajectories is to label the position 4-vector in the Euclidean embedding space at any point along the path as v, and to parameterise the trajectory itself by λ, such that

$$v(\lambda) = (1-\lambda)v_{original} + \lambda v_{dual} \tag{4.1}$$

where v_{original} is the original position of one of the masses in the regular lattice, and v_{dual} is the position of one of the masses in the dual lattice (or, equivalently, one of the vertices in the original lattice). Every point along the trajectory is then given by a unique value of $\lambda \in [0, 1]$. This choice of parameterisation has been made so that at $\lambda = 0$ the new masses have not been moved from the original position of the black holes in the original lattice, and so that at $\lambda = 1$ they have been moved the maximal amount (and are therefore at the positions of one of the masses in the dual lattice). Thus, the analysis of regular lattice configuration performed in [3] becomes the limiting case, when $\lambda = 0$ or 1.

To illustrate this concept further, consider the 8-mass model. It is comprised of 8 cubes, each of which has 8 vertices. Therefore 8 black holes at the centre of each of these cubes is split up into a further 8, giving a model with 64 black holes. It turns out that due to the topology of these lattices, 4 black holes then meet at any vertex. When all the black holes are at their specified v_{dual} positions, there are only 16 separately identifiable black holes, as 4 black holes have met at each endpoint. The 8-mass model and the 16-mass model are therefore dual to one another. For some of the other lattices this is not the case, as shown in Table 4.1, where we list each of the configurations, the cell shape, and the resulting number of black holes.

Original N^o	Cell shape	N^o vertices	Total N^o	Dual N^o
5	Tetrahedron	4	20	5
8	Cube	8	64	16
16	Tetrahedron	4	64	8
24	Octahedron	6	144	24
120	Dodecahedron	20	2400	600
600	Tetrahedron	4	2400	120

Table 4.1: The numbers of masses for each of the models (original, total and dual) and the number of vertices of a single cell.

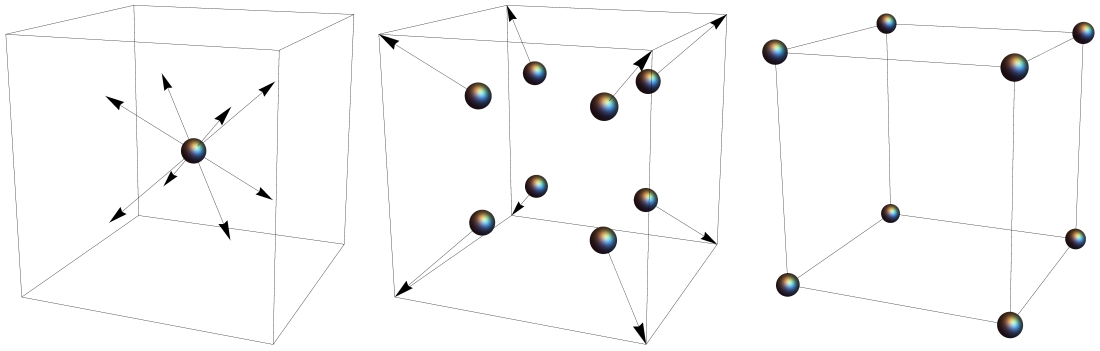

(a) $\lambda = 0$. (b) $\lambda = 0.5$. (c) $\lambda = 1$.

Figure 4.1: A single mass at the centre of a cube in the 8-mass model is split into a further 8 masses which are moved along trajectories parameterised by λ.

A schematic representation of the splitting up process for one of the black holes in the 8-mass model described previously can be seen in Figure 4.1, where we show three instances along the trajectory: the initial point, $v_{original}$ at $\lambda = 0$, the midpoint at $\lambda = 0.5$, and the endpoint v_{dual} at $\lambda = 1$. Figure 4.1 should be used for conceptual understanding only, as topologically the black holes are not being moved along trajectories in flat Euclidean space. Instead they are moving along the surface of a 3-sphere. To illustrate this more accurately we show a dimensionally reduced version of the same process in Figure 4.2. We suppress one dimension to show initially 6 black holes on the surface of a 2-sphere at $\lambda = 0$, represented by the black dots. Increasing λ then sees each of these 6 black holes split into a further 4, and these follow individual trajectories on the surface of this 2-sphere as λ increases. For values of λ approaching 1, the black holes end up at their endpoints of their trajectories, specifically 3 meet at each end point, to show 8 black holes in the final picture at

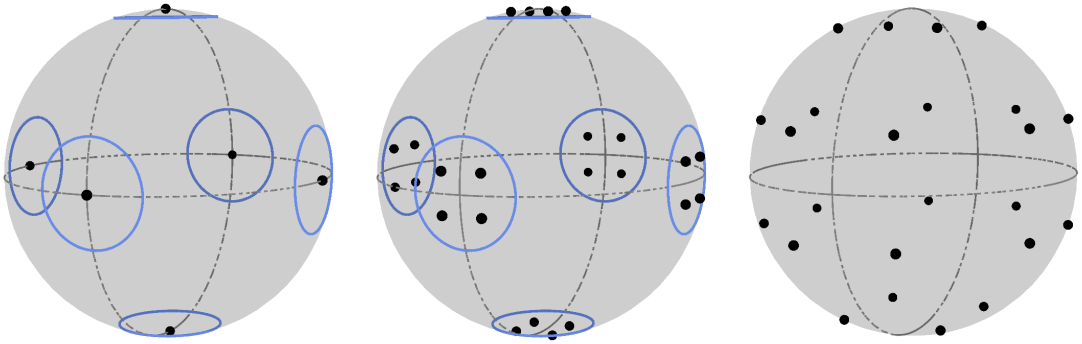

(a) $\lambda = 0$. (b) $\lambda \sim \lambda_{\text{crit}}$. (c) $\lambda = 0.5$.

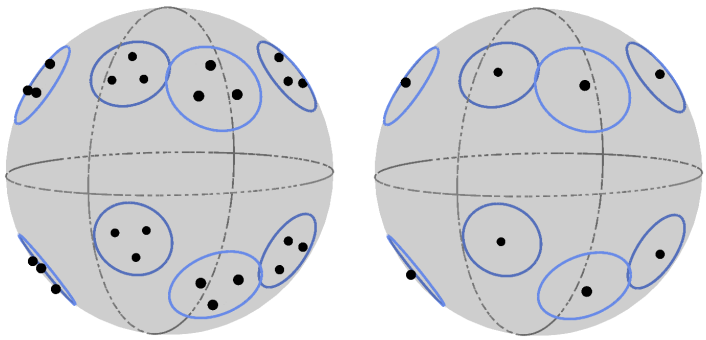

(d) $\lambda \sim \lambda_{\text{crit}}$. (e) $\lambda = 1$.

Figure 4.2: A dimensionally reduced depiction of the $8 \to 16$-mass case where the masses move along trajectories parameterised by λ. For values of λ close to a critical value of λ, collective horizons encompass the black holes, shown by the blue rings, which vanish as they move further apart.

$\lambda = 1$, which is a dimensionally reduced version of the 16-mass model. The blue rings which can be seen for values of λ close to 0 or 1 are *collective horizons*, which are explained in more detail later and only occur for values of λ close to 0 or 1.

4.2.1 Lattice Configurations

We will now look in more detail at each of the 4 different configurations:

$5 \to 5$-Mass Model

The original 5-mass model is the higher-dimensional equivalent of a tetrahedron and is known as a 4-simplex. It can be created by taking the vertices of a regular tetrahedron and adding a new one that is equidistant from the other 4. An example

set of these 5 vertices can be written in Cartesian $(w,\, x,\, y,\, z)$ coordinates as

$$\begin{aligned} &i) \quad (1,0,0,0), \\ &ii) \quad \sqrt{\frac{5}{16}}\left(-\frac{1}{\sqrt{5}},1,1,1\right), \\ &iii) \quad \sqrt{\frac{5}{16}}\left(-\frac{1}{\sqrt{5}},1,-1,-1\right), \\ &iv) \quad \sqrt{\frac{5}{16}}\left(-\frac{1}{\sqrt{5}},-1,1,-1\right), \\ &v) \quad \sqrt{\frac{5}{16}}\left(-\frac{1}{\sqrt{5}},-1,-1,1\right), \end{aligned} \tag{4.2}$$

where it is clear that the $(x,\, y,\, z)$ coordinates of vertices $ii)$ to $v)$ are the vertices of a regular tetrahedron centred at $(0,\, 0,\, 0)$. Thus position $i)$ is this new vertex which creates the 4-simplex and is equidistant from the others. The 5-mass model is self dual, which means when we perform the splitting up process and eventually set $\lambda = 1$, we also recover another 5-mass model. As a result, in our formalism the black holes were originally at the centres of their cells, or tetrahedra, and move to each of the vertices of the tetrahedra, but both are equivalently 5-mass models. Thus we can interchange the positions of the vertices with the positions of the centres of the cells. This means we can think of Equation (4.2) as the positions of the masses at $\lambda = 0$, i.e. at the centre of their tetrahedra. It is now straightforward to find the dual positions, or new vertices that the black holes will be moved to. This is by done reflecting the positions of the 5 locations above in the four planes given by $w = 0$, $x = 0$, $y = 0$ and $z = 0$ or equivalently putting a minus sign in front of each of the above coordinates. Thus our dual lattice has masses at the following positions:

$$\begin{aligned} &i) \quad (-1,0,0,0), \\ &ii) \quad \sqrt{\frac{5}{16}}\left(\frac{1}{\sqrt{5}},-1,-1,-1\right), \\ &iii) \quad \sqrt{\frac{5}{16}}\left(\frac{1}{\sqrt{5}},-1,1,1\right), \\ &iv) \quad \sqrt{\frac{5}{16}}\left(\frac{1}{\sqrt{5}},1,-1,1\right), \\ &v) \quad \sqrt{\frac{5}{16}}\left(\frac{1}{\sqrt{5}},1,1,-1\right). \end{aligned} \tag{4.3}$$

We will now look in detail at the trajectory of one of the black holes. Consider the mass at position i) in Equation (4.2). It is split into 4 masses and these move to positions ii), iii), iv) and v) in Equation (4.3). This sets $v_{original} = (1,\, 0,\, 0,\, 0)$ and let us choose $v_{dual} = \sqrt{\frac{5}{16}}\left(\frac{1}{\sqrt{5}}, -1, -1, -1\right)$. Substituting these into Equation (4.1) gives

$$\begin{aligned} v(\lambda) &= (1-\lambda)(1,0,0,0) + \lambda\sqrt{\frac{5}{16}}\left(\frac{1}{\sqrt{5}}, -1, -1, -1\right) \\ &= \left(1 - \frac{3\lambda}{4}, -\lambda\sqrt{\frac{5}{16}}, -\lambda\sqrt{\frac{5}{16}}, -\lambda\sqrt{\frac{5}{16}}\right) . \end{aligned} \tag{4.4}$$

Before we proceed further it should be pointed out that this path and its more general form Equation (4.1) are straight lines, or chords, that cut directly through the embedding space E^4. We instead require that our masses travel along the surface of the 3-sphere along geodesic arcs, and impose this constraint by first writing a general trajectory in hyperspherical coordinates instead of Cartesian. This gives

$$v(\lambda) = (r\cos\chi, r\sin\chi\cos\theta, r\sin\chi\sin\theta\cos\phi, r\sin\chi\sin\theta\sin\phi)\,, \tag{4.5}$$

where r, χ, θ and ϕ will be functions of λ. Recognising that a position on the chord has the same angular coordinates as a corresponding position on the arc, and that the 3-sphere is a unit 3-sphere with $r = 1$ allows us to write the new trajectory along the arc $v'(\lambda)$ as

$$v'(\lambda) = (\cos\chi, \sin\chi\cos\theta, \sin\chi\sin\theta\cos\phi, \sin\chi\sin\theta\sin\phi), \tag{4.6}$$

where $\chi = \chi(\lambda)$, $\theta = \theta(\lambda)$ and $\phi = \phi(\lambda)$ are obtained from transforming the $(w,\, x,\, y,\, z)$ coordinate positions from Equation (4.1) into hyperspherical coordinates. Returning to our worked example, we have that

$$(w,\, x,\, y,\, z) = \left(1 - \frac{3\lambda}{4}, -\lambda\sqrt{\frac{5}{16}}, -\lambda\sqrt{\frac{5}{16}}, -\lambda\sqrt{\frac{5}{16}}\right), \tag{4.7}$$

which gives,

$$\chi(\lambda) = \arccos\left(1 - \frac{3\lambda}{4}\right), \tag{4.8a}$$

$$\theta(\lambda) = \arccos\left(\frac{-\lambda\sqrt{\frac{5}{16}}}{\sin\chi(\lambda)}\right), \tag{4.8b}$$

$$\phi(\lambda) = \arccos\left(\frac{-\lambda\sqrt{\frac{5}{16}}}{\sin\chi(\lambda)\sin\theta(\lambda)}\right). \tag{4.8c}$$

These functions can be substituted into Equation (4.6) to give the trajectory for the mass, paramaterised by λ. For one mass, there are 3 functions to be calculated, described by Equations (4.8a), (4.8b) and (4.8c). There are 3 other trajectories emanating from this starting point which we did not consider, with their own functions, as well as the 4 remaining black holes in this model. This means there is a total of 60 functions. For the largest mass model, there are 2400 x 3 = 7200 functions to be calculated.

8 → 16-Mass Model

The positions of the masses in the 8-mass model are given by all permutations of the following:

$$(w, x, y, z) = (\pm 1, 0, 0, 0)\,. \tag{4.9}$$

A full list of the positions of the 8 masses, as well as their (χ, θ, ϕ) coordinates, is given in Table 4.2. The dual of the 8-mass lattice, the 16-mass model, has its mass positions at all permutations of:

$$(w, x, y, z) = \frac{1}{2}(\pm 1, \pm 1, \pm 1, \pm 1)\,. \tag{4.10}$$

Consider the mass at position $\frac{1}{2}$(1, 1, 1, 1) in the 16-mass model. This is split into 4 masses, each of which moves towards one of the following vertices of the 8-mass model: (1, 0, 0, 0), (0, 1, 0, 0), (0, 0, 1, 0) and (0, 0, 0, 1), as these are its nearest vertices.

Mass number	$(w,\, x,\, y,\, z)$	$(\chi,\, \theta,\, \phi)$
$i)$	$(1,\, 0,\, 0,\, 0)$	$(0,\, \frac{\pi}{2},\, \frac{\pi}{2})$
$ii)$	$(-1,\, 0,\, 0,\, 0)$	$(\pi,\, \frac{\pi}{2},\, \frac{\pi}{2})$
iii	$(0,\, 1,\, 0,\, 0)$	$(\frac{\pi}{2},\, 0,\, \frac{\pi}{2})$
$iv)$	$(0,\, -1,\, 0,\, 0)$	$(\frac{\pi}{2},\, \pi,\, \frac{\pi}{2})$
$v)$	$(0,\, 0,\, 1,\, 0)$	$(\frac{\pi}{2},\, \frac{\pi}{2},\, 0)$
$vi)$	$(0,\, 0,\, -1,\, 0)$	$(\frac{\pi}{2},\, \frac{\pi}{2},\, \pi)$
$vii)$	$(0,\, 0,\, 0,\, 1)$	$(\frac{\pi}{2},\, \frac{\pi}{2},\, \frac{\pi}{2})$
$viii)$	$(0,\, 0,\, 0,\, -1)$	$(\frac{\pi}{2},\, \frac{\pi}{2},\, \frac{3\pi}{2})$

Table 4.2: Coordinates $(w,\, x,\, y,\, z)$ of the 8 masses in the embedding space E^4, as well as $(\chi,\, \theta,\, \phi)$ in the lattice. This table is taken from [3].

24 → 24-Mass Model

The coordinates of the masses in the original 24-mass model are given as all possible permutations of

$$(w, x, y, z) = \frac{1}{\sqrt{2}}(\pm 1, \pm 1, 0, 0)\,. \tag{4.11}$$

As this configuration is self-dual, the model at $\lambda = 1$ also has 24 masses, but at the dual vertex positions. These are given by Equations (4.9) and (4.10).

120 → 600-Mass Model

The positions of the masses for the 120-mass model are also given by Equations (4.9) and (4.10), as well as 96 masses located at all even permutations of

$$(w, x, y, z) = \frac{1}{2}(\pm\varphi, \pm 1, \pm\varphi^{-1}, 0)\,, \tag{4.12}$$

where $\varphi = (1 + \sqrt{5})/2 = 1.618\ldots$ is the golden ratio. The dual of this lattice is the 600-mass model, with masses located at all permutations of

$$\frac{1}{\sqrt{8}}(0,0,\pm 2,\pm 2), \tag{4.13a}$$
$$\frac{1}{\sqrt{8}}(\pm 1,\pm 1,\pm 1,\pm\sqrt{5}), \tag{4.13b}$$
$$\frac{1}{\sqrt{8}}(\pm\varphi^{-2},\pm\varphi,\pm\varphi,\pm\varphi), \tag{4.13c}$$
$$\frac{1}{\sqrt{8}}(\pm\varphi^{-1},\pm\varphi^{-1},\pm\varphi^{-1},\pm\varphi^{2})\,, \tag{4.13d}$$

and all even permutations of

$$\frac{1}{\sqrt{8}}(0,\pm\varphi^{-2},\pm 1,\pm\varphi^{2}), \tag{4.14a}$$
$$\frac{1}{\sqrt{8}}(0,\pm\varphi^{-1},\pm\varphi,\pm\sqrt{5}), \tag{4.14b}$$
$$\frac{1}{\sqrt{8}}(\pm\varphi^{-1},\pm 1,\pm\varphi,\pm 2)\,. \tag{4.14c}$$

In Figures 4.3 to 4.6 we plot the slices through the hypersurfaces for some of these different configurations, at different values of λ. We display the full sequence of $\lambda = 0$ continuously through to $\lambda = 1$ for the first two lattice configurations, 5 to 5 and 8 to 16 masses, whilst for the two remaining configurations, 24 to 24, and 120 to 600 masses, we only show 2 hypersurfaces for brevity.

4.3 Apparent Horizons

We now have a method to place mass points at arbitrary positions along the curves that connect the centres and vertices of lattice cells, and so have a basis for cosmological models that simultaneously allows for clustering on small scales, while maintaining a degree of statistical homogeneity and isotropy on large scales. It remains to demonstrate that the new objects in question really are black holes. In this section we consider the problem of identifying the positions of apparent horizons within our exact initial data. This is sufficient to demonstrate the existence of black holes and a cosmological region. The positions of black hole horizons are particularly important in the models we will be discussing, as the possible merging or sharing of horizons could change the number of black holes that an observer in the cosmological region of the space infers. It could even impact upon the existence of a cosmological region at all. For our models to represent cosmological models we require that the horizons

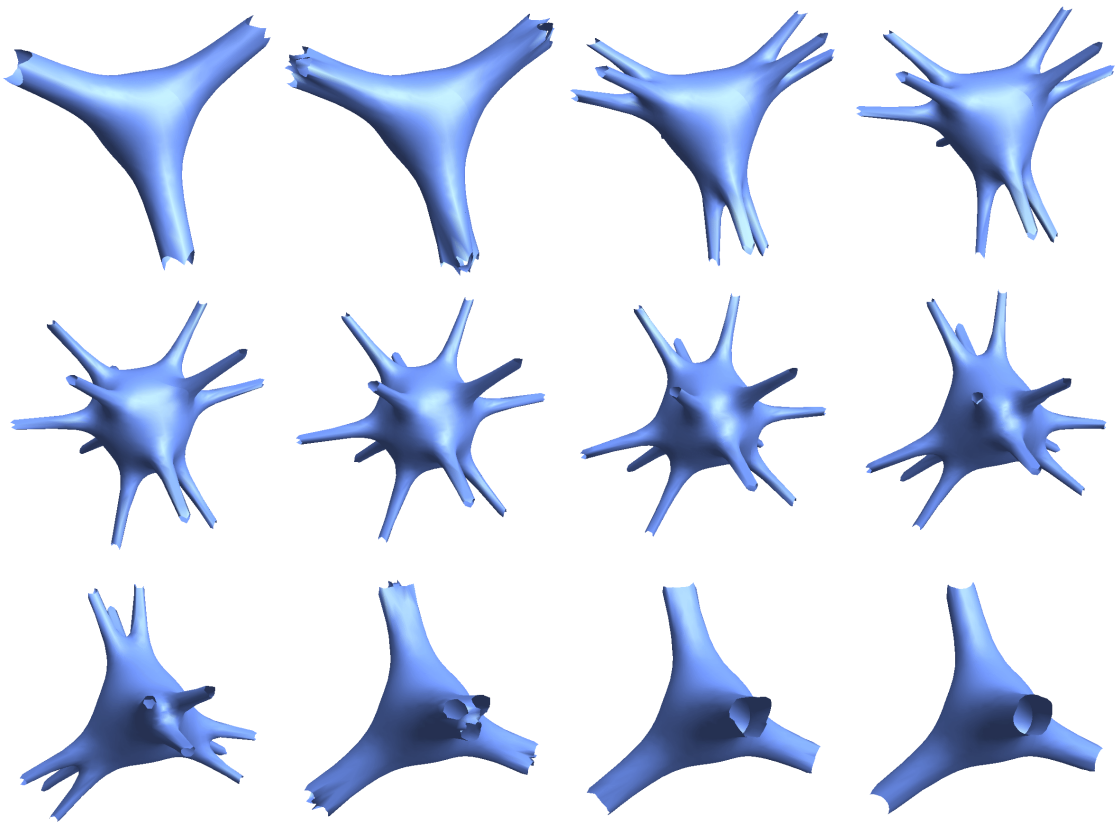

Figure 4.3: Slices through the hypersurfaces of the 5 to 5-mass configuration, at different values of λ, from left to right, top row to bottom row. The first image is at $\lambda = 0$, the sixth image is where $\lambda = 0.5$ and the final image is at $\lambda = 1$. The tubes indicate positions of masses, and the first and final images are duals to each other.

of neighbouring black holes should remain distinct and not overlap. We will call a region of space *cosmological* if it is entirely bounded by apparent horizons, and is not in causal contact with any asymptotically flat region of space. Any timelike observer in such a cosmological region will then be able to directly infer the presence of black holes, through the influence of their gravitational field, but will not be able to relocate themselves to a region that is arbitrarily far from all of them. The number of black holes in this cosmological region, as determined by the observer, will be equal to the number of distinct, closed, marginally outer trapped surfaces that bound it.

An interesting complication that arises is that if these objects are brought close enough together then an extra apparent horizon can appear, which encompasses them both. The black holes retain their own individual horizons but also acquire

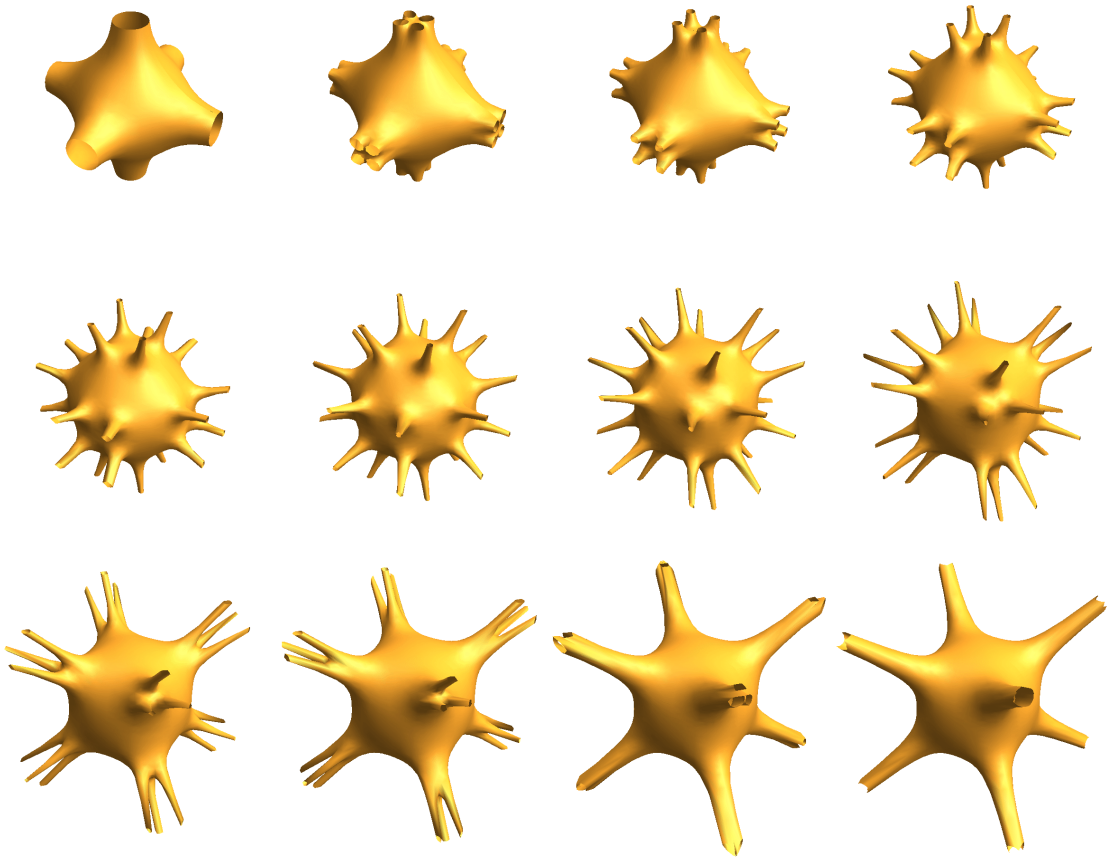

Figure 4.4: Slices through the hypersurfaces of the 8 to 16-mass configuration, at different values of λ, from left to right, top row to bottom row. The first image is at $\lambda = 0$ (the 8-mass model), the sixth image is where $\lambda = 0.5$ and the final image is at $\lambda = 1$ (the 16-mass model). Again the tubes indicate positions of masses, and the first and final images are duals to each other.

this new shared horizon. An analogous phenomenon is already well known for two black holes sufficiently close enough to each other in an asymptotically-flat space [164, 166], see Figure 4.7, but brings some new twists in the cosmological context. In this section we describe the two analytical methods used to compute the locations of these horizons and the critical values of λ where this collective horizon disappears for each of the 4 configurations.

Recall from chapter 2 that apparent horizons are defined as marginally outer trapped surfaces. This then means that expansion of the outward-pointing null normal to the surface should have vanishing expansion, so that $\nabla_\mu k^\mu = 0$. Here we will use two different techniques which contain complementary information about the properties of the apparent horizon, and that can be used together to give a measure

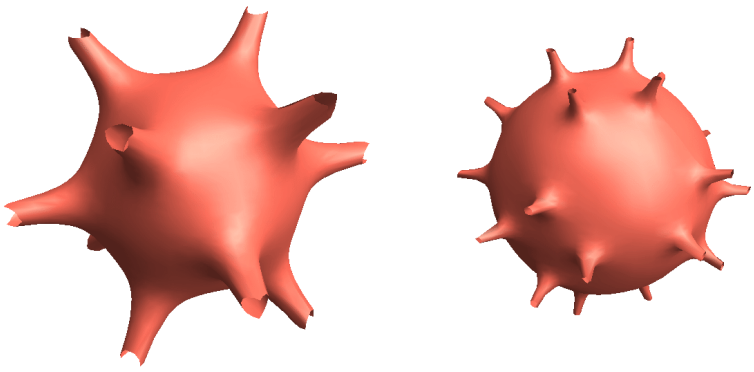

Figure 4.5: Slices through the hypersurfaces of the self dual 24-mass model. The first image on the left is at $\lambda = 0$ and the second image on the right is at $\lambda = 0.5$, a model with 144 masses.

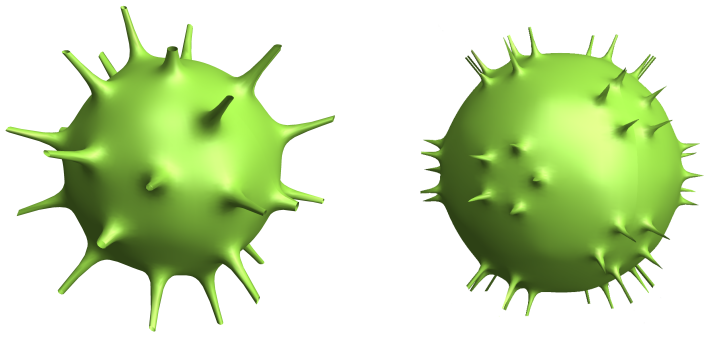

Figure 4.6: Slices through the hypersurfaces of the 120 to 600-mass configuration. The first image on the left is at $\lambda = 0$ (the 120-mass model) and the second image on the right is at $\lambda = 1$ (the 600-mass model).

of asphericity in its shape. We will refer to these as the area method and the Weyl tensor method, and they proceed as follows:

4.3.1 Area Method

If the gravitational field in the vicinity of each black hole is close to spherically symmetric then one way of estimating the position of the apparent horizon is to approximate it as being a sphere in the conformal geometry, with constant radial coordinate $\chi = \chi_h$. The position of this sphere can be found by considering concentric shells centred on a mass, with different values of χ, and then determining the value

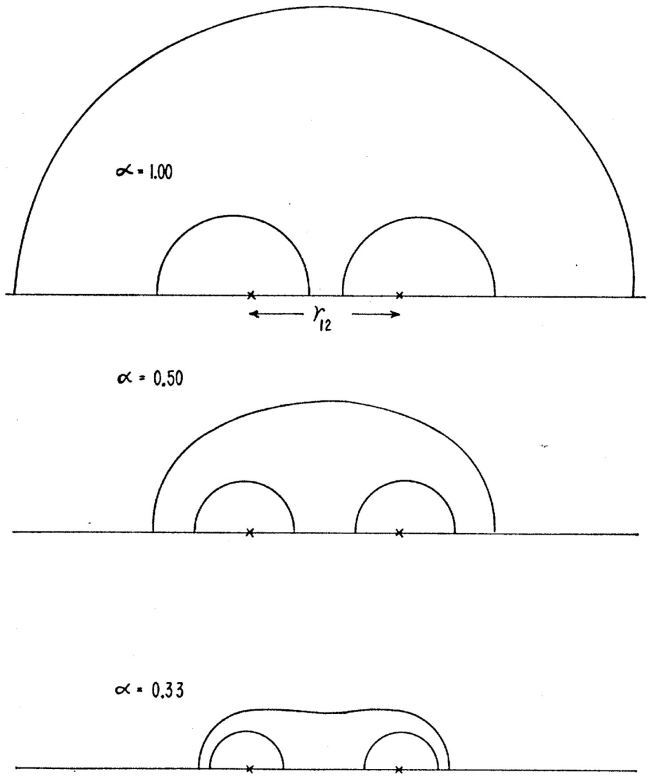

Figure 4.7: Minimal surfaces for two equal mass uncharged black holes, represented by the crosses, separated by distance r_{12}. The surfaces are calculated for three different values of the mass to separation ratio parameter, α. This figure is taken from Interaction Energy in Geometrostatics by Brill and Lindquist http://dx.doi.org/10.1103/PhysRev.131.471, and is reproduced with permission by D. Brill.

of χ that gives a sphere with the minimum area, as measured by evaluating

$$A(\chi) = \int_0^{2\pi} \int_0^{\pi} \psi^4 \sin^2(\chi) \sin(\theta) d\theta d\phi \,. \tag{4.15}$$

The benefit of this method is that it is relatively simple and that it gives us an approximation for the position of the apparent horizon in every direction away from the centre of the black hole. The drawback is that it should only be expected to be accurate when the black hole horizon is close to spherical. From Figure 4.7 it is clear that as the black holes move further apart, the shape of the collective horizon becomes distorted and so our approximation may break down.

4.3.2 Weyl Tensor Method

To more accurately determine the positions of the horizons in our initial data we can examine the constraint equations, as we did in chapter 2. Recall a relevant constraint equation for locating the horizons in terms of the electric part of the Weyl tensor was given by Equation (2.72). At the location of an apparent horizon we know from Equation (2.69) that $\nabla_\mu e_1^\mu = 0$, which in turn implies that $a_1 = 0$. We can also locate positions on the apparent horizon where $E_3^3 = E_2^2$. This means that if we arrange our coordinate system so that $\mathbf{e}_1 = \psi^{-2}\partial_\chi$ points along locally rotationally symmetric curves obeying these properties then a necessary condition for determining the location of an apparent horizon is given by

$$\mathbf{e}_1(E^{11}) = 0 \qquad \text{or, equivalently,} \qquad \frac{1}{\psi^2}\frac{\partial}{\partial\chi}(\psi^{-4}\mathcal{R}_{\chi\chi}) = 0\,, \tag{4.16}$$

where we have used $\mathbf{e}_1 = \psi^{-2}\partial_\chi$. In other words, if we plot E^{11} or $\psi^{-4}\mathcal{R}_{\chi\chi}$ along a locally rotationally symmetric curve parameterised by χ, then marginally outer trapped surfaces will be located at the points at which this function is extremised. This method is expected to be more precise than the area method outlined above but is only sufficient to locate the points at which the horizon intersects locally rotationally symmetric curves.

We can use this expression to find the locations of the horizons, both shared and individual, as well as calculate the critical values for λ for which the shared horizon vanishes. Considering the 5-mass configuration, we calculate the relevant component of the electric part of the Weyl tensor along a curve that connects the centre of one of the cells with a vertex. We do this for different values of λ, specifically $\lambda = 0$, 0.05, 0.1, 0.2, 0.3, 0.4 and 0.5, and display these results in Figure 4.8. To produce these plots we initially rotated the lattice so that a mass appeared at $\chi = 0$. Then, Equation (4.16) tells us that the horizons are located at the maxima or minima of these curves. Initially, at $\lambda = 0$, there is one maxima, located at $\chi \approx 0.4$, which we identify as the apparent horizon of the 4 black holes that are essentially lying on top of each other, at the centre of the cell. At $\lambda = 0.05$, when these 4 black holes have moved a small distance apart, we see the appearance of two more maxima close to $\chi = 0$, which we identify as the black hole's individual horizons either side. The original previous horizon at $\chi = 0.4$ is thus identified as the collective horizon. At $\lambda = 0.1$, this horizon has disappeared and we are left with only the individual horizons, which are still seen in the remaining figures. We note that there are multiple different points that satisfy Equation (4.16), represented by the different maxima

Nº of masses in original lattice	Critical value at which shared horizons vanish, λ_{crit}
5	0.077
8	0.061
16	0.021
24	0.019
120	0.007
600	0.002

Table 4.3: Numerical values for λ_{crit}, to three decimal places.

and minima along the curve, see Figure 4.8b, however it is only the maxima we identify as horizons, as demonstrated in the above discussion.

4.3.3 Comparison Between Methods

Unlike the Weyl tensor method, the area method is unable to provide the critical value of λ at which the collective horizon we are looking for disappears. This is because a minimal sphere of constant χ can always be found around any number of black holes, even though in reality it may be far from spherical. Figure 4.9 shows a comparison of the two methods for illustrative purposes for the 5-mass configuration. We show the position of one of the black holes originally at $\chi = 0$ moving outwards radially (black line), as well as its own individual horizons (green and orange lines). To produce this plot we have extracted out the positions of the maxima in Figure 4.8 as well as for other values of λ. It is clear that the collective horizon found using the area method does not disappear (red line), unlike the blue line which is the same quantity but calculated using the Weyl method, and as expected, tends towards the location of the individual horizon when the black hole is far from its neighbours.

4.3.4 Critical Values of λ

The value of λ_{crit} can be calculated for each of the models we are considering and the results in Table 4.3 show these values for each of the 6 lattices, that is, the 4 configurations we have been considering but the 6 different models within them. It is clear that increasing the number of masses decreases the amount of separation needed before the black holes lose their collective horizon, and can be considered separate. This is due to the decreasing contribution from each mass to the overall

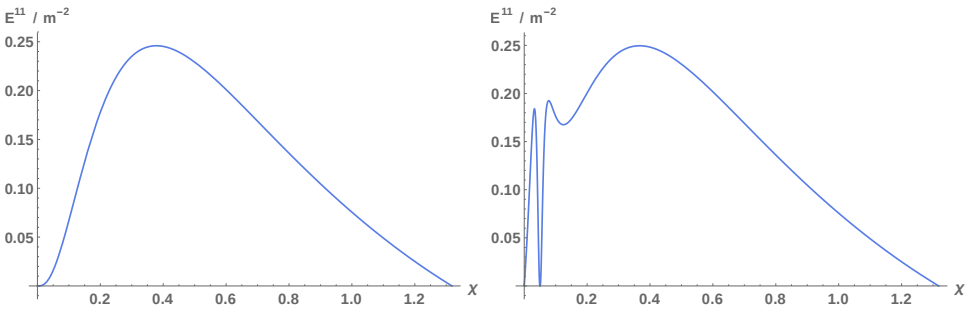

(a) $\lambda = 0$.

(b) $\lambda = 0.05$.

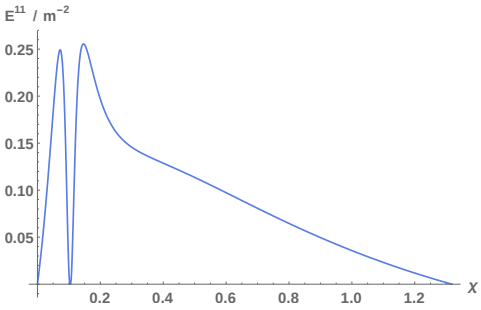

(c) $\lambda = 0.1$.

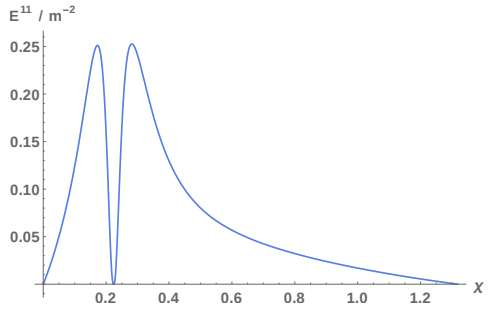

(d) $\lambda = 0.2$.

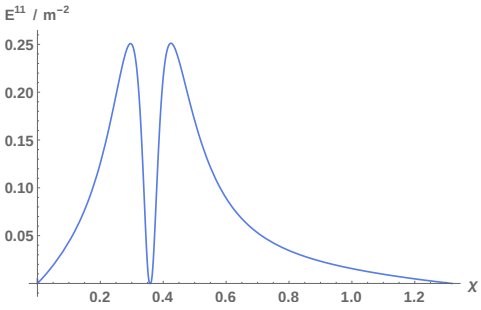

(e) $\lambda = 0.3$.

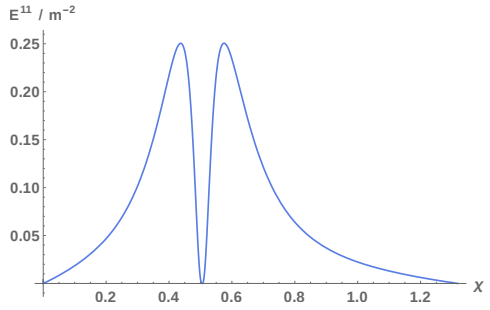

(f) $\lambda = 0.4$.

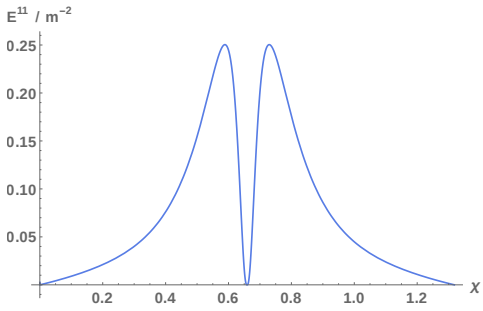

(g) $\lambda = 0.5$.

Figure 4.8: The value of E^{11} along locally rotationally symmetric curves, for different values of λ in the 5-mass lattice. E^{11} is presented here in units of m^{-2}, where m is the proper mass of each of the black holes.

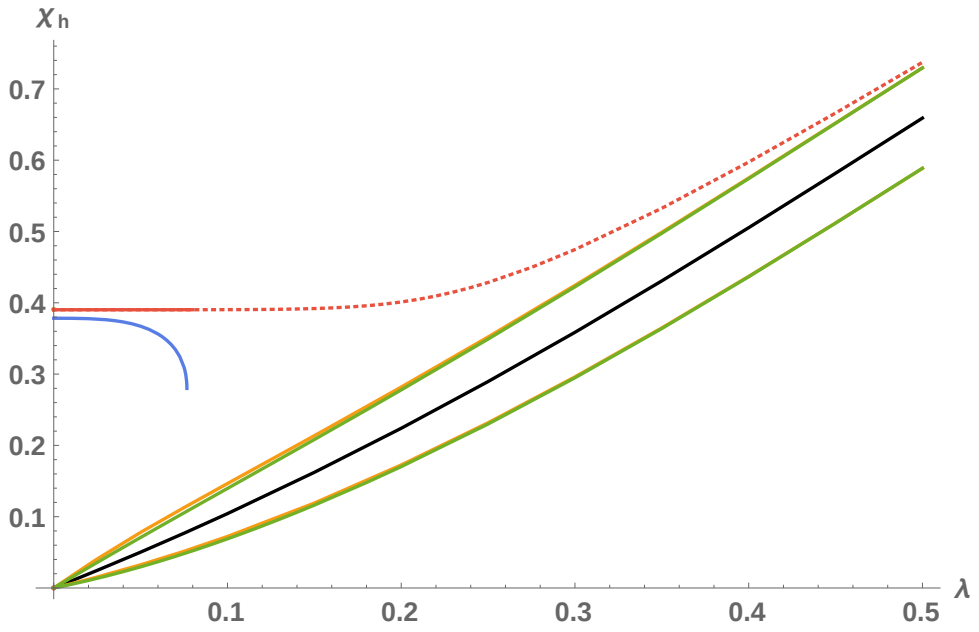

Figure 4.9: The values of χ_h for both individual and shared horizons at different values of λ for the 5-mass case. The blue and red lines are the collective horizons from the Weyl and area methods, respectively. The dashed line indicates that this horizon only exists for values of λ up to λ_{crit}, but can always be found using the area method. We plot the position of one of the black holes as it moves radially outward from $\chi = 0$, shown by the black line. The orange and green lines are largely indistinguishable, and show the individual horizon either side of this black hole, calculated using the Weyl and area method respectively.

geometry.

Calculating where these shared horizons vanish is necessary for the comparison of these configurations to their FLRW counterparts, the results of which are presented in section 4.5. This is because the total number of masses is used to perform the comparison, and depending on the value of λ as we have seen, this will change the effective number of masses an observer in the cosmology will see. For the 5-mass case for example, as long as $\lambda > \lambda_{\text{crit}}$, there are 20 separated black holes. If $\lambda < \lambda_{\text{crit}}$, these are clustered into groups of 4, each cluster having a collective horizon. This means we are now considering an effective 5-mass model, as we cannot infer the presence of the 4 individual black holes residing within a cluster. A consequence of this is that we will need to explicitly define these different masses, which we will do in the next section.

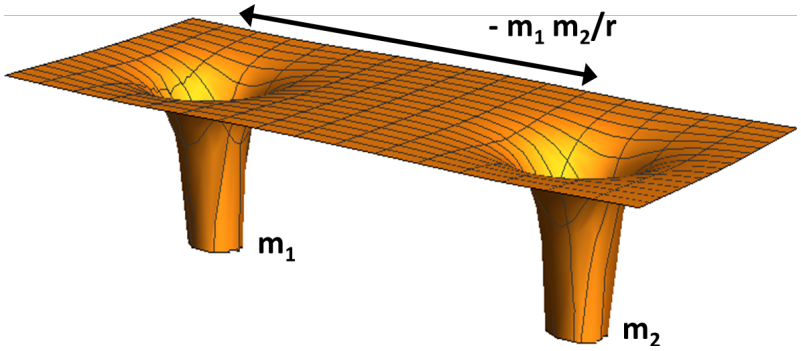

Figure 4.10: Two black holes of mass m_1 and m_2, separated by distance r and the gravitational interaction between them, $-m_1m_2/r$. The total gravitational mass of the system is equal to the sum of the masses together with the gravitational interaction.

4.4 Mass Parameters and Interaction Energies

In order to compare our models to Friedmann cosmologies we need to assign some concept of mass to our lattice structures, and define the masses within them. This can be tricky for our cosmological purposes as cosmological models (by construction) do not have asymptotically flat regions from which to view the gravitational fields of masses or clusters of masses. Further complications arise for these particular models because it is known that gravitational interaction energies themselves gravitate, see Figure 4.10, therefore care must be taken when considering a cluster of masses - do we include the interaction energies within them or not when talking about the mass of a cluster? It has recently been suggested that complex hierarchies of structure could produce large deviations from the expectations of Friedmann cosmology, essentially because the cumulative effect of gravitational interaction energies over many different spatial scales could contribute substantially to the total amount of mass in the universe [130]. We will consider this possibility in the context of our models of clustered black holes. The discussion of mass parameters and interaction energies that follows will proceed as in [167] and [168].

4.4.1 Mass Parameters

In order to proceed we first need to define our 3 types of mass - bare, proper and cluster. The definitions of each of these are given below.

Bare mass: The first mass parameter we wish to consider is the bare mass of each of our mass points, $\tilde{m}_i$. As in chapter 3, this parameter is introduced by

simple analogy with the terms that appear in a time-symmetric slice through the Schwarzschild solution, but does not necessarily correspond in any direct way to the physical mass that an observer near a black hole would infer for that object. In the case of time-symmetric initial data describing a cluster of black holes in an asymptotically flat space, it is known that the sum of the bare mass parameters corresponds to the sum total of individual proper masses of all the black holes, as well as the sum total of all gravitational interaction energies between each pair of black holes [166]. The interpretation in the present case is a little more complicated, but we still wish to use these parameters as our first measure of mass. Their meaning will be investigated further below.

Proper mass: The proper mass of each black hole is defined by rotating our coordinate system so that the black hole we are investigating is centered at $\chi = 0$, and by looking at the behaviour of the geometry in the limit $\chi \to 0$. By comparing the leading-order terms in the metric to the Schwarzschild geometry it is then possible to read off a value for the mass, which for a universe containing N black holes is given by Equation (3.15), which we will restate here,

$$m_i = \sum_{j \neq i}^{N} \frac{\sqrt{\tilde{m}_i \tilde{m}_j}}{\sin\left(\frac{\chi_{ij}}{2}\right)}, \tag{4.17}$$

where i is the label that gives the mass point under consideration, j labels all other masses, and χ_{ij} is the coordinate distance between points i and j. We will refer to m_i as the proper mass of the ith black hole, which technically corresponds to the mass that an observer in the asymptotically flat region on the far-side of the Einstein-Rosen bridge would infer by looking at how the gravitational field drops off at infinity. This gives a well-defined mass to each of the black holes, but again does not necessarily correspond to the mass that an observer in the cosmological region of the space would infer. It can be seen that the proper mass of a black hole is specified by the positions of all of the other $N - 1$ masses in the universe.

Cluster mass: The third mass parameter we wish to introduce is what we will refer to as the cluster mass, $\mathfrak{m}_i$, which will only be defined for black holes that are within a cluster. The idea here is to consider the proper mass that such a black hole would have if we include only contributions to Equation (4.17) that come from

masses outside of the cluster, so that

$$\mathfrak{m}_i = \sum_{j=1}^{N-C_n} \frac{\sqrt{\tilde{m}_i \tilde{m}_j}}{\sin\left(\frac{\chi_{ij}}{2}\right)}, \tag{4.18}$$

where again i labels the black hole under consideration, which we arrange to be at $\chi = 0$, but this time j labels the masses outside of the cluster. The N is again the total number of black holes in the universe, and C_n here corresponds to the number of masses in each cluster (which from our construction is equal to the number of vertices in the primitive lattice cell of the original n-mass lattice). We therefore have that $N = n\,C_n$, and the summation in Equation (4.18) can be seen to be over the $N - C_n$ black holes outside the cluster under consideration.

These definitions of mass will be used to investigate the role of interaction energies within our configurations as well as the FLRW comparisons.

4.4.2 Interaction Energies

Recall the known result that in Einstein's theory, gravitational interaction energies themselves can act as sources of mass, see Figure 4.10. We can write down an expression for the total gravitational mass of this system M_{tot} when viewed from infinity, which is given by [166]

$$M_{\text{tot}} = m_1 + m_2 - \frac{m_1 m_2}{r}. \tag{4.19}$$

In general, for many masses this generalises to

$$M_{\text{tot}} = M_{\text{obj}} + M_{\text{int}}, \tag{4.20}$$

where M_{obj} is the sum total mass of all of the individual objects in the system, and M_{int} is the sum total of all the pairwise interactions between objects in the system. Applying this formula to the black holes within a cluster, and the clusters within the cosmology, will allow us to determine values for the relevant gravitational interaction energies both within and between clusters of black holes.

Interaction energies within clusters: If we start by considering the individual black holes within a cluster, then we can derive an expression for the interaction energies between all objects within that cluster, $M_{\text{int}}^{\text{wcl}}$. This was calculated in [167],

and is given by

$$M_{\text{int}}^{\text{wcl}} \simeq -\sum_{i}^{C_n} \sum_{j\neq i}^{C_n-1} \frac{\sqrt{\tilde{m}_i \tilde{m}_j}}{\sin\left(\frac{\chi_{ij}}{2}\right)}, \tag{4.21}$$

where the sum over i is over all the C_n masses in the cluster, and the sum over j is over the remaining $C_n - 1$ masses in the cluster (for every ith black hole). Using this expression, we can write the sum of intra-cluster interaction energies $M_{\text{int}}^{\text{wcl}}$ in terms of the mass parameters in the previous section as

$$M_{\text{int}}^{\text{wcl}} = M_{\text{tot}}^{\text{cl}} - M_{\text{obj}}^{\text{bh}} \simeq \sum_{i}^{C_n} \mathfrak{m}_i - \sum_{i}^{C_n} m_i, \tag{4.22}$$

where in this case $M_{\text{obj}}^{\text{bh}}$ is the sum total of proper masses of the individual black holes in the cluster, and where $M_{\text{tot}}^{\text{cl}}$ is the total mass of the cluster (which can now be seen to be given by the sum of $\mathfrak{m}_i$ over all black holes within the cluster).

Separation interaction energies: Let us now consider the interaction energies between black holes separated by cosmological distances, and the total mass of the universe as a whole. These quantities are difficult to define, but a natural definition for the total energy in the cosmological model is given by

$$M_{\text{tot}}^{\text{cos}} = \sum_{i}^{N} \tilde{m}_i. \tag{4.23}$$

This quantity is defined in analogy to the standard expression for N black holes in an asymptotically flat space [166] and is closely related to the expression that one would obtain when considering the total mass of all black holes and interaction energies in one of the asymptotically flat flange regions on the far side of an Einstein-Rosen bridge [168]. Using it to evaluate the inter-cluster gravitational interaction energies, we find

$$M_{\text{int}}^{\text{sep}} = M_{\text{tot}}^{\text{cos}} - nM_{\text{obj}}^{\text{bh}} = \sum_{i}^{N} \tilde{m}_i - \sum_{i}^{N} m_i \tag{4.24}$$

where the term containing $M_{\text{obj}}^{\text{bh}}$ again indicates the total proper mass of all black holes, but this time includes all N black holes in the universe. This expression has an appealing similarity to the one given in Equation (4.22), and is intended to give a measure of the total of all gravitational interaction energies between all black holes.

Interaction energies between clusters: Using the results above, we can de-

duce an expression for the interaction energies between clusters that are separated by cosmological scales. Using Equation (4.20) we find this quantity to be equal to

$$M_{\text{int}}^{\text{bcl}} = M_{\text{tot}}^{\text{cos}} - nM_{\text{tot}}^{\text{cl}}, \tag{4.25}$$

where $M_{\text{tot}}^{\text{cos}}$ is again the total energy in the entire model, and $M_{\text{tot}}^{\text{cl}}$ here is the total energy within each cluster (i.e. proper masses of the black holes plus intra-cluster interaction energies). From our previous considerations this can be written as

$$M_{\text{int}}^{\text{bcl}} \simeq \sum_{i}^{N} \tilde{m}_i - n \sum_{i}^{C_n} \mathfrak{m}_i = \sum_{i}^{N} \tilde{m}_i - \sum_{i}^{N} \mathfrak{m}_i \tag{4.26}$$

where n is the number of clusters (equal to the number of masses in the original lattice) and where in the last equality we have used the fact that all clusters are identical. This expression is intended to describe the sum total of all gravitational interaction energies between all clusters of black holes. Again, it has a pleasing similarity with Equations (4.22) and (4.24).

With these definitions, we can now calculate the different types of interaction energies within our 4 configurations. For simplicity, in each model we choose the mass parameters to all be identical. Figure 4.11 depicts our results for each of the 4 models where we calculate the total separation interaction energy (blue lines), the interaction energies within n clusters (orange lines) and the interaction energy between clusters (green lines), as a function of splitting up parameter λ.

When the black holes are clustered there will be interactions between the C_n black holes within each cluster, as well as interactions between the clusters. These two interaction energies are depicted as the orange and green lines, respectively. Their sum is the total of all interaction energies between all black holes in the model and is given by the blue line. It is clear from the figure that the intra-cluster interaction energies diverge as $\lambda \to 0$, in the limit that the black holes get closer together. The total interaction energy between all separated black holes also diverges, but the inter-cluster interactions defined in Equation (4.26) can be seen to remain finite and close to constant. This is exactly what we would expect from these quantities, and gives some a posteriori justification for their introduction.

The four plots in Figure 4.11 are sufficient to give information about all of the interaction energies in all of our clustered-mass models. For example, this is because the models that contain masses clustered around the positions of the cell centres of the original 8-mass lattice are given by the $\lambda < 1/2$ portion of plot (b), while

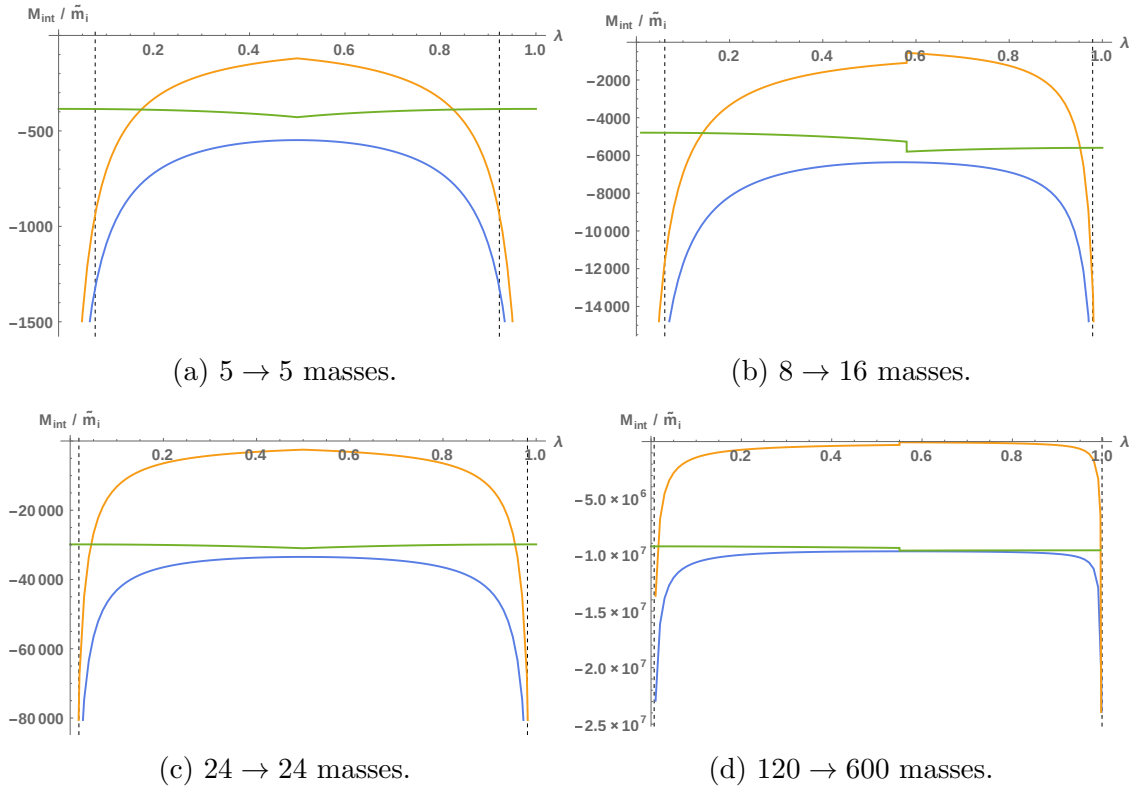

(a) $5 \to 5$ masses.

(b) $8 \to 16$ masses.

(c) $24 \to 24$ masses.

(d) $120 \to 600$ masses.

Figure 4.11: All three interaction energies for each of the configurations as a function of λ, and in units of mass parameter $\tilde{m}_i$. The blue lines correspond to the total separation interaction energy, $M_{\text{int}}^{\text{sep}}$, the orange lines give the interaction energies within n clusters, $M_{\text{int}}^{\text{wcl}}$ and the green lines give the interaction energy between clusters, $M_{\text{int}}^{\text{bcl}}$.

models with masses clustered around the positions of the cell centres of the original 16-mass lattice are given by the $\lambda > 1/2$ portion of the same plot. This is due to these two lattices being dual to each other, with the 8-mass model recovered in the limit $\lambda \to 0$ and the 16-mass model recovered in the limit $\lambda \to 1$. Similarly, plot (d) is sufficient to describe black holes clustered around the positions of the cell centres in the original 120 and 600-mass models. In the case of plots (a) and (c) only clustered masses around one type of lattice cell centres are considered, because the 5 and 24-mass lattices are both self-dual.

The critical values of λ, λ_{crit}, are denoted in each of these plots by the vertical dashed lines. Recall that these values of λ denote when the clustered masses become distinguishable as individual black holes to observers in the cosmological region. The reader may note that the halfway point between original setups occurs at $\lambda = 0.5$ only for the models that are self-dual, whilst the non-self dual models have an asymmetry in transitioning from one to another. For the 8 to 16-mass case, the halfway point

(when individual black holes are maximally separated) is instead at $\lambda = 0.576$,whilst for the 120 to 600 masses this point occurs at $\lambda = 0.553$. This phenomenon can be seen as the slight discrepancies in the green and orange curves in plots (b) and (d) - they are due to changing whether we consider the black holes to be clustered around the centres of the lattice cells or the dual lattice cells. Of course, for values of $\lambda \sim 1/2$, these masses should not really be considered as being clustered around either point, so this discrepancy has no real practical significance, but is explained for completeness.

The reason for introducing and studying these different interaction energies will become clear in the next section, when we compare our clustered-mass models to Friedmann solutions and to each other. In order to do this quantitatively, we need to know which (if any) of the interaction energies should be included in the total mass content of our black hole universes.

4.5 Comparison with FLRW Cosmology

4.5.1 Choosing a Comparison Cosmology

We will now compare our lattice models to their corresponding FLRW counterparts and calculate the effect clustering has between the two types of cosmology. We choose the FLRW cosmologies to be composed of pressureless dust and have a spatial curvature constant given by $k = 1$, meaning they are also positively curved. We also choose the FLRW models to contain the same total proper mass as their lattice counterparts, as in chapter 3.

The quantity we will be comparing is the same quantity as before, the measure of global scale, or scale factor. For the FLRW cosmology this was given by Equation (3.16) and for the lattice cosmology this was given by $ds^2 = \psi^4 d\tilde{s}^2$. Recall that in chapter 3, definition D2 was the length of the edge of a cell. For our structuration process, this is no longer viable as this measures a length between two vertices of a cell. Our black holes are on trajectories towards these points and so by construction, at $\lambda = 1$, this quantity would diverge. Therefore we are constrained to use definition D1 instead, and the reader should note that this will give sufficient results.

As Equation (3.17) is a function of position, there is a degree of ambiguity as to where we calculate this for each of the models. In order to make this choice as unambiguous as possible (as well as to minimise the effect of any individual nearby black hole), we choose the point that is furthest away from all masses, where ψ is at its global minimum. The resulting scale factor is then uniquely specified for any

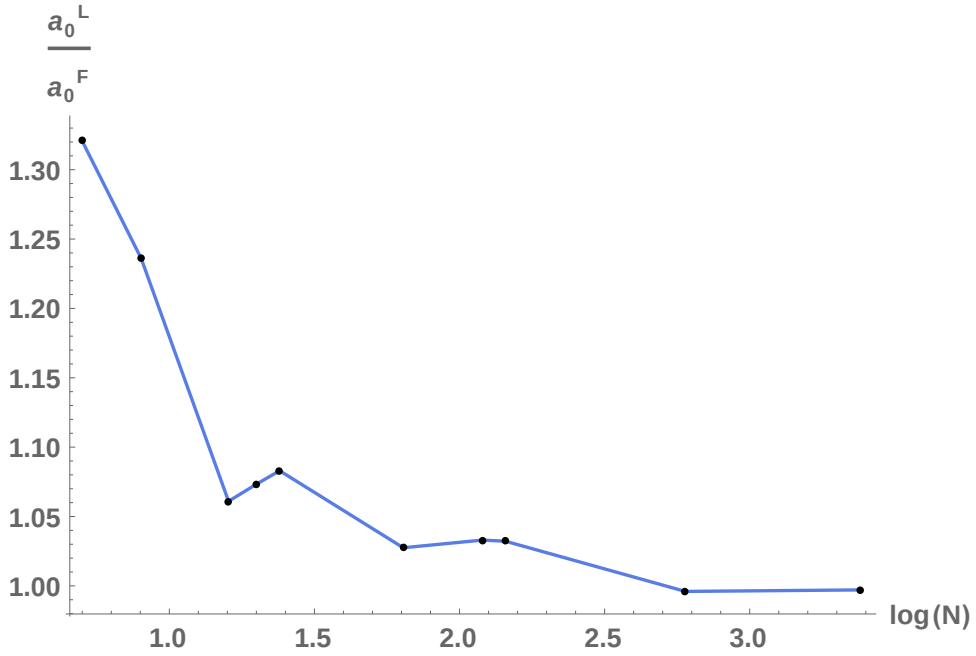

Figure 4.12: The ratio of scale factors in the lattice universes a_0^L and the dust-dominated positively-curved FLRW universes a_0^F, as a function of the number of masses in the universe N, where $N = 5$, 8, 16, 20, 24, 64, 120, 144, 600 and 2400, from left to right.

value of $\lambda \in [0, 1]$.

4.5.2 At a Fixed Value of λ

Firstly, we compare the 4 configurations each at a fixed value of λ, specifically $\lambda = 0.5$. This means we are considering the lattices when the masses are nearly equidistant from each other but not exactly. We can then add this to our existing catalogue of the 6 original lattices, to have a total of 10 different lattices, with masses ranging from 5 to 2400 in number, and see the effect this has. We plot these results in Figure 4.12, which clearly show that increasing the number of masses has a global trend of decreasing the size of the lattices universes to be increasingly similar to the FLRW cosmologies, if not always locally (these smaller variations are due to different polyhedra being used).

4.5.3 At Different Values of λ

Secondly, we now compare the 4 configurations to their FLRW counterparts, but at different values of λ, to measure the effect of clustering. Recall that if λ is within the critical value λ_{crit} then the number of black holes in the cosmological region is

given by the number of cells in the original lattice model, n. If this is the case it is most appropriate to use Equation (4.18) to determine the proper mass of the cluster within the shared horizon, so that $M = \sum_i \mathfrak{m}_i$. This measure includes the interaction energies of the black holes within the shared horizon, which are now indistinguishable from the perspective of a cosmological observer. In this case, we then compare the lattice models to an FLRW universe with the same total mass as the sum of all of these cluster masses.

If λ is beyond the critical value, however, then there are $N = n\,C_n$ distinct black holes in the cosmological region, where C_n is the number of masses in a cluster. In this case we could choose to calculate the total mass of each cluster of black holes using $M = \sum_i \mathfrak{m}_i$ or use $M = \sum_i m_i$ where m_i is the proper mass of each black hole. The former of these methods will include the intra-cluster interaction energies, while the latter will not. We display the results for both methods in Figure 4.13, for each of our lattice models.

The results of using this method show the expected behaviour for the limiting cases when $\lambda \to 0$ or 1, as determined in [3]. The results for values of λ near to these extreme cases also appear well behaved, as expected due to the fact that we are still considering an effective n-mass model (the extra masses are behind a shared horizon), with the cluster mass $\mathfrak{m}_i$ being used as the measure of mass rather than the individual proper masses m_i.

If we now consider the values of λ beyond the critical values, then we can see from Figure 4.13 that the comparisons made using proper masses of the black holes (solid lines) can yield quite different results from those made using the cluster mass (dotted lines). If we take the total mass of the black hole universes to be given by the sum total of individual proper masses of all black holes within it, as has frequently been done in previous studies, then the results can be seen to vary strongly with changing λ. In the most extreme case, which is the 600-mass model, the scale factor of the lattice universe drops down to 30% of its FLRW counterpart when the black holes are made to cluster (i.e. when the masses are close together, but still separated enough to be considered individual black holes). However, when the ratio of scale factors are determined using the total cluster masses of the black hole (which include the interaction energies within each cluster), it can be seen that the dependence of the scale factor a_0^L on λ is much less pronounced. In Figure 4.13, the dotted lines that give the ratio of scale factors in this case have been truncated artificially, as at some point it becomes meaningless to consider black holes separated by large distances as belonging to a cluster.

The situations immediately before and after the critical values of λ do not produce

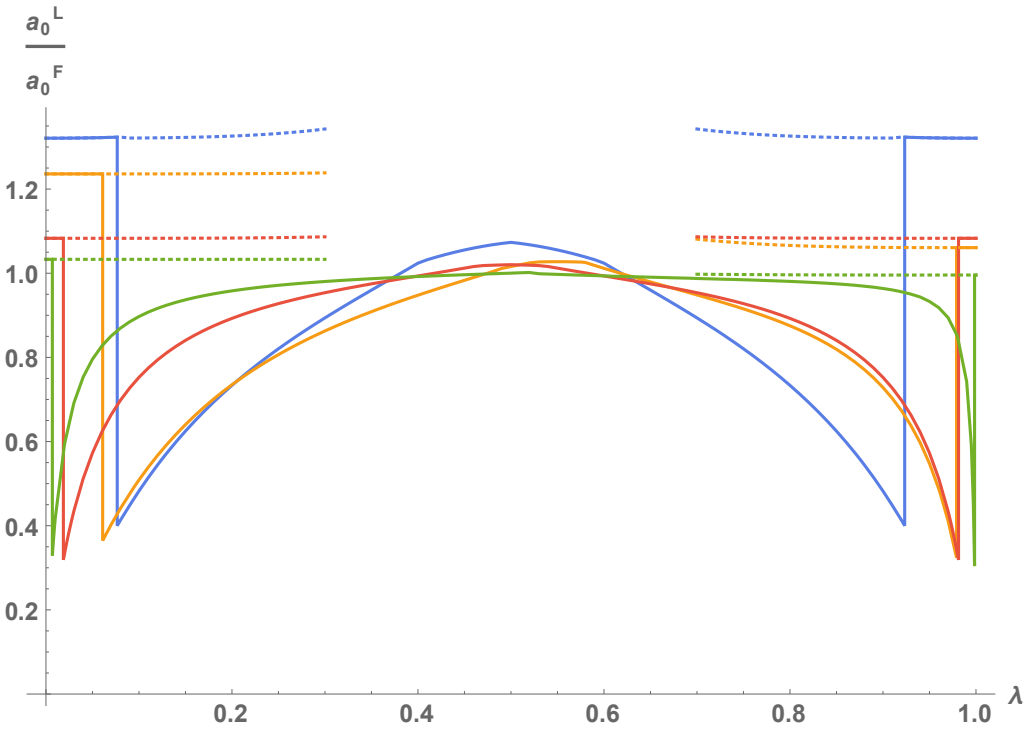

Figure 4.13: The ratio of scales between the lattice universes a_0^L and the corresponding dust-dominated positively-curved FLRW universes a_0^F, as a function of λ. The four curves correspond to the models with the following number of masses: $5 \to 5$ (blue), $8 \to 16$ (yellow), $24 \to 24$ (red), and $120 \to 600$ (green). The sudden drops appear at the points where $\lambda = \lambda_{\text{crit}}$, which have different values for each of the different cases. In the regions where λ is beyond λ_{crit}, the dotted lines correspond to the total mass being calculated using the sum of cluster masses ($\sum_i \mathfrak{m}_i$) and the solid lines correspond to the total mass being calculated using the sum of proper masses of individual black holes ($\sum_i m_i$).

discontinuous changes in the geometry of the cosmological region when we pass λ_{crit}, only an instantaneous change in the existence of the shared horizon. This suggests that the appropriate measure of total mass should include the interaction energies that exist within a cluster, even when the shared horizon does not exist. This raises some interesting questions about dynamical structure formation in the real Universe: if interaction energies contribute to the energy budget of the Universe, then which interactions between which pairs of objects should be considered? In the examples considered in this section we have artificially introduced clusters of objects on a single scale. In the real Universe structure exists on a multitude of scales and pairwise interactions could in principle be expected to exist between every pair of objects in the Universe. Should we take each of these interactions into account? And, if not, where should we draw the line?

4.5.4 Comparison Between Lattice Models

In the previous section we compared our clustered lattice models to FLRW models with the same total proper mass, and the same total cluster mass. These results can be used to work out the difference in scale between lattice models with different values of λ when they have the same $\sum_i m_i$ or $\sum_i \mathfrak{m}_i$. However, if we want to perform a similar analysis for lattice models with some fixed total bare mass $\sum_i \tilde{m}_i$ then a comparison with FLRW is less instructive. This is because there is a large difference between lattice models with some $\sum_i \tilde{m}_i$ and FLRW models that contain the same total bare mass in dust [3, 168]. Instead we can compare lattice models that have the same total bare mass but different values of λ. This allows us to see the consequences of structure formation on the large-scale cosmology if the total energy in the universe, including all proper masses and interaction energies, is kept fixed. The results are shown in Figure 4.14. We have chosen to normalise the scale factor by choosing bare mass parameters such that when $\lambda = 0$ we have $a_0^L = 1$. Beyond this value, we find that the scale factor increases with λ. This growth is initially rather slow, but rapidly increases as λ gets larger. Note that as the overall number of masses increases, the increase in the scale factor at large values of λ becomes less pronounced. For example in the 5-mass lattice the scale factor is approximately 1.05 at $\lambda = 0.3$, but for the 600-mass lattice it is only 1.003. This suggests that the effect of clustering decreases as the number of masses in the universe is increased, if we compare models with the same total energy, and drops below 1% when the number of black holes is $> 10^3$. This is qualitatively similar behaviour to the results shown in Figure 4.13, when the sum of intra-cluster interaction energies and proper masses were taken into account. It shows that the consequences of inter-cluster interactions are not particularly strongly affected by the clustering, which is in keeping with the near-constant nature of the green lines in Figure 4.11.

4.6 Discussion

We extended the 6 original black hole lattices by devising a novel formalism to create structures within them, by splitting up the existing masses and moving them along very specific trajectories. The purpose of this was to investigate the consequences of the existence of astrophysical structure on the large-scale properties of the universe. This gave us a set of four new black hole universes, containing 20, 64, 144 and 2400 masses, and with each model being controlled by a single parameter λ. We found that a collective horizon appeared around the clustered black holes when they

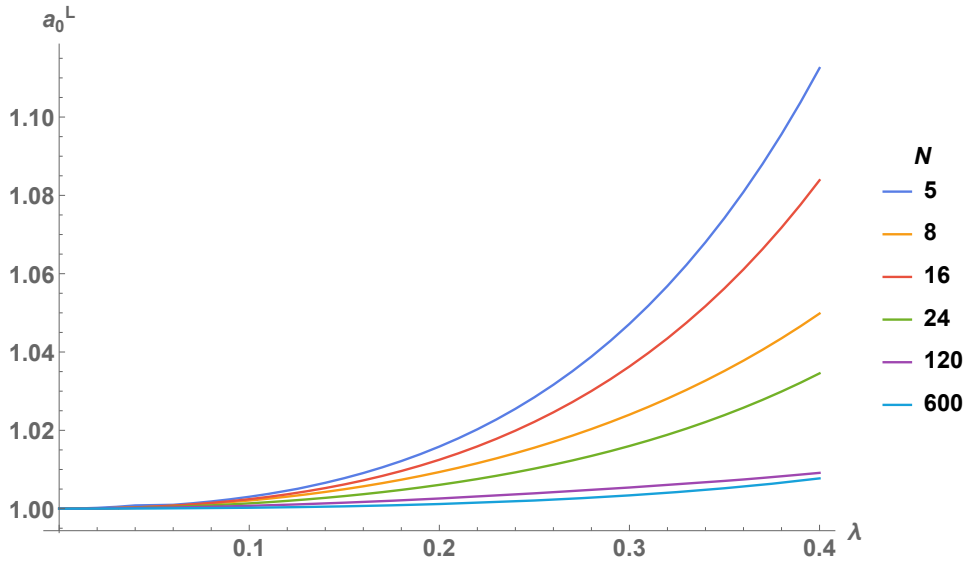

Figure 4.14: The scale factor of lattice cosmologies a_0^L as a function of λ when the total energy is kept fixed (such that $\sum_i \tilde{m}_i$ = constant). The values of the $\tilde{m}_i$ have been chosen for each of the 6 different lattices so that $a_0^L = 1$ when $\lambda = 0$, and are different for each model.

were sufficiently close together. We derived expressions for the interaction energies between clusters and within clusters, as well as the proper mass of individual black holes and the mass of clusters of black holes. When comparing our lattices to their FLRW counterparts we found that the most sensible way to do this was to include the intra-cluster interaction energies in the total energy budget, along with the proper masses of each of the black holes. Failure to include the interaction energies within clusters would appear to give deficits of order unity, if only the sum of proper masses of individual black holes were taken into account. The interaction energies within astrophysical structures therefore seem capable of having a non-negligible influence on the scale of the global cosmology. Therefore it appears we need to take interaction energies into account when calculating the total energy in our cosmological models. These results are a first step towards understanding the effects of structure formation on the global cosmology in exact solutions with clustered discrete masses. If the total energy in the universe is found to remain approximately constant, then we predict the effects of structure formation to be modest ($\sim 10\%$ when $N \sim 10$, decreasing to $\sim 1\%$ when $N \sim 10^3$). However, if only the proper mass of black holes remains constant then deviations of the order of $\sim 10\%$ seem possible even when the number of masses is very large.

The work presented so far has involved extending the initial data in chapter 3 to include masses in more complex configurations, but is still based on the Schwarzschild

solution to the Einstein field equations. We can further extend this by considering other solutions, such as Reissner-Nordström or Schwarzschild-de Sitter, or even other gravitational theories, such as scalar-tensor. Thus, provided we can find exact solutions to a set of constraint equations, we can construct a variety of these inhomogeneous cosmologies. This is exactly what we will do in the remaining chapters, where we move on from the linearly superposed Schwarzschild masses as our initial data.

5 Solutions with a Cosmological Constant Λ

This chapter is based on [36].

5.1 Introduction

In this chapter and the following ones we move on from considering only the Schwarzschild solution and instead look at other solutions to the Einstein field equations. This chapter focuses on utilising the Schwarzschild-de Sitter spacetime, which means we will be considering cosmological models that not only contain the usual black holes as before, but also a cosmological constant denoted by Λ. As with the previous chapter, we are extending the existing black hole lattices such that they are being generalised, and in the limit of vanishing Λ, the new models reduce to the original ones in [3]. As well as providing new mathematical insights into inhomogeneous cosmologies when these generalisations are performed, there is an overriding motivation particularly for including a cosmological constant. There is ample evidence to support the idea that our own Universe is undergoing a late time accelerated expansion [22, 23], of which a positive cosmological constant is a satisfactory candidate. Therefore the inclusion of Λ allows a more 'realistic' cosmological model, and one that can be compared to existing expanding models. The post-Newtonian models in [142] have already been extended to include a cosmological constant, [143], whilst the authors in [169] have considered a numerical construction of a flat, infinite cubic lattice. Our work differs from these previous studies as we make no approximations when modelling the geometry of space, and because we solve the constraint equations using a fully analytic approach. The topology of our model is also different to that of Yoo et al., which allows us the benefit of studying six different tessellations (rather than the one tessellation that exists in flat space).

The rest of this chapter is organised as follows. In section 5.2 we derive initial data for our models. In section 5.3 we review the Schwarzschild-de Sitter solution

and determine the masses of the black holes and in section 5.4 we derive a formula for locating apparent horizons within each of our lattice models. This is then used to determine what values of Λ give cosmologically viable solutions in section 5.5. One of the ways our models can be compared to equivalent FLRW models is by looking at how backreaction affects the deceleration parameter, which we do in section 5.6. Finally we briefly look at how our initial data could be evolved numerically in section 5.7 before discussing our findings in section 5.8.

5.2 Initial Data with Λ

The relevant Hamiltonian and momentum constraint equations that we will need are as follows,

$$\mathcal{R} + K^2 - K_{ij}K^{ij} = 16\pi\rho, \tag{5.1}$$

$$D_j\left(K_i^j - h_i^j K\right) = 0, \tag{5.2}$$

where $\mathcal{R}$ is the Ricci scalar of the hypersurface, K_{ij} is the extrinsic curvature, K its trace, ρ is the total energy density as measured by an observer n^i, h_{ij} is the intrinsic metric of the hypersurface and D_j is the covariant derivative with respect to this metric. In order to solve these, we perform a further conformal-transverse-traceless decomposition, as introduced in chapter 2. Recall that the extrinsic curvature can be written in terms of its trace K and trace-free part A_{ij} as in Equation (2.55), and that we can also perform a conformal rescaling of the 3-metric, where $h_{ij} = \psi^4\tilde{h}_{ij}$. This then gives an identity for the Ricci scalar as before, see Equation (2.49). Substituting these results into the constraint equations above gives

$$8\tilde{D}^2\psi - \psi\tilde{\mathcal{R}} - \frac{2}{3}\psi^5 K^2 + \psi^5 A_{ij}A^{ij} = -2\Lambda\psi^5 \tag{5.3}$$

$$D_j\left(A_i^j - \frac{2}{3}h_i^j K\right) = 0, \tag{5.4}$$

where the substitution $8\pi\rho = \Lambda$ has been made. Previously in [3], both the extrinsic curvature and cosmological constant were zero. For non-vanishing extrinsic curvature and/or Λ we have that Equation (5.3) is non-linear in ψ, making it extremely difficult to solve in general. However, if we choose

$$K^2 = 3\Lambda \quad \text{and} \quad A_{ij} = 0, \tag{5.5}$$

then Equation (5.4) is satisfied identically and Equation (5.3) becomes linear in ψ,

$$8\tilde{D}^2\psi = \psi\tilde{\mathcal{R}}. \tag{5.6}$$

It is manifest that this is just the Helmholtz equation from previous chapters, therefore we can choose the conformal metric of the initial hypersurface to be a 3-sphere of constant curvature as before, and the conformal factor will take the same form as in Equation (3.4).

5.3 Proper Masses

We can now compare the geometry of our chosen initial data in the previous section to an appropriate slice through the Schwarzschild-de Sitter solution to obtain an expression for the proper mass. The Schwarzschild-de Sitter solution in standard Schwarzschild coordinates (t, r, θ, ϕ) is given by

$$ds^2 = -\left(1 - \frac{2M}{r} - \frac{\Lambda r^2}{3}\right)dt^2 + \frac{dr^2}{\left(1 - \frac{2M}{r} - \frac{\Lambda r^2}{3}\right)} + r^2\left(d\theta^2 + \sin^2\theta d\phi^2\right), \tag{5.7}$$

where M is the mass of the black hole. This solution has both black hole and cosmological horizons provided that the combination of parameters $M^2\Lambda$ lies within the range $0 < M^2\Lambda < 1/9$. As this is a requirement of our models, this will be investigated later in this chapter.

Previous chapters have involved initial data with zero extrinsic curvature. Equation (5.5) shows that the trace of the extrinsic curvature we are now considering is constant and therefore we need to look for constant mean curvature (CMC) slices of the above Schwarzschild-de Sitter solution. In order to proceed, we first write the solution in the following form [170],

$$ds^2 = -\left(\alpha^2 - \frac{\beta^2}{\psi}\right)d\tilde{t}^2 + 2\beta d\tilde{t}dr + \psi dr^2 + r^2\left(d\theta^2 + \sin^2\theta d\phi^2\right), \tag{5.8}$$

where α and β are the lapse and shift respectively and where $\psi = \psi(r, \tilde{t})$, (note that this is not necessarily the conformal factor). Computing the 3-dimensional Christoffel symbols and non-vanishing components of the Ricci tensor allows the Ricci scalar of the three-space to be written as [1]

$$\mathcal{R} = 2\partial_r\psi/\left(r\psi^2\right) + 2(1 - 1/\psi)/r^2, \tag{5.9}$$

which gives the Hamiltonian constraint Equation (5.1) as [171]

$$\frac{2}{r}\left(\partial_r\psi^{-1}+\frac{1}{r}\psi^{-1}-\frac{1}{r}\right)+K_i{}^jK_j{}^i-\frac{1}{3}K^2=0. \tag{5.10}$$

Using $\beta=\beta_r=A\beta^r$ and the evolution equation for the spatial part of the metric, Equation (2.45), yields $K_\theta{}^\theta=K_\phi{}^\phi=-\frac{1}{2}\left(K_r{}^r-K\right)$, and therefore the momentum constraint (5.2) as

$$\partial_r\left(r^3K_r{}^r\right)-\frac{1}{r}K=0. \tag{5.11}$$

Integrating this and Equation (5.10) yields the extrinsic curvature as

$$K_r{}^r=-\sqrt{\frac{2}{3}}|A|+\frac{1}{3}K, \tag{5.12}$$

and the conformal factor ψ as [171]

$$\psi^{-1}=1-\frac{2M}{r}+\left(\sqrt{\frac{2}{3}}K+\frac{|A|}{2}\right)\frac{|A|}{3}r^2, \tag{5.13}$$

where $|A|=\sqrt{A_{ij}A^{ij}}$ and where M is the mass parameter from Equation (5.7). The value of $|A|r^3$ in this expression is constrained to be a function of $\tilde{t}$ only, and must obey the following evolution equation

$$\frac{d\left(|A|r^3\right)}{d\tilde{t}}=\sqrt{6}\alpha M-\frac{\sqrt{6}r^2}{\psi}\frac{\partial\alpha}{\partial r}+\left(\frac{2|A|}{\sqrt{6}}-\frac{K}{3}\right)\alpha|A|r^3. \tag{5.14}$$

For further details about this foliation, including explicit forms for the shift and lapse functions, the reader is referred to [171]. The particular leaf we require is the one on which $A_{ij}=0$. From Equation (5.13), this gives us a hypersurface with intrinsic geometry

$$ds^2=\left(1+\frac{M}{2\rho}\right)^4\left(d\rho^2+\rho^2\left(d\theta^2+\sin^2\theta d\phi^2\right)\right), \tag{5.15}$$

where we have transformed to an isotropic radial coordinate using $r=\rho(1+M/2\rho)^2$. This is manifestly the same intrinsic geometry as a time-symmetric slice though the Schwarzschild geometry. Given that the intrinsic geometry in our initial data is also identical to that of a time-symmetric slice through the Schwarschild solution, this means that the proper mass of the ith black hole must also be given by Equation (3.15).

5.4 Apparent Horizons

Just as we did in section 4.3, we will look to the orthonormal constraint equations and the results already derived in chapter 2 to locate the apparent horizons. Recall a constraint equation given by the Bianchi identity was given in Equation (2.72). For vanishing Λ, the expansion of the spacelike normal vector, denoted a_1 was zero also. Now however this is not the case and we can relate it to the expansion scalar by using Equation (2.74). We have that

$$a_1^{\text{outer}} = -\frac{1}{2}m^{\mu\nu}\nabla_\mu e_{1\,\nu} = \frac{1}{3}\Theta = \pm\sqrt{\frac{\Lambda}{3}}, \tag{5.16}$$

where we have used the fact that $\Theta = -K$ and $K^2 = 3\Lambda$. The $\pm$ after the final equality indicates the fact that our initial data can describe either an expanding $(+)$ or a collapsing $(-)$ space. The superscript 'outer' here refers to the fact that we are considering outer trapped surfaces, recall Equation (2.68). We can also consider ingoing future-directed null geodesics, l^μ. These are defined as $l^\mu = \frac{1}{\sqrt{2}}(n^\mu - s^\mu)$. The vanishing expansion of ingoing null geodesics gives rise to marginally inner trapped surfaces, and therefore our relation between the expansion of e_1^μ and the expansion scalar differs only by a minus sign. We can immediately write

$$a_1^{\text{inner}} = -\frac{1}{2}m^{\mu\nu}\nabla_\mu e_{1\,\nu} = -\frac{1}{3}\Theta = \mp\sqrt{\frac{\Lambda}{3}}, \tag{5.17}$$

where the $\pm$ sign here corresponds to expanding $(-)$ or collapsing $(+)$ space. We therefore have both inner and outer trapped surfaces for each of the two possible signs of Θ. Those with $\Theta < 0$ (or $K > 0$) correspond to contracting universes whilst those with $\Theta > 0$ (or $K < 0$) correspond to expanding universes.

Finally, in Equation (2.72) we can again choose coordinates such that $E_3{}^3 = E_2{}^2 = 0$. Combining all of the results we now have an expression to locate the positions of the apparent horizons in our lattices with a cosmological constant, which is given by

$$\mathbf{e}_1\left(E^{11}\right) = \alpha_1\alpha_2\sqrt{3\Lambda}E^{11} \tag{5.18}$$

where we have introduced two new quantities, α_1 and α_2, which both take values of either $+1$ or -1. The first parameter describes whether the space is expanding or contracting, and we choose $\alpha_1 = +1$ to correspond to expansion and $\alpha_1 = -1$ to correspond to contraction. The second parameter then describes whether the horizon in question is an inner or outer trapped surface. Given our previous choice,

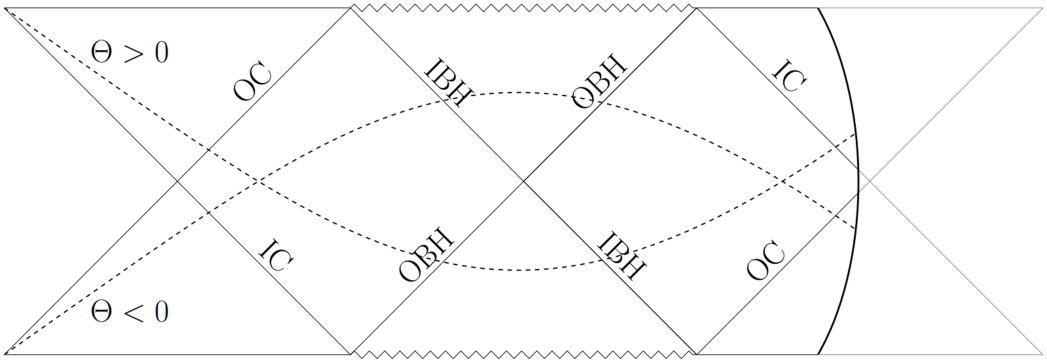

Figure 5.1: Penrose-Carter diagram for the region of spacetime in a lattice with non-zero Λ. The hypersurfaces that constitute the initial data are shown as dashed lines. The expanding universe with $\Theta > 0$ passes through an outer trapped cosmological horizon (OC), an outer trapped black hole horizon (OBH), an inner trapped black hole horizon (IBH) and an inner trapped cosmological horizon (IC) before emerging into the cosmological region on the right. Similarly, a contracting universe with $\Theta < 0$ passes through an inner trapped cosmological horizon (IC), an inner trapped black hole horizon (IBH), an outer trapped black hole horizon (OBH) and an outer trapped cosmological horizon (OC) before emerging into the cosmology. The solid curved line on the right-hand side represents a cut-off where beyond this the causal structure of the cosmological region should be expected to be too complicated to represent in a 2D figure.

we have that $\alpha_2 = +1$ corresponds to outer trapped surfaces whilst $\alpha_2 = -1$ refers to inner trapped surfaces. The reader may note that this implies there is a symmetry between outer trapped surfaces in the expanding case and inner trapped surfaces in the contracting case. Consequently, a naive estimate of the total number of horizon types to be found would a priori have been 8 (cosmological and black hole, which can be either inner or outer trapped, occurring in either expanding or contracting configurations). However, our analysis above shows that the degeneracy between outer + expanding and inner + contracting reduces the total number of different horizons to be just 4, which will be calculated in the next section. Finally, in the limit $\Lambda = 0$ we note that the expression used to locate the apparent horizons given in Equation (5.18) reduces to that of Equation (4.16) as expected.

We summarise our analyses of the hypersurfaces of our lattices with Λ by showing a Penrose-Carter diagram for some arbitrary value of Λ in Figure 5.1. Both expanding and contracting hypersurfaces have been considered and are indicated by the sign of Θ. On the left of the diagram the spacetime approaches perfect Schwarzschild-de Sitter, while on the right it approaches the complicated cosmological region (separated off

by the curve). In between, each surface passes through exactly two cosmological horizons and two black hole horizons, which can be either inner or outer trapped surfaces. At the mid-point (within the black hole region) each of the two spaces contains a throat that has a finite, non-zero, minimal radius. In the limit $\Lambda \to 0$ we can verify that Equation (5.18) reduces to the corresponding Equation (4.16), and in that case the apparent horizon becomes degenerate with the minimal sphere that can fit within the throat at the centre of the black hole region. Finally, we note that the procedure outlined in this section correctly identifies the known locations of the horizons in the exact Schwarzschild-de Sitter geometry.

5.4.1 Locations of Apparent Horizons

We now seek to determine the location of these horizons in each of the six possible lattices. To start with we use the 5-mass model as an example and rotate coordinates so that one of the masses appears at the position $\chi = 0$. We then calculate the electric part of the Weyl tensor along a curve that connects this mass with one of its neighbours in an adjacent cell, as a function of radial coordinate χ. This information can then be used in Equation (5.18) to obtain the positions of the various horizons for different values of Λ in units of M_0^{-2} (where M_0 is the proper mass of one of the black holes). The results of this are displayed in Table 5.1, where we have chosen to consider an expanding universe ($\Theta > 0$) and therefore $\alpha_1 = +1$. In our subsequent analyses we consider horizons in the expanding case only unless specified otherwise. Of course the results and analyses for contracting solutions are exactly the same, albeit under an interchange of the words inner and outer when referring to horizons.

For $\Lambda = 0$, we find that the locations of the horizons at $\chi = \chi_2$ and $\chi = \chi_3$ are degenerate, as previously identified in [82]. The positions of the other two horizons when $\Lambda = 0$ are found to be at $\chi_1 = 0$ (the origin) and $\chi_4 = \frac{1}{2}\arccos(-\frac{1}{4})$, (the midpoint between masses). These are mathematical solutions to Equation (5.18), but for vanishing Λ had not previously been considered as physically interesting. Although the latter can rightly be identified as an extremal surface in the geometry (it is part of the face of one of the cells in the lattice), it is not part of a closed extremal surface, and so is not technically a horizon. Similarly, it is a stretch to call the sphere at $\chi_1 = 0$ a horizon, as this corresponds to a sphere at infinity on the far side of the Einstein-Rosen bridge. Nevertheless, it is useful to identify these points as cosmological horizons as they become more interesting when $\Lambda \neq 0$.

Switching on Λ reveals that the horizons change positions, as indicated in Table 5.1. For the inner trapped surfaces with $\alpha_2 = -1$, the black hole horizon at χ_3 moves

	$\alpha_2 = +1$		$\alpha_2 = -1$	
Λ/M_0^{-2}	χ_1	χ_2	χ_3	χ_4
0	0	0.413	0.413	0.912
0.002	0.00539	0.367	0.474	0.824
0.004	0.00781	0.349	0.507	0.781
0.006	0.00975	0.337	0.541	0.740
0.008	0.0115	0.326	0.586	0.690
0.009	0.0121	0.323	0.638	0.638
0.020	0.0196	0.285	-	-
0.040	0.0311	0.241	-	-
0.060	0.0426	0.207	-	-
0.080	0.0559	0.177	-	-
0.100	0.0749	0.144	-	-
0.111	0.104	0.104	-	-
0.120	-	-	-	-

Table 5.1: Positions of the horizons for the expanding 5-mass model, as a function of Λ measured in units of M_0^{-2}. The horizons at χ_1 and χ_2 are both outer trapped, while those at χ_3 and χ_4 are both inner trapped. Dashes indicate that no horizons exist for the given value of Λ. The position of the midpoint between masses is at $\chi = 0.912$ in this configuration.

outwards with increasing Λ, while the cosmological horizon at χ_4 moves inwards as Λ increases. This means that as Λ increases, χ_3 and χ_4 converge towards each other and become degenerate at $\Lambda \simeq 0.009 M_0^{-2}$. For values of Λ above this critical value, there are no solutions to Equation (5.18). Similarly, for outer trapped surfaces with $\alpha_2 = +1$, the black hole horizon at χ_2 moves to lower χ as Λ increases, whilst the cosmological horizon at χ_1 moves to higher values of χ. This corresponds to the black hole horizon moving outwards on the far side of the Einstein-Rosen bridge, while the cosmological horizon moves inwards from infinity. Again, these two horizons become degenerate at a critical value of $\Lambda \simeq 0.111 M_0^{-2}$ and there exist no solutions to Equation (5.18) for higher values of Λ.

To illustrate this behaviour graphically one can consider the functional form of the left and right-hand sides of Equation (5.18). These quantities are shown in Figure 5.2 as a function of the coordinate χ for the 5-mass expanding model with $\alpha_2 = \pm 1$. The coloured lines represent the right-hand side of Equation (5.18) and hence are

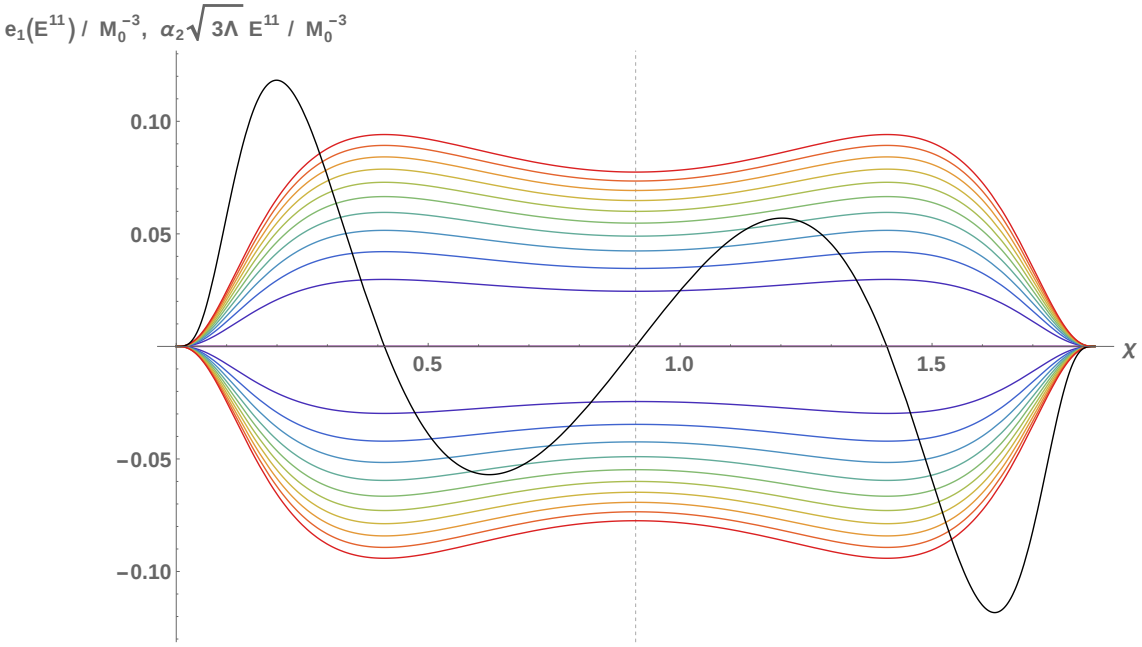

Figure 5.2: A graphical representation of the left and right-hand sides of Equation (5.18) for the expanding 5-mass model. The black curve corresponds to the left-hand side, while the multi-coloured curves correspond to the right-hand side. The values of Λ range from 0 (purple) to $0.02\,M_0^{-2}$ (red) in increments of $0.002\,M_0^{-2}$. For $\alpha_2 = +1$ the multi-coloured lines are above the horizontal axis, and $\alpha_2 = -1$ for those below. The vertical dashed line shows the midpoint between the two masses.

a function of Λ. When the black line and the coloured lines cross, the equation is satisfied and a value for the position of a horizon χ_h can be read off. For small enough values of Λ there are four occasions where this happens. However, if the value of Λ is increased sufficiently then these lines do not cross at all, and the horizons cease to exist, a point already illustrated in Table 5.1.

The χ values from the positions of the horizons can be plotted separately, and in the first panel of Figure 5.3 these values are shown for the 5-mass model. The subsequent panels show the positions of the horizons for each of the five other lattice universes that we are considering for different values of Λ. These diagrams show all four possible horizons, both inner and outer black hole horizons as well as inner and outer cosmological horizons. The extremal values of Λ in both the inner and outer regions are displayed in the diagrams as vertical lines. As the number of masses is increased the two extremal values for Λ converge until they become indistinguishable by eye as shown in the case of the 120-mass and 600-mass configurations. The black hole horizons meet at $\Lambda = 0$ as expected [82], and in every case the largest χ_4 value is simply the midway point between the two masses. The information presented in

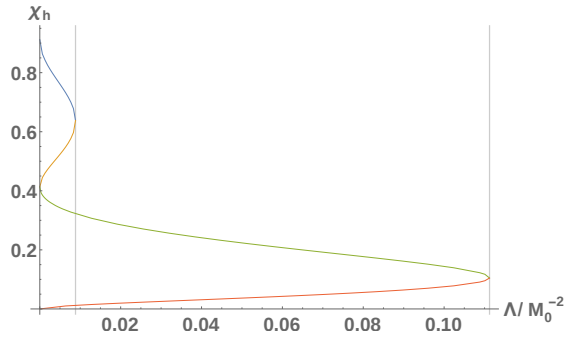

(a) 5 masses.

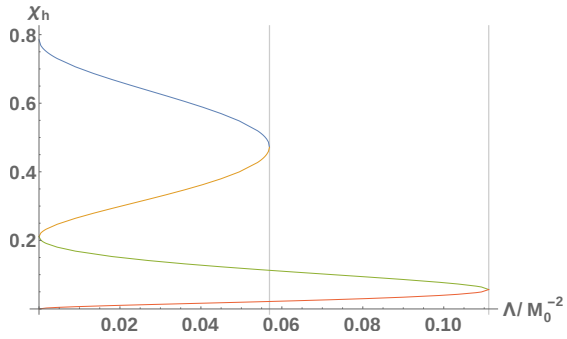

(b) 8 masses.

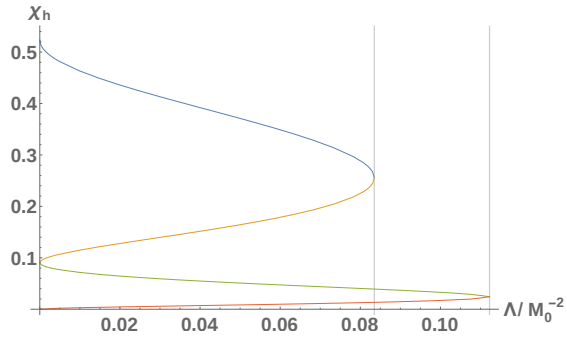

(c) 16 masses.

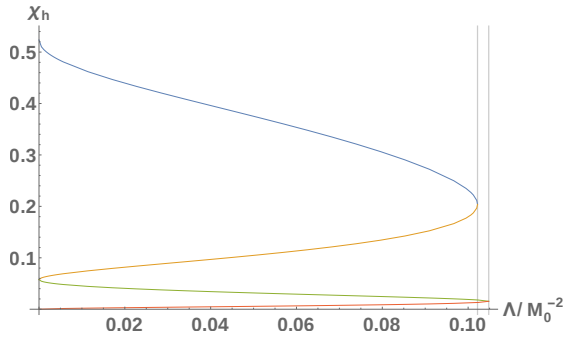

(d) 24 masses.

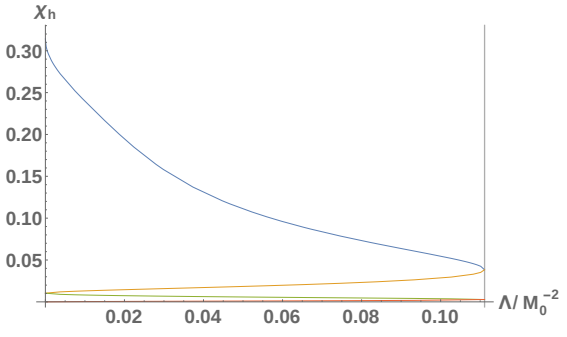

(e) 120 masses.

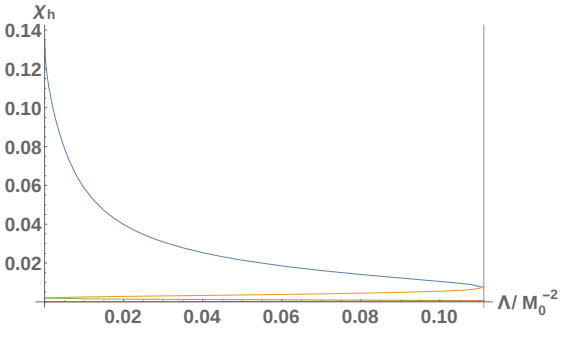

(f) 600 masses.

Figure 5.3: The positions of the four possible horizons in each of the six lattice universes as a function of Λ. The blue (orange) line corresponds to a marginally inner trapped cosmological (black hole) horizon, whilst the green (red) line corresponds to a marginally outer trapped black hole (cosmological) horizon. The vertical lines represent the value of Λ after which no solutions to Equation (5.18) exist.

Figure 5.3 can be used to determine the distance between neighbouring black holes for every value of Λ in each of the six possible configurations.

5.5 Cosmologically Viable Solutions

In the previous section we showed that there were certain values of Λ above which, no apparent horizons could be found. This means in order for our solutions to remain as cosmological models and to compare them to their FLRW versions, we need to ensure the horizons, both cosmological and black hole, do indeed exist, and therefore, impose bounds on our values of Λ. In this section we look at these bounds in more detail. A further motivation is provided by the fact that in the Schwarzschild-de Sitter solution, it is known that cosmological and black hole horizons exist provided $0 < M_0^2\Lambda < 1/9$.

The vertical lines in Figure 5.3 have already been used to denote the location of the point where the black hole and cosmological horizons become degenerate. Here we will collect these results, for each of the six lattice models, to consider the behaviour of the upper bound on $M_0^2\Lambda$ as a function of the number of masses in the universe. We present this information graphically in Figure 5.4. It is manifest that two different phenomena arise as the number of masses increases. The first is that the critical values for Λ, after which there are no horizons, converge to the same value for both $\alpha_2 = +1$ and $\alpha_2 = -1$. The second is that the value to which they converge is the same value as the upper bound in the Schwarschild-de Sitter solution, $M_0^2\Lambda = 1/9$. This is not unexpected, as for large values of N the distance between neighbouring masses increases, and the overall contribution from any individual black hole to the spacetime of any other diminishes. In other words, increasing N isolates each black hole to the point that it can be very well approximated by the Schwarzschild-de Sitter solution.

It is also interesting to see if a varying lower limit for ΛM_0^2 exists, or whether it is always bound from below by zero. One way of determining this is to look at the gradients of both sides of Equation (5.18) and see if it always true that $\partial_\chi\left(\sqrt{3\Lambda}E^{11}\right) > \partial_\chi\left(\psi^{-2}\partial_\chi\left(E^{11}\right)\right)$, for arbitrarily small values of Λ. If it is, then the inner black hole and cosmological horizons should be expected to exist and to remain separate. We calculated these two functions numerically, and found the condition to be valid down to values of $\Lambda \sim \mathcal{O}\left(10^{-14}\right)$ and $\chi \sim \mathcal{O}\left(10^{-8}\right)$ for all six lattice models. This indicates the lower bound on ΛM_0^2 is always zero, at least as far as can be determined with machine precision calculations. This result agrees with the results

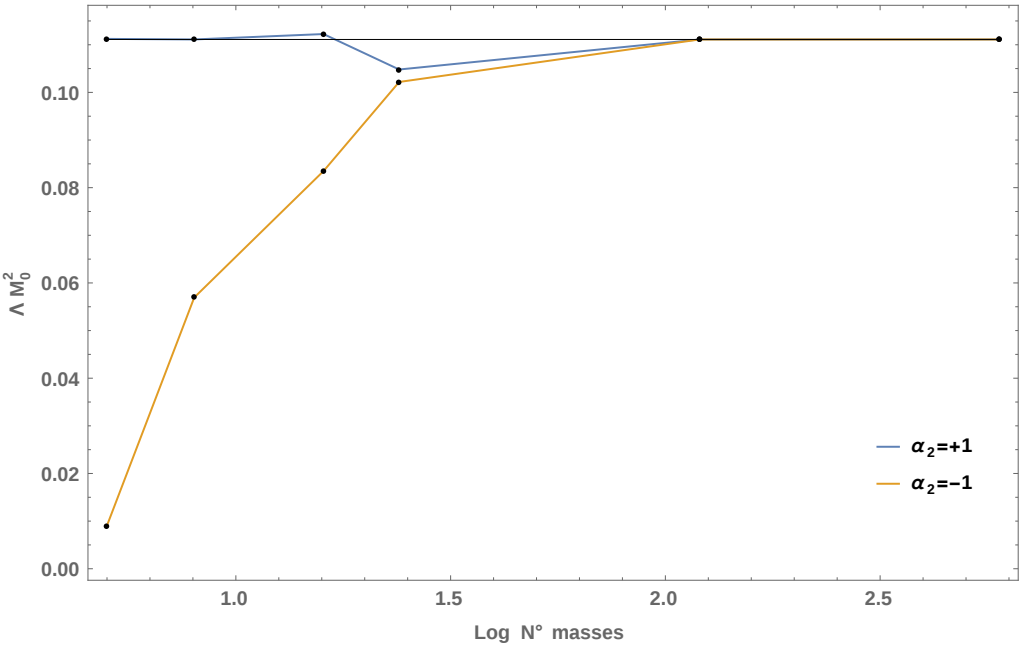

Figure 5.4: The upper bound on ΛM_0^2 as a function of the number of masses, for the outer horizons (blue) and the inner horizons (yellow). The solid line corresponds to the Schwarzschild-de Sitter value of 1/9.

of [169], who found that an inner cosmological horizon always exists in the case of an infinite flat lattice.

5.6 Deceleration Parameter

Previously, a way to compare our lattices with their corresponding FLRW versions was to look at the ratio of scale factors, as in [3] and here in chapter 4. As our intrinsic geometry remains unchanged from these original lattices, there will be little point in calculating these same quantities again. Instead, a new way to compare our inhomogeneous lattices with their homogeneous FLRW counterparts is to look at the deceleration parameter q. The reason for this is twofold - firstly, it was previously incalculable for the $\Lambda = 0$ case, as explained further on, but secondly, its relevance in being a measure of the rate of change of expansion of space is that adding Λ itself means we are considering an expanding (or contracting) hypersurface as we have seen. The deceleration parameter is a dimensionless quantity, and for an FLRW universe is defined as

$$q \equiv -\frac{a\ddot{a}}{\dot{a}^2} \tag{5.19}$$

where overdots denote derivatives with respect to the proper time of comoving observers t. The Friedmann equations for an FLRW universe containing pressureless dust and Λ were given in Equations (2.81) and (2.82). In an FLRW solution, $K = -3\dot{a}/a$, $\tilde{\mathcal{R}} = 6k$ and the electric part of the Weyl tensor (proportional to $\psi^{-1}\tilde{D}^2\psi$) plays the role of the energy density in the effective Friedmann equations [82]. Recall for the inhomogeneous lattices our choice for the extrinsic curvature to solve the constraint equations was $K^2 = 3\Lambda$ and we also had the Helmholtz equation for the conformal factor, $8\tilde{D}^2\psi = \psi\tilde{\mathcal{R}}$. Looking at the above FLRW solution results and the Friedmann equations means we can immediately see that the most closely analogous FLRW solutions to these choices are those that obey the conditions

$$\frac{\dot{a}^2}{a^2} = \frac{\Lambda}{3} \qquad \text{and} \qquad \frac{8\pi\rho}{3} = \frac{k}{a^2}. \tag{5.20}$$

These can then be used to calculate the deceleration parameter in Equation (5.19) which is

$$q = \frac{4\pi\rho}{\Lambda} - 1, \tag{5.21}$$

and will be used for both the black hole lattices and the comparison FLRW cosmological models. For the lattices, the energy density ρ will be the sum of proper masses of all the black holes, whilst for the FLRW universes ρ is the energy density in dust at the moment described in Equation (5.20). There are many other ways to construct measures of deceleration in inhomogeneous universes, and ours is a choice that is relatively simple and allows for direct comparison between our two cosmologies.

As in previous chapters, the particular way in which we compare our two cosmologies is to calculate the ratio of deceleration parameters, as shown below,

$$\frac{q_L}{q_F} = \frac{4\pi\rho_L - \Lambda}{4\pi\rho_F - \Lambda}, \tag{5.22}$$

where q_L is the deceleration parameter for the black hole lattices, ρ_L their energy densities, and q_F and ρ_F the same quantities but calculated for the FLRW universes. For vanishing Λ the first term on the right-hand side of Equation (5.21) diverges which means this quantity cannot be defined in that case. For non-zero Λ however, the deceleration parameter is finite and so our ratio of deceleration parameters is well-defined.

Lastly, in order to compare between the two cosmologies we impose that the total mass within them is the same, i.e. the sum of the proper masses of the black holes is equal to the total mass of the fluid of dust, as previously. This ensures we are also

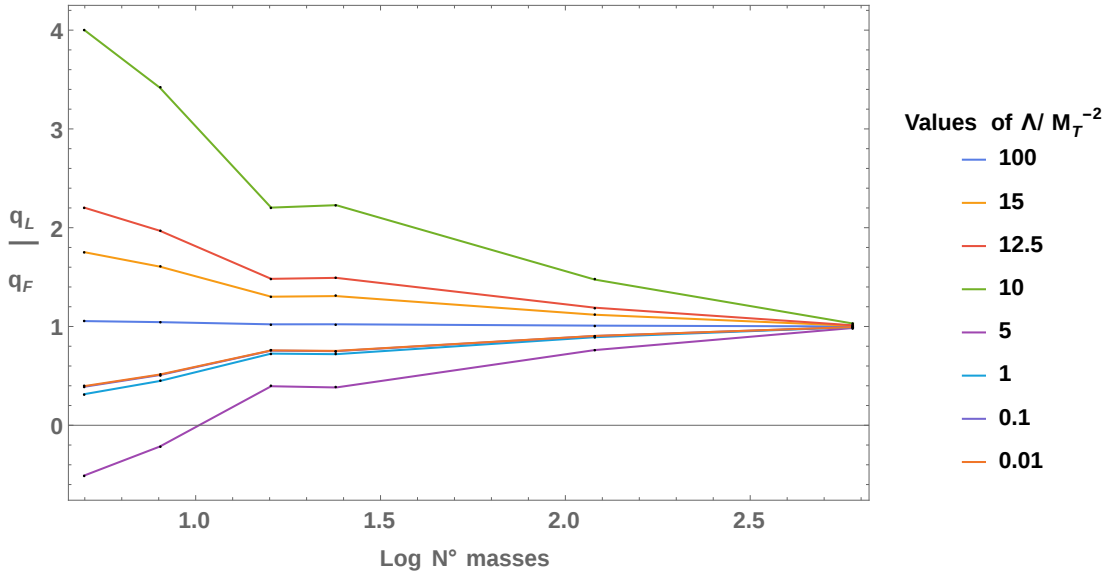

Figure 5.5: The ratio of the deceleration parameter in the lattice universe, compared to the corresponding FLRW universe, in each of the six possible tessellations of the 3-sphere. Each curve corresponds to a different value of Λ, in units of M_T^{-2}.

choosing which of the infinite family of solutions that satisfy Equation (5.20) to use. From this, we have expressions for the energy densities which are given by

$$\rho_L = \frac{M_T}{2\pi^2}\frac{1}{a_L^3} \qquad \text{and} \qquad \rho_F = \frac{M_T}{2\pi^2}\frac{1}{a_F^3}\,, \tag{5.23}$$

where $M_T = \sum_i M_i$ is the total mass in the universe and where a_L and a_F denote the global scale factors in the lattice and fluid models respectively. We have also taken the volume of a hypersurface of constant t to be given by $V = 2\pi^2 a^3$. Regarding the scale factors, these were previously calculated in [3], and can be seen in the final column of Table 3.2.

We can now calculate the ratio of deceleration parameters in Equation (5.22) as a function of the combination ΛM_T^2. It can be seen that in the limit $\Lambda \to \infty$, both q_L and $q_F \to -1$. For small values of Λ the deceleration parameters q_L and q_F are both large and positive (diverging in the limit $\Lambda \to 0$, as discussed above). These properties are true for each of the six tessellations of the 3-sphere and are non-surprising due to the form of the expression in Equation (5.22).

Fig. 5.5 shows the ratio of our two deceleration parameters, evaluated at different values of Λ. As the number of masses increases the ratios tend to unity for all values of Λ. This is to be expected, as for large values of N we have $a_L \approx a_F$, which implies $\rho_L \approx \rho_F$ and therefore $q_L/q_F \approx 1$. When Λ is large, $100 M_T^{-2}$, the ratio of deceleration

parameters is approximately unity regardless of N. When Λ is very small, the ratio of deceleration parameters reduces to $\rho_L/\rho_F = (a_F/a_L)^3$. This is shown by the curves corresponding to $0.1M_T^{-2}$ and $0.01M_T^{-2}$, which are indistinguishable from each other. On the other hand, for intermediate values of Λ, when $4\pi\rho_F = \Lambda$, the same ratio diverges. Using Equation (5.23) and the fact that $a_F = \frac{4M_T}{3\pi}$ this occurs at $\Lambda \approx 8.33M_T^{-2}$, for which the green curve is a good indicator of this divergence in ratio. All values of Λ below this critical value give $q_L/q_F < 1$, while all values above it give $q_L/q_F > 1$.

5.7 Numerical Evolution

The work in this thesis provides initial data for the constraint equations, which can be evolved using numerical relativistic techniques to satisfy the evolution equations. When $\Lambda = 0$ the initial hypersurface is time-symmetric, meaning that evolving the initial data in either direction in time means evolving it towards a cosmological singularity, where numerical errors are likely to increase. Therefore, we believe the work in this chapter has certain benefits over the corresponding work without Λ. Furthermore, the work in this chapter is particularly interesting because the addition of a cosmological constant Λ allows for expanding hypersurfaces as we have seen. It would therefore be of interest to numerically evolve the initial data and see the effects this has. We can go one step further and impose a constraint on our initial data such that the hypersurfaces are always expanding, as we believe our own Universe is.

To do this we look at the first Friedmann equation in Equation (2.81) and demand that firstly, if the universe is no longer expanding, then

$$H = \dot{a}/a = 0 \quad \textit{iff} \quad \frac{8\pi\rho}{3} - \frac{k}{a^2} + \frac{\Lambda}{3} = 0. \tag{5.24}$$

Using the fact that $\rho = \rho_0 a_0^3/a^3$, this can be rewritten as

$$\begin{aligned} &\frac{8\pi\rho_0 a_0^3}{3} - ka + \frac{\Lambda}{3}a^3 = 0 \\ &= \frac{8\pi\rho_0 a_0^3}{3}\left(1 - \frac{3ka}{8\pi\rho_0 a_0^3} + \frac{\Lambda}{8\pi\rho_0 a_0^3}a^3\right) = 0. \end{aligned} \tag{5.25}$$

From Equation (5.20) we have that $8\pi\rho_0/3 = k/a_0^2$ which can be rearranged to give $a_0 = 8\pi c/(3k)$ where $c = \rho_0 a_0^3$. Choosing $a_0 = 1$ gives Equation (5.25) as being

$$1 - a + \frac{\Lambda}{8\pi\rho_0}a^3 = 0. \tag{5.26}$$

There are no points where this is satisfied, and hence no points where $H = 0$, if $\Lambda/(8\pi\rho_0) > 4/27$. Defining density parameters for Λ and matter respectively as,

$$\Omega_\Lambda \equiv \frac{\Lambda}{3H_0^2} \text{ and } \Omega_m \equiv \frac{8\pi\rho_0}{3H_0^2}, \tag{5.27}$$

finally gives this bound as

$$\Omega_\Lambda > \frac{4}{27}\Omega_m, \tag{5.28}$$

as the criteria to be satisfied for eternal expansion. If we substitute in the Planck value for the density parameters for matter, which is 0.3, we see that eternal expansion occurs provided $\Omega_\Lambda > 0.044$, which at $\Omega_\Lambda = 0.7$, is most always satisfied.

An advantage of our work providing the initial data is that it is exact. Previous attempts have made use of numerical solutions where numerical errors will only grow during the time evolution, thus our work minimises the growth of these errors by being an exact solution.

5.8 Discussion

In this chapter we provided and studied exact initial data for a universe that contains regularly arranged black holes in a hyperspherical universe and in the presence of a cosmological constant. We determined the proper mass of the black holes by considering the constant mean curvature foliation of the Schwarzschild-de Sitter spacetime, and found that the intrinsic geometry remains unchanged from the $\Lambda = 0$ case. We then found expressions for the locations of the black hole and cosmological horizons and determined numerical values for the positions of these horizons in each of the six possible lattice universes. We found that there are upper bounds on the value of ΛM_0^2, where M_0 is the proper mass of the black holes in this spacetime, and that this upper bound converges to the Schwarschild-de Sitter value as the number of masses in the universe is increased. These results give qualitative agreement with the numerical work found performed in [169] when considering the inner black hole and cosmological horizons, but appear to disagree when considering the outer horizons. We expect that the source of this disagreement is due to the freedom that exists to change the scale of the size of the cells in the flat lattice that the authors of this study had been considering. No such freedom exists in the hyperspherical lattices that we have studied, which makes them much more rigid, and thus changes the relationship between the positions of black hole horizons and cosmological horizons.

We then studied the change in deceleration parameter due to inhomogeneity in

spaces of this type, by comparing to positively curved FLRW models that contain the same cosmological constant and dust with the same total proper mass. We found that the backreaction effect from inhomogeneity decreases as the number of masses is increased, and as the value of the cosmological constant becomes large.

Finally we found an interesting requirement for our models to be eternally expanding, which could prove useful for future numerical evolution, and would allow our models to be compared to those that exist in the literature that have had the time evolution studied.

In this chapter and the preceding one we have completed our analyses and discussion of generalising the existing black hole lattices to those that start to resemble the complexity and nature of our own Universe, by adding structure and considering expanding hypersurfaces. In the following chapters we extend the lattices in a slightly different way, to include electric charge as well as an alternative gravitational theory. These constitute more mathematical explorations into backreaction in inhomogeneous cosmologies.

6 Solutions with Charged Black Holes

This chapter is based on [37] and the calculations presented here were performed by Rashida Bibi.

6.1 Introduction

In this chapter we extend our existing catalogue of black hole lattice initial data to include electric charge. This allows for Reissner-Nordström-like black holes [172] as well as other types of charged astrophysical bodies [173] to be included in cosmology. We find that as the magnitude of the charge is increased, the discrepancy between the charged lattice models and the corresponding FLRW solutions reduces and that the horizon size of each black hole decreases.

There are several motivations for including electric charge. Firstly, it offers a generalisation of existing models, analogous to the generalisation from Schwarzschild to Reissner-Nordström in the study of static black holes. We expect this to give new mathematical and physical insights into the nature of these inhomogeneous cosmologies. By definition, an FLRW universe forbids regions of charged spacetime due to the homogeneity requirement, thus our addition of charge and inhomogeneity allows us to investigate a previously unexplored area, and the cosmological consequences of such universes. As before, we use the black hole lattices to study this problem in a well-defined and precise way. In addition, this work generalises the well-known Majumdar-Papapetrou and Kastor-Traschen solutions for multiple extremal black holes with $|q| = m$ [104, 105, 107] to the case where the black holes have $|q| \neq m$. Finally, the inclusion of electric charge offers a way to break the discrete rotational symmetries that might otherwise exist within these lattice cosmologies, as we find that the black holes must necessarily contain non-identical charges.

This rest of this chapter is organised as follows: in section 6.2 we review the Einstein-Maxwell constraint equations on a time-symmetric hypersurface. In section

6.3 we derive initial data for a cosmological model that contains electrically charged black holes and specifically focus on the 8-mass cubic lattice. The apparent horizons are considered in section 6.4 before being compared to a Friedmann cosmology in section 6.5. Finally we conclude in section 6.6.

6.2 Einstein-Maxwell

The Einstein-Maxwell equations that govern electromagnetic fields in the presence of gravitation are given by

$$R_\nu^{\ \mu} - \frac{1}{2}\delta_\nu^{\ \mu} R = \frac{1}{2}\left(F_{\nu\alpha}F^{\alpha\mu} - \frac{1}{4}\delta_\nu^{\ \mu} F_{\alpha\beta}F^{\alpha\beta}\right) \equiv 8\pi T_\nu^{\ \mu}, \tag{6.1}$$

where $R_\nu^{\ \mu}$ is the Ricci tensor, and R is the Ricci scalar. The Faraday tensor is denoted by $F_\nu^{\ \mu}$, and obeys the following differential relations,

$$\nabla_\nu F^{\mu\nu} = 0 \quad \text{and} \quad \nabla_{[\alpha} F_{\mu\nu]} = 0. \tag{6.2}$$

Our aim is to solve these equations to obtain the geometry of a universe that contains N electrically charged black holes.

To find the relevant initial data for this system, we start by choosing a spacelike hypersurface with metric h_{ij} and normal u^μ. The Hamiltonian and momentum constraint equations from Equation (6.1) are then given by

$$\mathcal{R} + K^2 - K_{ij}K^{ij} = 16\pi\rho \tag{6.3}$$

$$D_j\left(K_i^{\ j} - \delta_i^{\ j} K\right) = 8\pi S_i, \tag{6.4}$$

respectively, where $\mathcal{R}$ is the Ricci curvature scalar of the initial 3-dimensional space, K_{ij} is the extrinsic curvature of this 3-space in the 4-dimensional spacetime, and where the energy and momentum densities are given by

$$\rho \equiv T_{\mu\nu}u^\mu u^\nu \quad \text{and} \quad S_i \equiv -\delta_i^{\ j} u^\mu T_{\mu j}, \tag{6.5}$$

respectively. All indices in these expressions are raised and lowered with the metric of the 3-space h_{ij}.

If we choose a time-symmetric initial hypersurface and matter fields then $K_{ij} = 0$, while $F_{i\mu} = -E_i u_\mu$ and $F_{ij} = 0$. This means that $\rho = E_i E^i$ and $S_i = 0$ and the

energy constraint Equation (6.3) becomes

$$\mathcal{R} = 2E_i E^i \tag{6.6}$$

whilst the momentum constraint Equation (6.4) is satisfied trivially. Simultaneously, the differential relations from Equation (6.2) imply

$$D_i E^i = 0. \tag{6.7}$$

We have a solution to the constraint equations if Equations (6.6) and (6.7) are both satisfied. This provides the initial data for a unique evolution under the six remaining Einstein-Maxwell equations in Equation (6.1) and the three evolution equations in Equation (6.2) [174].

Let us now make the following ansätze. We proceed analogously as in previous chapters and write the metric as

$$ds^2 = \Omega^2 \psi^2 \tilde{h}_{ij} dx^i dx^j, \tag{6.8}$$

where ψ and Ω are functions of all spatial coordinates and where $\tilde{h}_{ij}$ is the metric of a conformal 3-dimensional space of curvature $\tilde{\mathcal{R}}$ = constant. Secondly, we choose as in [166],

$$E_i = \partial_i[\ln(\Omega/\psi)]. \tag{6.9}$$

The time-symmetric constraint Equations (6.6) and (6.7) then become

$$\tilde{D}^2\Omega = \frac{\tilde{\mathcal{R}}}{8}\Omega \quad \text{and} \quad \tilde{D}^2\psi = \frac{\tilde{\mathcal{R}}}{8}\psi, \tag{6.10}$$

where $\tilde{D}^2$ indicates a covariant Laplacian with respect to the metric $\tilde{h}_{ij}$. These are both Helmholtz equations for the two functions Ω and ψ. Solutions to this are well known, and as long as Ω and ψ are not directly proportional, it can be seen that $E_i \neq 0$. The reader may note that for periodic lattices of black holes the equations in Equation (6.10) can have positive energy solutions only if $\tilde{\mathcal{R}}$ is positive (see [162] for proof).

6.3 Initial Data

Proceeding in the usual way we choose $\tilde{h}_{ij}$ to be the metric of a 3-sphere. By noting that Equations (6.10) are both linear and by recognising that $f \propto 1/\sin(r/2)$ is a

solution, we can write solutions to these equations more generally as

$$\Omega = \sum_{i=1}^{N} \frac{c_i}{2\sin\left(r_i/2\right)}, \tag{6.11}$$

$$\psi = \sum_{i=1}^{N} \frac{d_i}{2\sin\left(r_i/2\right)}, \tag{6.12}$$

where i runs from 1 to N, c_i and d_i are two sets of N constants (yet to be determined), and r_i denotes the value of the r coordinate after rotating the sphere so that the i^{th} pole is located at $r_i = 0$. As previously, these solutions contain N poles on the conformal 3-sphere located at arbitrarily chosen locations. Each of these poles will correspond to an electrically-charged mass point at the centre of a black hole in a cosmological model.

A slice through Reissner-Nordström

We must now relate the constants c_i and d_i to the charge and mass of each of the black holes in order for the geometry to be fully specified. We expect that each of these constants will be some combination of both mass and charge. To find the relation, recall that the Reissner-Nordström solution in $(t,\, \sigma,\, \theta,\, \phi)$ coordinates with mass m and charge q can be written as

$$ds^2 = -\left(1 - \frac{2m}{\sigma} + \frac{q^2}{\sigma^2}\right) dt^2 + \frac{d\sigma^2}{\left(1 - \frac{2m}{\sigma} + \frac{q^2}{\sigma^2}\right)} + \sigma^2\left(d\theta^2 + \sin^2\theta d\phi^2\right). \tag{6.13}$$

Transforming from σ to ρ as follows,

$$\sigma = \rho\left(1 + \frac{m}{2\rho}\right)^2 - \frac{q^2}{4\rho}, \tag{6.14}$$

allows us to write a time-symmetric slice as

$$ds^2 = \left(1 + \frac{m-q}{2\rho}\right)^2 \left(1 + \frac{m+q}{2\rho}\right)^2 \left(d\rho^2 + \rho^2 d\theta^2 + \rho^2 \sin^2\theta d\phi^2\right). \tag{6.15}$$

We still need to write this metric in the form of Equations (6.8), (6.11) and (6.12), in order to transform the conformal 3-space plane to a sphere. To do this, we perform one final coordinate transformation given by $\rho = k\tan(r/2)$, where k is a constant,

and obtain

$$ds^2 = \frac{k^2}{4}\left(\frac{1}{\cos(r/2)} + \frac{m-q}{2k\sin(r/2)}\right)^2\left(\frac{1}{\cos(r/2)} + \frac{m+q}{2k\sin(r/2)}\right)^2 d\tilde{s}^2, \tag{6.16}$$

where $d\tilde{s}^2$ is the usual line-element on a 3-sphere. Finally, choosing $2k = \sqrt{m-q}\sqrt{m+q}$, we get

$$ds^2 = \left(\frac{\sqrt{m+q}}{2\sin(r/2)} + \frac{\sqrt{m-q}}{2\cos(r/2)}\right)^2\left(\frac{\sqrt{m-q}}{2\sin(r/2)} + \frac{\sqrt{m+q}}{2\cos(r/2)}\right)^2 d\tilde{s}^2. \tag{6.17}$$

This result is of exactly the form that we would have obtained from considering Equations (6.8), (6.11) and (6.12) with one mass positioned at $r = 0$ and a second mass positioned at $r = \pi$. The two geometries are formally identical if we further choose $c_1 = d_2 = \sqrt{m+q}$ and $c_2 = d_1 = \sqrt{m-q}$. This means that the time-symmetric initial data for the Reissner-Nordström solution is a special case of our more general initial data, with one mass of charge $+q$ at $r = 0$ and a second mass of charge $-q$ at $r = \pi$.

N arbitrarily positioned charged black holes

Let us now consider the general case where N masses are at arbitrarily chosen positions. By using Equation (6.16), and in the vicinity of a mass point, we can relate c_i and d_i to the mass m_i of each of the black holes in any arbitrary distribution of points. First we rotate coordinates as before such that the ith mass appears at $r = 0$. We can then expand the terms in Equation (6.8) to find in the limit $r \to 0$,

$$ds^2 = \left(\frac{c_i}{r} + \sum_{j\neq i}\frac{c_i}{2\sin\left(r_{ij}/2\right)}\right)^2\left(\frac{d_i}{r} + \sum_{j\neq i}\frac{d_i}{2\sin\left(r_{ij}/2\right)}\right)^2 d\tilde{s}^2, \tag{6.18}$$

where r_{ij} is the coordinate distance between the positions of the ith and jth masses. Comparing this equation with the expanded version of Equation (6.16) at $r = 0$ allows us to read off the coefficients of the leading-order terms to obtain:

$$k = \frac{1}{2c_i d_i}\left(c_i\sum_{j\neq i}\frac{d_j}{2\sin\left(r_{ij}/2\right)} + d_i\sum_{j\neq i}\frac{c_j}{2\sin\left(r_{ij}/2\right)}\right) - \frac{q_i^2}{2c_i d_i}, \tag{6.19}$$

and

$$m_i = c_i\sum_{j\neq i}\frac{d_j}{2\sin\left(r_{ij}/2\right)} + d_i\sum_{i\neq j}\frac{c_j}{2\sin\left(r_{ij}/2\right)}. \tag{6.20}$$

The former of these equations is a relation between the coordinate systems of the Reissner-Nordström solution and our multi-black hole solution around one of our mass points. The latter however is an expression for the mass of each of our black holes. The above analysis shows that the geometry of space in the vicinity of any one of the black holes will be similar to a Reissner-Nordström black hole with mass m, where m is given by Equation (6.20), provided a multi-black hole solution is specified with a full set of $c_i's$ and $d_i's$.

We will now identify the electric charge of each of our black holes. A general definition of electric charge within a region Ω is given by [166]

$$q_i \equiv \frac{1}{4\pi}\int_{\partial\Omega} E_i n^i dS \tag{6.21}$$

where E_i is the electric field and n^i is the unit inward-pointing normal. For our black holes it is convenient to take the boundary $\partial\Omega$ to correspond to asymptotic infinity, on the far side of the Einstein-Rosen bridge. This gives

$$n^i = \left(\frac{-1}{\psi\Omega}, 0, 0\right), \tag{6.22}$$

and $dS = \psi^2\Omega^2 r^2 \sin\theta d\theta d\phi$. In both of these expressions Ω and ψ should be evaluated in the limit $r \to 0$. Evaluating Equation (6.21) in this limit, and using Equations (6.11), (6.12) and (6.22) gives

$$q_i = c_i \sum_{j\neq i} \frac{d_j}{2\sin\left(r_{ij}/2\right)} - d_i \sum_{j\neq i} \frac{c_j}{2\sin\left(r_{ij}/2\right)}. \tag{6.23}$$

This equation is an expression for the charge on the mass at position $r_i = 0$, and can equally be used to evaluate the charge on every other black hole in our solution. The total charge in the universe is zero and is independent of how the black holes are distributed and their masses, as we note that Equation (6.23) immediately gives $\sum_i q_i = 0$. Physically this makes sense, as lines of flux can only end on masses in a closed cosmology.

Adding and subtracting the Equations (6.20) and (6.23) gives the following

$$m_i + q_i = c_i \sum_{j\neq i} \frac{d_j}{\sin\left(r_{ij}/2\right)}, \tag{6.24}$$

$$m_i - q_i = d_i \sum_{j\neq i} \frac{c_j}{\sin\left(r_{ij}/2\right)}, \tag{6.25}$$

however, this is still a system of non-linear equations, which makes it difficult to solve for the c_i and d_i directly, after the desired m_i and q_i have been specified.

A periodic universe with eight charged black holes

The simplest solution to Equations (6.24) and (6.25) is the case where all but one of the black holes is extremal, with $m_i = q_i$. If the one exceptional black hole is labelled $i = 1$, then vanishing total charge means that we must have $q_1 = -\sum_{i\neq 1} q_i = -\sum_{i\neq 1} m_i$. The only solutions to Equations (6.24) and (6.25) then have $m_1 = -q_1$, and we have the initial data for a Majumdar-Papapetrou [104, 105] solution with spatial infinity transformed into the black hole with $i = 1$. We wish to extend these results to consider non-extremal black holes. We do this in the next section, in which an exact solution for c_i and d_i can be found once the mass and charge of each of the black holes has been specified.

Determining the sets of constants c_i and d_i

For simplicity and in the rest of this chapter, our analyses considers only one of the six lattice models - the 8-mass cubic lattice. Physically this corresponds to considering a 4-dimensional Euclidean embedding space, within which a hypercube is placed within a 3-sphere, and by ensuring that the vertices of the hypercube are all touching the hypersphere simultaneously (i.e. by circumscribing the cube with the sphere). Lines can be drawn between the points where these two structures touch, which are just the edges of eight equal-sized cubes, and as we have seen are the primitive lattice cells of this particular tiling.

An interesting feature arises in the regular 8-mass universe, in that each of the black holes is antipodal to another black hole, just as in the time-symmetric slice through the Reissner-Nordström solution discussed in the previous section. This can be verified by looking at the final column of Table 4.2 in chapter 4. This lists the coordinates of the location of each mass in both a set of Cartesian coordinates in the 4-dimensional Euclidean embedding space, as well as in a set of hyperspherical polar coordinates intrinsic to the 3-space itself. The reader should note that the χ coordinates in chapter 4 are simply the r coordinates used in this chapter. Taking a hint from the existence of the time-symmetric Reissner-Nordström geometry, we can now choose the c_i and d_i of these 8 masses such that the c_i from each mass is equal

to the d_i of the antipodal mass,

$$c_1 = c_3 = c_5 = c_7 = d_4 = d_6 = d_8 = e - f \tag{6.26}$$

$$c_2 = c_4 = c_6 = c_8 = d_3 = d_5 = d_7 = e + f \tag{6.27}$$

where e and f are constants (yet to be determined). From Equations (6.24) and (6.25) this choice then allows us to determine that

$$m_1 = m_2 = m_3 = m_4 = m_5 = m_6 = m_7 = m_8 = (1 + 6\sqrt{2})e^2 + f^2 \tag{6.28}$$

$$q_1 = -q_2 = q_3 = -q_4 = q_5 = -q_6 = q_7 = -q_8 = -2(1 + 3\sqrt{2})ef. \tag{6.29}$$

Each of the 8 black holes has an identical mass to the others, while having an equal and opposite electric charge to its antipodal partner. This is simplest way to satisfy the requirements of vanishing total electric charge of all black holes and some degree of regularity.

Finally, it is now straightforward to solve Equations (6.28) and (6.29) for e and f to get

$$e = \frac{\sqrt{(19 + 6\sqrt{2})m + \sqrt{(433 + 228\sqrt{2})m^2 - (91 + 120\sqrt{2})q^2}}}{\sqrt{(182 + 240\sqrt{2})}}, \tag{6.30}$$

and $f = -q/2(1 + 3\sqrt{2})e$, where $m = m_i$ is the mass of each black hole and $|q| = |q_i|$ is the magnitude of the charge on each black hole (with sign chosen so that $q = q_1$). We now have an explicit solution where half of the black holes have positive charge while the other half have negative charge, but all black holes have equal mass.

6.4 Apparent Horizons

As shown in previous chapters, it is of interest to determine the location of the horizons around each of the black holes, and this chapter is no exception. For this work, it will be to ensure that there is no overlap in the horizons corresponding to different black holes, so that the solution can reasonably be referred to as a cosmological model. As before, the position of the apparent horizon can be determined from the initial data and we will therefore use this surface to approximate the location of the horizon of each of our black holes. Recall the apparent horizon is the outermost marginally outer trapped surface. As our initial data is time-symmetric, this surface must be an

extremal surface in this 3-space. Proceeding in the same way as in section 4.3, it is enough to use the area method to approximate its location. Analogously to Equation (4.15), we rotate our 3-sphere until one of the masses appears at $r = 0$. Then the area of any sphere centered on this mass is given by

$$A = \int_0^{2\pi} \int_0^{\pi} \psi^2 \Omega^2 \sin^2 r \sin\theta d\theta d\phi \tag{6.31}$$

where $r =$ constant. Integrating and minimising then gives us a good approximation to the location of the black hole horizon. The true area of the apparent horizon is that of a minimal sphere in the initial geometry, meaning this method of assuming a sphere of constant coordinate radius to approximate the apparent horizon necessarily produces a slight overestimate of the horizon area. However, as long as the horizons are well separated, this error is expected to be very small [82].

Figure 6.1 shows the results of calculating the position of the apparent horizon in this way, where we display the r coordinate of the apparent horizon as a fraction of the coordinate distance between neighbouring black holes. It is clear that the black hole horizons in our 8-mass model never touch, as when $q/m \to 0$, the horizon extends about 27% of the way to the halfway point between black holes, as expected from previous work. The horizon then shrinks back towards the centre of the black hole as the charge on the black hole is increased, to either positive or negative values, until it reaches zero in the limit $q/m \to \pm 1$. Our results show similar behaviour to what should be expected from a maximal slice through a Reissner-Nordström black hole.

6.5 FLRW Comparison

We further extend previous results concerning cosmologies filled with uncharged black holes and consider the cosmological effects of electrical charge. As before, we compare the scale of the cosmological region at the maximum of expansion between our charged lattice universes and their FLRW counterparts. The initial data constructed in section 6.3 can immediately be seen to be at such a maximum, as it was chosen to be time-symmetric. The line element containing the scale factor at the corresponding moment of time in a spatially closed and dust dominated FLRW model is given by Equation (3.16). By comparing this number to the scale of the cosmological region in our black hole spacetime we can then deduce the effect of discretely distributed electric charges with the mass condensed into a finite number

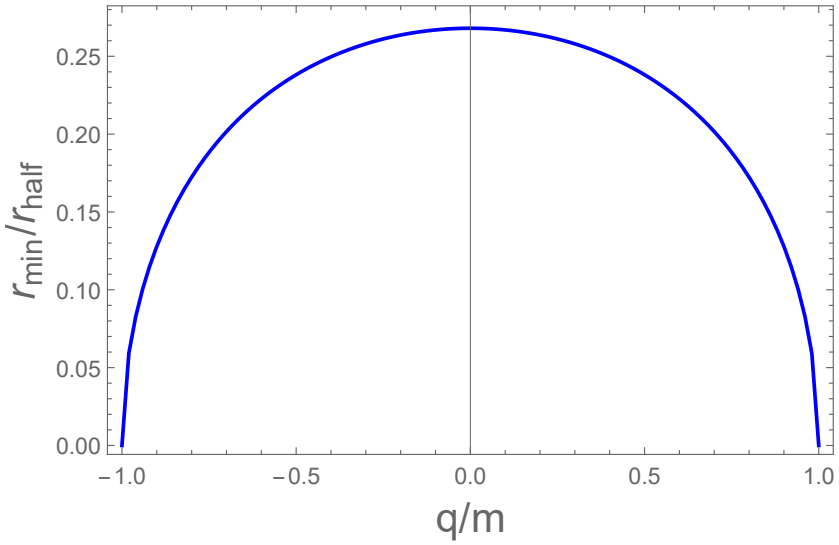

Figure 6.1: The position of the apparent horizon around one of our black holes $r_{\min}$, displayed as a fraction of the coordinate distance to the halfway point between black holes r_{half}. The value of $r_{\min} \to 0$ as $q/m \to \pm 1$.

of points.

For these charged lattices, we can determine the scale of the cosmological region by calculating the proper length of one of the edges of one of our lattice cells, exactly as definition D2 in Equation (3.18) and in [3]. If we rotate our solution until a cell edge lies along a curve with θ and ϕ being constant, then the proper length of the edge is given by

$$d = \int_{r_1}^{r_2} \sqrt{g_{rr}} dr = \int_{r_1}^{r_2} \psi \Omega dr, \tag{6.32}$$

where r_1 and r_2 are the coordinates of the end-points of the edge in question (i.e. the vertices of the lattice cell). The proper length of a curve that subtends the same angle in a closed FLRW model is given by

$$d_{\text{FLRW}} = \int_{r_1}^{r_2} a\left(t_{\max}\right) dr = \left(r_2 - r_1\right) a\left(t_{\max}\right), \tag{6.33}$$

where $a(t_{max})$ is the scale factor.

In general, the value of d_{FLRW} will depend only on the total mass in the space M (once the locations of the cell vertices have been chosen), whilst the value of d will depend on both the mass of the black holes and their charge (m and q). Proceeding as before we choose each cosmology to have the same total proper mass, i.e. $M = 8m$. It is manifest that the relevant comparison of scales in the two cosmologies will be given by $a/a_{FLRW} = d/d_{FLRW}$. This ratio is a function of only the charge to mass

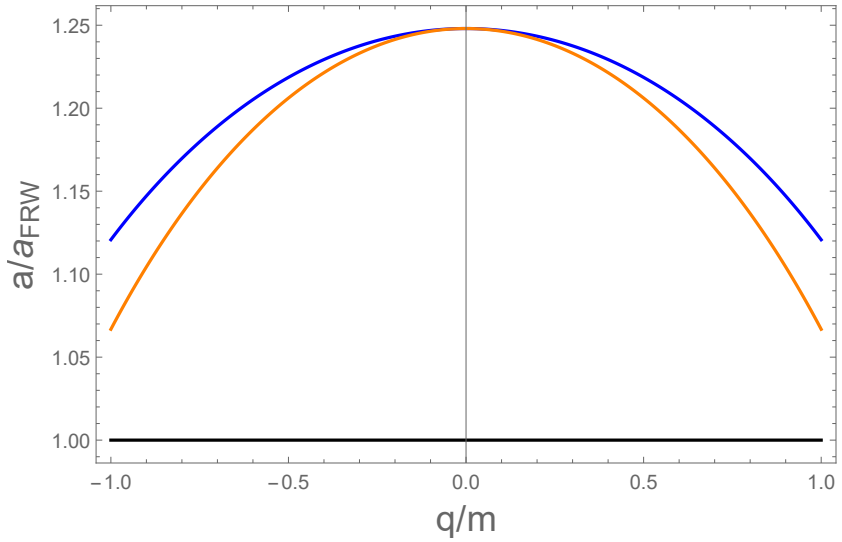

Figure 6.2: The scale of the cosmological region in our black hole lattice at the maximum of its expansion, compared to a spatially closed dust dominated FLRW model with the same mass. The orange line correspond to measuring the scale of the black hole universe along a curve that joins cells that contain three black holes with the same charge, whilst the blue line corresponds to two black holes with the same charge and a third with the opposite charge.

ratio of the black holes q/m, and reduces to the measure of cosmological backreaction studied previously in [3] in the limit $q \to 0$.

The value of the ratio of scale factors as a function of q/m is displayed in Figure 6.2. When $q/m \to 0$ we recover the results of the uncharged case, and as $q/m \to \pm 1$ the black holes become extremal. The difference from the predicted scale factor from FLRW cosmology is greatest when the black holes are uncharged. Thus, increasing the charges on the black holes decreases the discrepancy with FLRW, but the scale of the cosmological region in our black hole cosmology is always greater than that of the corresponding FLRW model, even when the black holes approach extremality. The two curves in Figure 6.2 correspond to the situations where the three cells that meet along the cell edge under investigation all contain black holes that have the same charge (orange line), or when two of the cells have the same charge and the other has the opposite charge (blue line). These two curves therefore describe every cell edge that exists within our eight-black hole modelas t, e rehsults do not depend on whether the same charges in these two situations are positive or negative; the ratio of scale factors is the same in either case.

6.6 Discussion

We have presented an analysis of a lattice of regularly arranged, charged black holes at maximum of expansion. This generalises existing work in the literature and provides insight into the effect that electric charge has on cosmological physics. We have found that the only solutions that exist are those that have zero net charge. We then applied this analysis to a specific model containing eight black holes, and found a relatively simply way of obtaining an uncharged universe overall - by demanding that black holes exist in antipodal pairs, and that each black hole has equal and opposite charge to its antipodal partner. We investigated the size of the apparent horizon as a function of this charge to mass ratio and found that as the magnitude of the charge of the black holes is increased the size of the apparent horizon decreases. In the limit where the black hole charges become extremal the apparent horizons recede to zero radius. We then compared this model to an FLRW model with positive spatial curvature containing the same total mass in dust and found that as the magnitude of the charge on the black holes was increased, the discrepancy between lattice and FLRW was reduced, with the largest discrepancy corresponding to the case where there is no charge.

Our work in this chapter completes our extension of the black hole lattices as far as general relativity is concerned. To recap, we have considered new initial data, either in the form of charged masses or a cosmological constant, as well as alternative arrangements of the masses themselves. In the next chapter we go one step further, and extend our lattices to a scalar-tensor theory of gravity, Brans-Dicke.

7 Solutions in Brans-Dicke Gravity

This chapter is based on [38].

7.1 Introduction

The preceding three chapters of this thesis have all shared a common theme - they have involved generalisations of the black hole lattices all within the same gravitational theory, general relativity. Here, and in our final chapter, we present some of the first steps to further generalise using an alternative gravitational theory. The theory we use is the one first introduced by Brans and Dicke [52], and introduced here in this thesis in section 2.1.5. While much work has been performed on understanding virtually every aspect of these theories (see e.g. [46, 175]), it is still the case that very little is known about their cosmological solutions away from the limits of homogeneity and isotropy. To date, the only studies in this area have been limited to highly symmetric matter configurations [176] or theories with well chosen self-interaction potentials [177]. We address this deficit by studying inhomogeneous cosmological configurations that admit no global symmetries, but which allow progress to be made using exact methods. We expect the spacetimes that result from our investigation to shed light on the consequences of structure formation in these theories, including the degree to which Newton's constant is allowed to vary in space near massive objects.

By extending the results of previous studies to new theories of gravity, we allow the general relativistic results to be considered within a wider context. It also significantly extends what is currently known about inhomogeneous cosmological models in scalar-tensor theories of gravity – a field that is severely restricted by the additional complexity of the field equations.

This final chapter is organised as follows: in section 7.2 we derive the relevant constraint equations for our initial data problem. In section 7.3 we investigate solutions to these equations, including expressions for the proper masses and scalar

charges for each of the point-like objects in section 7.4. Section 7.5 then contains a review of Friedmann cosmology in Brans-Dicke theory, and proceeds to compare the scale of our inhomogeneous models to these perfectly homogeneous and isotropic solutions in section 7.5.1. Finally, we conclude in section 7.6.

7.2 Deriving the Constraint Equations

It is not necessarily the case that alternative theories of gravity admit a well-posed initial value problem. For certain simple Horndeski theories (the most general scalar-tensor theories), of which Brans-Dicke is a subset, then there is an initial value problem which is indeed well-posed [178]. This allows us to proceed as in previous chapters and formulate the field equations as a set of Hamiltonian and momentum constraint equations. Recall the Lagrangian density for the Brans-Dicke theory, Equation (2.12), which when varied with respect to the appropriate fields, gave the field equations in Equations (2.13) and (2.14). Before we can construct our lattices by finding suitable initial data, we first need to derive the Hamiltonian and momentum constraint equations that correspond to these field equations. This is done by performing the usual $3+1$ decomposition, using the irrotational timelike unit normal n_μ and the projection tensor $h_{\mu\nu} = g_{\mu\nu} + n_\mu n_\nu$. All quantities can then be split into a temporal part, by contracting with n_μ, and a spatial part, by projecting with $h_{\mu\nu}$. In particular, the Gauss-Codazzi-Mainardi equations can be used to project the Einstein tensor such that

$$2G_{\mu\nu}n^\mu n^\nu = \mathcal{R} + K^2 - K_{\mu\nu}K^{\mu\nu}, \tag{7.1}$$

where $K_{\mu\nu} = -h_\mu{}^\rho h_\nu{}^\sigma \nabla_\rho n_\sigma$ is the extrinsic curvature of the hypersurfaces orthogonal to n^μ, K is its trace, and $\mathcal{R}$ is the Ricci curvature scalar of the space orthogonal to n^μ. As well as this we find

$$-h_\mu{}^\nu G_{\nu\sigma}n^\sigma = D_\nu K^\nu{}_\mu - D_\mu K, \tag{7.2}$$

where D_μ is the torsion-free covariant derivative on the hypersurface orthogonal to n^μ that is compatible with $h_{\mu\nu}$, and which is defined such that $D_\mu K_{\nu\rho} = h_\mu{}^\sigma h_\nu{}^\tau h_\rho{}^\chi \nabla_\sigma K_{\tau\chi}$ (for example). For general relativity in vacuum, the left-hand sides of both Equations (7.1) and (7.2) are zero. For Brans-Dicke theory, however this is not the case - the left-hand side is instead functions of the scalar field, ϕ.

When $T_{\mu\nu} = 0$, we can use Equation (2.13) to write the Hamiltonian constraint as

$$\mathcal{R} + K^2 - K_{\mu\nu}K^{\mu\nu} = 2\frac{\Box\phi}{\phi} + \frac{2}{\phi}n^\mu n^\nu \nabla_\mu\nabla_\nu\phi + \frac{\omega}{\phi^2}(\nabla\phi)^2 + \frac{2\omega}{\phi^2}n^\mu n^\nu \nabla_\mu\phi\nabla_\nu\phi\,, \quad (7.3)$$

where we have used $g_{\mu\nu}n^\mu n^\nu = -1$. The first and second terms on the right-hand side of Equation (7.3) can then be used to write

$$\begin{aligned}
&\frac{2}{\phi}\left(\Box\phi + n^\mu n^\nu \nabla_\mu\nabla_\nu\phi\right)\\
=&\frac{2}{\phi}Kn_\mu\nabla^\mu\phi + \frac{2}{\phi}\left(-Kn_\mu\nabla^\mu\phi + g^{\mu\nu}\nabla_\mu\nabla_\nu\phi + n^\mu n^\nu\nabla_\mu\nabla_\nu\phi\right)\\
=&\frac{2}{\phi}Kn_\mu\nabla^\mu\phi + \frac{2}{\phi}\left(-Kn_\mu\nabla^\mu\phi + h^{\mu\nu}\nabla_\mu\nabla_\nu\phi\right)\\
=&\frac{2}{\phi}Kn_\mu\nabla^\mu\phi + \frac{2}{\phi}\left(\nabla_\nu(n^\rho n_\mu)h_\rho{}^\nu\nabla^\mu\phi + h^{\mu\nu}\nabla_\mu\nabla_\nu\phi\right)\\
=&\frac{2}{\phi}Kn_\mu\nabla^\mu\phi + \frac{2}{\phi}\left(\nabla_\nu(h_\mu{}^\rho)h_\rho{}^\nu\nabla^\mu\phi + h^{\mu\nu}\nabla_\mu\nabla_\nu\phi\right)\\
=&\frac{2}{\phi}Kn_\mu\nabla^\mu\phi + \frac{2}{\phi}\left(\nabla_\nu(h_\mu{}^\rho\nabla^\mu\phi)h_\rho{}^\nu\right)\\
=&\frac{2}{\phi}Kn_\mu\nabla^\mu\phi + \frac{2}{\phi}D_\mu D^\mu\phi\,,
\end{aligned} \quad (7.4)$$

while the third and fourth terms can be written as

$$\begin{aligned}
&\frac{\omega}{\phi^2}\left(g^{\mu\nu}\nabla_\mu\phi\nabla_\nu\phi + 2n^\mu n^\nu\nabla_\mu\phi\nabla_\nu\phi\right)\\
=&\frac{\omega}{\phi^2}\left((h^{\mu\nu} - n^\mu n^\nu)\nabla_\mu\phi\nabla_\nu\phi + 2n^\mu n^\nu\nabla_\mu\phi\nabla_\nu\phi\right)\\
=&\frac{\omega}{\phi^2}\left(h^{\mu\nu}\nabla_\mu\phi\nabla_\nu\phi + n^\mu n^\nu\nabla_\mu\phi\nabla_\nu\phi\right)\\
=&\frac{\omega}{\phi^2}\left(D_\mu\phi D^\mu\phi + n^\mu\nabla_\mu\phi\, n^\nu\nabla_\nu\phi\right)\,.
\end{aligned} \quad (7.5)$$

Combining these results we have that the Hamiltonian constraint can be written as

$$\mathcal{R} + K^2 - K_{\mu\nu}K^{\mu\nu} - 2K\frac{\dot{\phi}}{\phi} - \frac{2}{\phi}D^2\phi - \frac{\omega}{\phi^2}\dot{\phi}^2 - \frac{\omega}{\phi^2}D_\mu\phi\, D^\mu\phi = 0\,, \quad (7.6)$$

where $\dot{} = n^\mu\nabla_\mu$ and $D^2 = D_\mu D^\mu$.

Similarly, for the momentum constraint we have

$$\begin{aligned}
&D_\mu K_\nu^\mu - D_\nu K\\
=&\frac{\Box\phi}{\phi}h_\nu{}^\mu n_\mu + \frac{\omega}{2}\frac{(\nabla\phi)^2}{\phi^2}h_\nu{}^\mu n_\mu - \frac{\omega}{\phi^2}h_\nu{}^\mu n^\rho\nabla_\mu\phi\,\nabla_\rho\phi - \frac{1}{\phi}h_\nu{}^\mu n^\rho\nabla_\mu\nabla_\rho\phi\,.
\end{aligned} \quad (7.7)$$

The first and second terms on the right-hand side of this equation can immediately be seen to vanish, as $h_\nu^{\ \mu} n_\mu = 0$. The third term is simply $-\omega\dot{\phi} D_\nu\phi/\phi^2$. Finally the last term can be written as

$$\begin{aligned} -\frac{1}{\phi} h_\nu^{\ \mu} n^\rho \nabla_\mu \nabla_\rho \phi &= -\frac{1}{\phi} h_\nu^{\ \mu} \nabla_\mu (n^\rho \nabla_\rho \phi) + \frac{1}{\phi} h_\nu^{\ \mu} (\nabla_\mu n^\rho) \nabla_\rho \phi \\ &= -\frac{1}{\phi} D_\nu \dot{\phi} - \frac{1}{\phi} K_\nu^{\ \rho} \nabla_\rho \phi \,. \end{aligned} \tag{7.8}$$

Combining these results we have that the momentum constraint can be written as

$$D_\mu K^\mu_{\ \nu} - D_\nu K + \frac{1}{\phi} K_\nu^{\ \mu} D_\mu \phi + \frac{1}{\phi} D_\nu \dot{\phi} + \frac{\omega}{\phi^2} \dot{\phi} D_\nu \phi = 0 \,. \tag{7.9}$$

Equations (7.6) and (7.9) are the final version of the Hamiltonian and momentum constraint equations we wish to use and are consistent with other similar results derived in the literature [179].

Finally, we wish to write the scalar field Equation (2.14) as a set of constraint and evolution equations. For convenience this is done by introducing new variables $\pi \equiv \dot{\phi}$ and $\psi_\mu \equiv D_\mu \phi$. The set of evolution equations for ϕ, π and ψ_μ are then given in vacuum by

$$\begin{aligned} \dot{\phi} &= \pi, \\ \dot{\pi} &= D_\mu \psi^\mu + K\pi + \dot{n}^\mu \psi_\mu, \\ \dot{\psi}_\mu &= D_\mu \pi + \dot{n}_\mu \pi + n_\mu \dot{n}^\nu \psi_\nu + K_\mu^{\ \nu} \psi_\nu, \end{aligned} \tag{7.10}$$

with the only constraint being

$$\psi_\mu - D_\mu \phi = 0 \,. \tag{7.11}$$

This last equation is of course just the definition of the variable ψ_μ, and must therefore be satisfied identically. We note that these equations are the same as those considered in [155], for a minimally coupled scalar field in Einstein's theory[1].

The only equations that need to be satisfied in order to fully specify the initial data of a vacuum spacetime in this theory are therefore just Equations (7.6) and (7.9). In the next section of this paper we will solve these equations in order to find initial data for a universe filled with point-like masses.

[1] Except for a missing term $+K_\mu^{\ \nu}\psi_\nu$, on the right-hand side of Equation (13) of that paper.

7.3 Initial Data

In order to simplify the constraint equations we can choose the extrinsic curvature to vanish, such that $K_{ij} = 0$. A hypersurface that satisfies this condition is time-symmetric, as we have seen before, and in a cosmological context corresponds to a maximum of expansion. It also provides an analogous situation to the general relativistic studies that have already been performed for this situation. In this case the Hamiltonian and momentum constraint equations then become

$$\mathcal{R} - \frac{2}{\phi} D^2\phi - \frac{\omega}{\phi^2}\dot{\phi}^2 - \frac{\omega}{\phi^2} D_i\phi D^i\phi = 0\,, \tag{7.12}$$

and

$$\frac{1}{\phi} D_i\dot{\phi} + \frac{\omega}{\phi^2}\dot{\phi} D_i\phi = 0\,, \tag{7.13}$$

and where we are now using Latin indices to denote coordinates on the 3-dimensional initial hypersurface, such that D_i is a covariant derivative with respect to the metric h_{ij} of this space.

Equation (7.13) is satisfied if either $\dot{\phi} = 0$ or $\dot{\phi} \propto \phi^{-\omega}$. The former of these corresponds to a scalar field that is also time-symmetric at the initial hypersurface. The latter case is not time-symmetric, and offers a potentially interesting scenario to study, but in this case we are unable to find solutions to the corresponding Hamiltonian equation. We therefore restrict our attention to the $\dot{\phi} = 0$ case, for which the Hamiltonian constraint (7.12) becomes

$$\mathcal{R} = (\omega + 2)\tilde{\psi}_i\tilde{\psi}^i + 2D_i\tilde{\psi}^i\,, \tag{7.14}$$

where we have defined $\tilde{\psi}_i \equiv \psi_i/\phi = D_i\phi/\phi$. This single equation is a profound simplification of the initial system of constraint equations, but is still a non-linear differential equation for the variable $\tilde{\psi}$ in terms of the 3-curvature $\mathcal{R}$. We will now show that through a change of variables we can express this as a set of linear equations which therefore admit solutions that can be linearly superposed.

Suppose that the geometry of an initial hypersurface can be written as

$$ds^2 = \Omega^4(r, \theta, \varphi)\, d\tilde{s}_3^2 \tag{7.15}$$

where $d\tilde{s}_3^2 = dr^2 + \sin^2 r(d\theta^2 + \sin^2\theta d\varphi^2)$ is the line-element of a hypersphere, and r, θ and φ are hyperspherical polar coordinates. The change of variables we wish to

perform is then given by

$$\Omega \;= \chi^a \sigma^{1-a} \qquad \text{and} \qquad \phi = \chi^s \sigma^{-s}\,, \tag{7.16}$$

where a is a constant, $s = (1 - 2a \pm \tau)/(2 + \omega)$ and $\tau = \sqrt{1 + 4a(1-a)(3+2\omega)}$. In this case Equation (7.14) is satisfied by any solutions of the following two linear equations,

$$\tilde{D}^2\sigma = \kappa_1\,\sigma \tag{7.17}$$

$$\tilde{D}^2\chi = \kappa_2\,\chi\,, \tag{7.18}$$

where $\tilde{D}^2$ is the Laplacian operator on the conformal hypersphere described by $d\tilde{s}^2$, and κ_1 and κ_2 are constants. If we choose $s = (1 - 2a - \tau)/(2 + \omega)$, then κ_1 satisfies

$$\kappa_1 = \frac{3(2+\omega) - (1 + 2a(3+2\omega) - \tau)\kappa_2}{(7 + 4\omega - 2a(3+2\omega) + \tau)}\,. \tag{7.19}$$

If one were to choose $s = (1 - 2a + \tau)/(2 + \omega)$, then the sign of τ would need to also be changed in this expression. However, in what follows we will use the first choice of s (this will be explained when we compare our solution to known exact solutions).

Equations (7.17) and (7.18) are both Helmholtz equations, which have the following smooth solutions [155]:

$$\sigma(r,\theta,\varphi) = \sum_i^N \alpha_i \,\frac{\sin\{\sqrt{1-\kappa_1}(\pi - r_i)\}}{\sin\{\sqrt{1-\kappa_1}\,\pi\}\sin\{r_i\}}, \tag{7.20}$$

$$\chi(r,\theta,\varphi) = \sum_i^N \gamma_i \,\frac{\sin\{\sqrt{1-\kappa_2}(\pi - r_i)\}}{\sin\{\sqrt{1-\kappa_2}\,\pi\}\sin\{r_i\}}, \tag{7.21}$$

where α_i and γ_i are two sets of constants, which are explained further on. Each of the terms in each of these two sums can be seen to diverge at $r_i = 0$, and remain smooth and single valued everywhere else. Both σ and χ therefore contain N poles, which we take to be located at N distinct locations on the conformal hypersphere. The meaning of r_i, as used in each of the different terms in these two equations, should therefore be taken to mean the value of the r coordinate after rotating coordinates so that the pole for that particular term appears at $r = 0$. In this sense, we are using a different set of hyperspherical polar coordinates for each term, so that we can write every term in the same form.

7.3.1 Comparison with the Brans Solution

The solutions given in Equations (7.20) and (7.21) contain $2N+3$ free parameters: $\alpha_i, \gamma_i, \omega, \kappa_2$ and a. We wish to understand these degrees of freedom and make sense of this, so we will compare our solution with the spherically symmetric, vacuum Brans solution. The line-element for the Brans solution is given by [46]

$$ds^2 = -e^{2\alpha_0}\left(\frac{1-\frac{B}{r}}{1+\frac{B}{r}}\right)^{\frac{2}{\lambda}} dt^2 + e^{2\beta_0}\left(1+\frac{B}{r}\right)^4 \left(\frac{1-\frac{B}{r}}{1+\frac{B}{r}}\right)^{\frac{2(\lambda-c-1)}{\lambda}} d\tilde{s}^2, \tag{7.22}$$

where $d\tilde{s}^2 = dr^2 + r^2(d\theta^2 + \sin^2\theta d\varphi^2)$, $\lambda^2 \equiv (c+1)^2 - c(1-\omega\, c/2)$ and c, B, α_0 and β_0 are constants. This solution also has a scalar field ϕ which can be written as

$$\phi = \phi_0 \left(\frac{1-\frac{B}{r}}{1+\frac{B}{r}}\right)^{\frac{c}{\lambda}}, \tag{7.23}$$

where again ϕ_0 is another constant. By comparing this solution with Equations (7.15) and (7.16) and requiring that $s = (1-2a-\tau)/(2+\omega)$, the following identification can be made:

$$s = \frac{c}{\lambda} \qquad \text{and} \qquad a = \frac{\lambda - c - 1}{2\lambda}. \tag{7.24}$$

For the choice of $s = (1-2a+\tau)/(2+\omega)$, our solution satisfies the constraint equations if we identify s with $-c/\lambda$ and a with $1-(\lambda-c-1)/\lambda$. This shows that the choice in the sign of τ in the parameter s is degenerate with the identification of χ and σ with either $\left(1-\frac{B}{r}\right)$ or $\left(1+\frac{B}{r}\right)$.

It is known that if $c = -1/(2+\omega)$, then Equation (7.22) reduces to the Schwarzschild solution as $\omega \to \infty$ [52]. Making this choice for c then gives us

$$s = -\frac{\sqrt{2}}{\sqrt{2+\omega}\sqrt{3+2\omega}} \qquad \text{and} \qquad a = \frac{1}{2} - \frac{1+\omega}{\sqrt{2}\sqrt{2+\omega}\sqrt{3+2\omega}}, \tag{7.25}$$

as well as

$$\kappa_1 = \frac{3 - 2\kappa_2 + \kappa_2\sqrt{\frac{6+4\omega}{2+\omega}}}{2+\sqrt{\frac{6+4\omega}{2+\omega}}}, \tag{7.26}$$

where $s = a = 0$ and $\kappa_1 = 3/4$ in the limit $\omega \to \infty$. This reduces the number of free parameters in our solutions to $2(N+1)$: $\alpha_i, \gamma_i, \omega$ and κ_2. We will investigate further the meaning of these remaining degrees of freedom in what follows.

7.4 Proper Mass and Scalar Charge

Proper Mass

We proceed as in the previous chapters of this thesis, in that in order to determine the proper mass of each of the point-like objects in our solution, we need to view them from infinity in the asymptotically flat region on the far side of the Einstein-Rosen bridge. Taking this limit $r_i \to 0$ gives

$$ds^2 \to \left(\frac{\gamma_i}{r_i} + B_i\right)^{4a} \left(\frac{\alpha_i}{r_i} + A_i\right)^{4-4a} d\tilde{s}^2, \tag{7.27}$$

where

$$A_i = -\frac{\alpha_i\sqrt{1-\kappa_1}}{\tan\{\sqrt{1-\kappa_1}\pi\}} + \sum_{j\neq i} \alpha_j \frac{\sin\{\sqrt{1-\kappa_1}(\pi - r_{ij})\}}{\sin\{\sqrt{1-\kappa_1}\pi\}\sin\{r_{ij}\}}, \tag{7.28}$$

$$B_i = -\frac{\gamma_i\sqrt{1-\kappa_2}}{\tan\{\sqrt{1-\kappa_2}\pi\}} + \sum_{j\neq i} \gamma_j \frac{\sin\{\sqrt{1-\kappa_2}(\pi - r_{ij})\}}{\sin\{\sqrt{1-\kappa_2}\pi\}\sin\{r_{ij}\}}, \tag{7.29}$$

where r_{ij} is the coordinate distance between points i and j (after rotating so that mass i appears at $r = 0$). We have also used the fact that in the limit $r_i \to 0$, then $d\tilde{s}_3^2 \to d\tilde{s}^2$ as $\sin^2 r \to r^2$. Defining a new coordinate $r_i' \equiv \alpha_i^{2-2a}\gamma_i^{2a}/r_i$ means that in the limit $r_i \to 0$ then $r_i' \to \infty$. Inserting this into Equation (7.27) gives

$$ds^2 \to \left(1 + 4\frac{(1-a)\alpha_i^{1-2a}\gamma_i^{2a}A_i + a\alpha_i^{2-2a}\gamma_i^{2a-1}B_i}{r_i'}\right) d\tilde{s}'^2, \tag{7.30}$$

where $d\tilde{s}'^2 = dr_i'^2 + r_i'^2 d\Omega^2$. Similarly, in the limit $r \to \infty$ the static, spherically symmetric Brans solution in Equation (7.22) becomes

$$ds^2 \to e^{2\beta_0}\left(1 + 4\frac{(c+1)}{\lambda}\frac{B}{r}\right) d\tilde{s}^2. \tag{7.31}$$

which, up to an overall constant rescaling of units, can be compared to Equation (7.30) to give $B(c+1)/\lambda = (1-a)\alpha_i^{1-2a}\gamma_i^{2a}A_i + a\alpha_i^{2-2a}\gamma_i^{2a-1}B_i$. We now recall that the parameter B in the Brans solution is related to its mass m by $B = m\lambda/2$ [52]. Further recalling $c = -1/(2+\omega)$ means we can now read off an expression for the proper mass of each of the point masses in our solution,

$$m_i = 2\left(\frac{2+\omega}{1+\omega}\right)\left(\frac{\gamma_i}{\alpha_i}\right)^{2a-1}((1-a)\gamma_i A_i + a\alpha_i B_i)\ . \tag{7.32}$$

Scalar Charge

As well as mass we can also derive an expression for the scalar charge, q_i, of each of the objects in our solution. This method will be analogous to the one used to derive an expression for the electric charge of a point mass in section 6.3, in particular, Equation (6.21). We therefore define our scalar charge as

$$q_i \equiv \frac{1}{4\pi} \int \partial_i \phi n^i dA \,, \tag{7.33}$$

where n^i is the unit inward pointing normal and dA is an area element as $r \to 0$, such that $n^i = (-\sigma^{-2+2a}\chi^{-2a}, 0, 0)$ and $dA = \sigma^{4-4a}\chi^{4a} r^2 \sin\theta \, d\theta \, d\phi$. As for the proper mass, we evaluate σ and χ in the asymptotic limit $r \to 0$. This gives an expression for the scalar charge of the i^{th} mass as

$$q_i = s \left(\frac{\gamma_i}{\alpha_i} \right)^{s+2a-1} (\gamma_i A_i - \alpha_i B_i) \,, \tag{7.34}$$

which has a pleasing symmetry with the expression for the proper masses given in Equation (7.32). It is straightforward to verify that in the limit $\omega \to \infty$, we recover $q_i \to 0$ as expected. These results show that the proper mass m_i and scalar charge q_i of each mass are directly related to the values of the parameters α_i and γ_i, and that by specifying a value of m_i and q_i for each of our points we are essentially setting the values of α_i and γ_i. This leaves only the values of ω and κ_2 as the remaining two degrees of freedom. The former of these corresponds to a choice of the gravitational theory being considered, as it appears as a coupling constant in the generating Lagrangian. We interpret the latter as corresponding to the amount of scalar field in the background cosmology, as explained below.

7.4.1 Background Scalar Field

We choose to depict the conformal factor Ω and scalar field ϕ for the 8-mass cubic lattice, as already introduced in the previous chapters. Figures 7.1 to 7.4 depict these quantities for different choices of the parameter κ_2. In each of these diagrams have set $\omega = \alpha = \gamma = 1$, and taken a surface at $r = \pi/2$. The slice taken through this configuration in these figures is a great sphere, and is chosen so that six of the eight points are positioned within that sphere. In each of the figures, the distance of the surface from the centre is the value of the field (Ω or ϕ) at that point, whilst the angular positions of the surfaces correspond to individual points on the great sphere $r = \pi/2$.

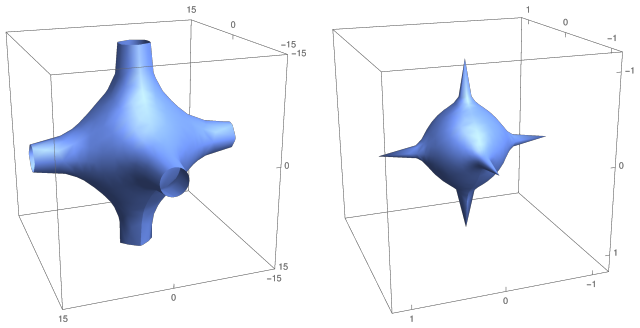

Figure 7.1: Conformal factor Ω (left) and scalar field ϕ (right), for $\kappa_2 = 0.1$.

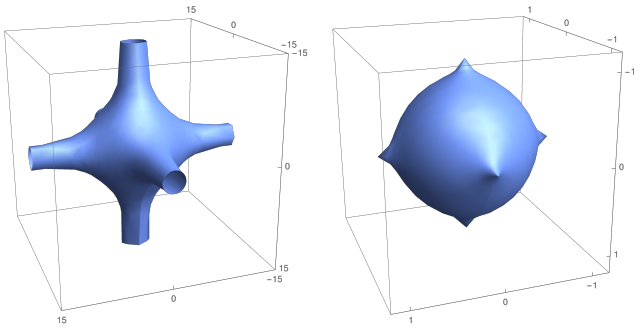

Figure 7.2: Conformal factor Ω (left) and scalar field ϕ (right), for $\kappa_2 = 0.4$.

In Figure 3, for $\kappa_2 = 0.75$ there is no scalar charge on any of the masses, as the value of the scalar field is represented by a constant unit sphere. Mathematically this can be seen in Equation (7.26), where we have that $\kappa_1 = \kappa_2$ for $\kappa_2 = 0.75$. Setting all of the α_i parameters to be equal to each other, and likewise for γ_i, then implies from Equations (7.28) and (7.29) that $\gamma_i A_i = \alpha_i B_i$. Finally it is manifest from Equation (7.34) that $q_i = 0$.

For values of $\kappa_2 < 0.75$ the scalar field is largest at the positions of the masses at a maximum value of 1, whereas for $\kappa_2 > 0.75$ the scalar field is smallest at the positions of the masses (as shown by the dimples in Figure 7.4). Changing the value of κ_2 can therefore be interpreted as increasing or decreasing the background value of the scalar field. We note that changing the value of κ_2 has very little effect on the geometry of the initial hypersurface itself, but that changing ω has a very significant effect on the scalar field distribution, with the shape of the corresponding figures again approaching a spherical shape in the limit $\omega \to \infty$. The distribution of ϕ in Figures 7.1 to 7.4 can be directly linked to the distribution of Newton's constant, G, via Equation (2.15).

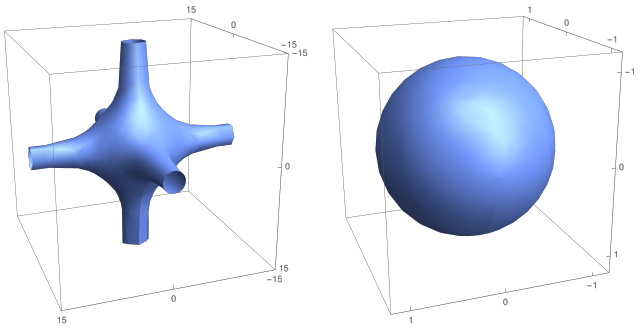

Figure 7.3: Conformal factor Ω (left) and scalar field ϕ (right), for $\kappa_2 = 0.75$.

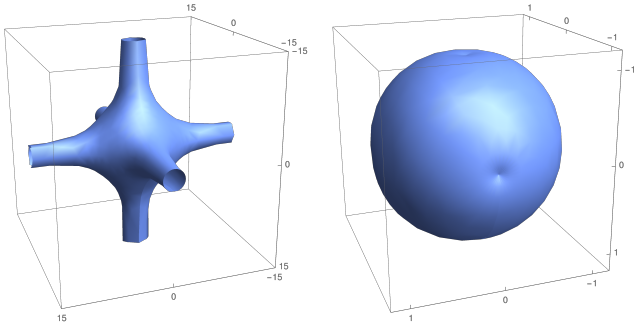

Figure 7.4: Conformal factor Ω (left) and scalar field ϕ (right), for $\kappa_2 = 0.9$.

7.4.2 General Relativistic Limit

We wish to investigate how (and if) the lattice cosmologies constructed above differ from their general relativistic counterparts, and how they approach them in the limit $\omega \to \infty$. Of principle interest in this regard will be the scale of the cosmological region of each of the respective solutions. In order to extract this quantity we define $a_0^{\mathrm{BDL}} \equiv (\chi^{2a}\sigma^{2-2a})\,|_{\mathrm{vertex}}$, where the right-hand side is being evaluated at the vertex of one of the primitive cells from which the lattice is constructed (i.e. at one of the points which is furthest away from all nearby masses). A similar quantity, a_0^{GRL} has already been calculated to measure the scale of the cosmological region in the corresponding general relativistic lattice [3].

We now wish to compare the values of a_0^{BDL} and a_0^{GRL} for two lattices that contain the same number of objects, located at the same positions, and with the same total proper mass. We again choose to consider the 8-mass cubic lattice, as discussed in the previous section. We find that the quantity $a_0^{\mathrm{BDL}}/a_0^{\mathrm{GRL}}$ changes as a function of the coupling parameter of the theory, ω, but also as a function of parameter that controls the background value of the scalar field κ_2, where $\kappa_2 \geq 1$. In order to uniquely specify a solution in the case of the Brans-Dicke lattices we also need to specify a value for the proper mass and scalar charge of each black hole, $q_i = q$. Regarding the proper

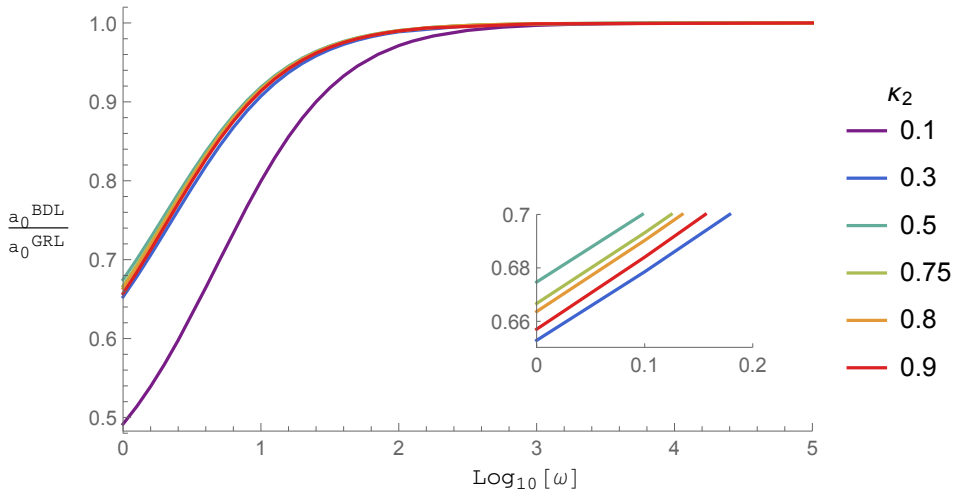

Figure 7.5: Ratio of scale factors $a_0^{\mathrm{BDL}}/a_0^{\mathrm{GRL}}$ for the BD and GR lattice cosmologies, for different values of ω and κ_2 (with $m = 9.48$ and $\gamma = 1$). The inset shows a close-up of the intersection of the lines with $\kappa_2 \geq 0.3$ and the y-axis.

mass, we set this to be the value found in the general relativistic case, as shown in Table VI of [3]. There, the ratio of effective mass to proper mass was found to be 0.11. Setting the effective mass to unity, for simplicity, then yields $m_i = m = 9.48$, and here we take this to set the value of the α_i parameters. For the scalar charge q, we find that scale factor of the cosmology is insensitive to the specific value chosen for q, therefore we can instead set $\gamma_i = 1$ for simplicity. We display our results in Figure 7.5

All our results show a convergence towards the general relativistic value of the scale factor as $\omega \to \infty$, as expected. For $\omega \lesssim 10^3$, however, our solutions are very different from the general relativistic ones, with the scale factor taking a smaller value in every case. These plots make it clear that scale of the cosmological solutions is strongly dependent on κ_2 for small values of ω, but that in the limit $\omega \to \infty$ all dependence on κ_2 drops out. Finally we interpret the independence of the value of the scale factor to the particular value of q as demonstrating that the majority of the gravitational influence of each point particle is dominated by its mass, and not its scalar charge.

7.5 Brans-Dicke Friedmann Cosmology

In this section we wish to make a comparison between the initial data for an inhomogeneous universe described above, and the corresponding homogeneous and

isotropic dust-filled Friedmann cosmologies that exist in Brans-Dicke theory. Our approach to this will be to compare cosmologies that contain the same total mass and background scalar field value, at a moment of time-reversal symmetry, similarly to previous chapters.

To do this we need to solve the field equations for homogeneous and isotropic dust-filled spacetimes, which are given by

$$\begin{aligned} H^2 &= \frac{8\pi\rho}{3\phi} - \frac{k}{a^2} - H\frac{\dot{\phi}}{\phi} + \frac{\omega}{6}\frac{\dot{\phi}^2}{\phi^2}, \\ \frac{\ddot{\phi}}{\phi} &= \frac{8\pi\rho}{\phi(2\omega+3)} - 3H\frac{\dot{\phi}}{\phi}, \end{aligned} \tag{7.35}$$

where $\rho = \rho_0 a_0^3/a^3$, $H = \dot{a}/a$ and where over-dots denote differentiation with respect to the proper time of comoving observers.

We immediately note that if we require $H = \dot{\phi} = 0$ then Equation (7.35) implies that the spatial curvature k must be positive (and given by $k = 8\pi\rho a^2/3\phi$, assuming ρ and ϕ are both positive valued quantities). Choosing units where $k = 1$, we find that there exist solutions given by [180]

$$a(t) = \frac{3\phi_0}{8\pi\rho_0 a_0^3} - \frac{2\pi\rho_0 a_0^3}{\phi_0(3+2\omega)}(t-t_0)^2\,, \tag{7.36}$$

where ϕ_0 and t_0 are constants, and where $\phi = \phi_0 a^{-2}$. This clearly corresponds to a universe with a time-symmetric evolution, with a maximum of expansion at $t = t_0$. The intrinsic geometry of the hypersurface at maximum of expansion is therefore given by

$$ds^2 = \frac{9\phi_0^2}{64\pi^2\rho_0^2 a_0^6} d\tilde{s}^2 = \frac{9\pi^2\phi_0^2}{16M^2} d\tilde{s}^2\,, \tag{7.37}$$

where in the last equality we have used the fact that $\rho = M/V = M/2\pi^2 a^3$, and where M and V are the mass and spatial volume of the hypersphere. This gives us the scale of the maximum of expansion of such a universe in terms of the total mass of the matter content M, and the constant associated with the scalar field, ϕ_0.

In order to compare cosmologies with the same total mass, we choose to consider solutions in which $M = Nm$, where N is the total number of identical point-like masses in the inhomogeneous solution and m is the proper mass of each of them. The second condition we need to implement is on the value of ϕ_0. To do this, we require that the background value of the scalar field in the inhomogeneous solutions must equal that of the Friedmann cosmology. Using the fact that the scalar field in the inhomogeneous solutions is given by $\phi = \chi^s \sigma^{-s}$, and equating it to the value of

ϕ at the maximum of expansion of the Friedmann models, we find

$$\chi^s\sigma^{-s} = \frac{16M^2}{9\pi^2\phi_0} \qquad \Rightarrow \qquad \phi_0 = \frac{16M^2}{9\pi^2\chi^s\sigma^{-s}}\,, \tag{7.38}$$

where χ and σ are to be given values associated with the cosmological background. There is clearly some freedom in choosing how this should be done, as both quantities are in general non-constant functions of spatial position. Here we proceed as in the previous section and choose the location that is farthest from all masses, at the vertex of one of the primitive cells of the lattice, analogous to definition D1, Equation (3.17) in chapter 3. This is is the closest thing to taking a 'background value' in an inhomogeneous cosmology. We will also evaluate the scale factor in the inhomogeneous solutions at the same point in order to make a fair comparison.

7.5.1 Multi-level Comparisons

We can now write the scale factors for Brans-Dicke lattice (BDL) cosmologies, and the corresponding Brans-Dicke Friedmann (BDF) cosmologies, as

$$a_0^{\mathrm{BDL}} = \chi^{2a}\sigma^{2-2a} \qquad \text{and} \qquad a_0^{\mathrm{BDF}} = \frac{4Nm}{3\pi\chi^s\sigma^{-s}}\,, \tag{7.39}$$

where χ and σ are both to be evaluated at the locations farthest from all masses. A comparison of a_0^{BDL} and a_0^{BDF} will then give a numerical quantification for the effects of structurisation of matter in Brans-Dicke cosmologies.

From the analyses in the previous two sections, we can illustrate the various comparisons that we can now perform. This is show in Figure 7.6. The branch labelled "1" corresponds to the comparison between discrete and continuous cosmologies in the general relativistic case, as initiated in [3] and reviewed in [129]. The work in section 7.4.2 provides the first (and currently only) steps to understand branch "2" of this diagram. We will investigate the remaining two branches in the remainder of this chapter.

Comparison of Friedmann Cosmologies

For branch "3", we again choose to consider the 8-mass model discussed above, and again choose the proper mass of each of our sources to have $m_i = m = 9.48$ (so that the total mass in the corresponding Friedmann solution is $M = 75.84$). We also set the parameter γ_i from Equation (7.21) to be equal to $\gamma = 1$ for each particle. Under these conditions, we plot the ratio of scales in the Friedmann cosmologies for the

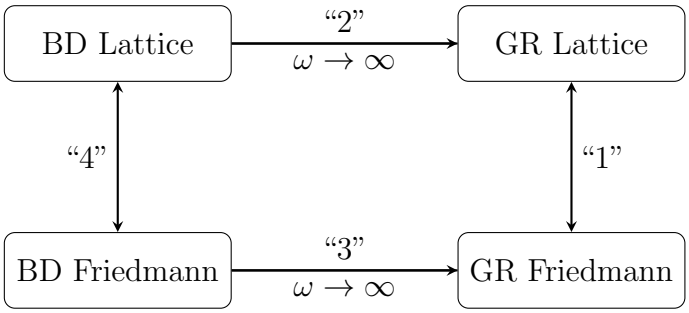

Figure 7.6: Schematic diagram showing four different cosmologies, and the comparisons that are possible between them.

Brans-Dicke theory and general relativistic case in Figure 7.7. The value of a_0^{BDF} approaches the general relativistic value as $\omega \to \infty$, as expected, and similarly to Figure 7.5. For small ω the scale of the Brans-Dicke Friedmannian cosmology is much larger than its general relativistic counterpart, which contrasts the behaviour in the previous graph.

Comparison of Brans-Dicke Cosmologies

Finally for branch "4", we plot the ratio of scales in the lattice and Friedmann cosmologies in the Brans-Dicke theory in Figure 7.8, using the exact same conditions as previously. The value of $a_0^{\mathrm{BDL}}/a_0^{\mathrm{BDF}}$ for the 8-mass lattice can be clearly seen to approach the general relativistic value of 1.236 calculated in [3], as $\omega \to \infty$. For small ω, on the other hand, the scale of the lattice cosmology is much smaller than its Friedmann counterpart, by as much as 50% for $\kappa_2 = 0.1$. It is interesting that there are small values of ω where the theory is far from a general relativistic one (for example, $\omega = 10, \kappa_2 = 0.1$) but the process of constructing either a lattice cosmology or a fluid one makes no difference as far as the ratio of scale factors is concerned (for these values it is approximately 1). If these are viable theories of gravity, we can construct cosmologies where there is no backreaction, however we note that the Brans-Dicke coupling parameter is very well constrained to be $\omega \gtrapprox 40,000$ to 2σ from solar system tests [181]. Our global scale of our models show rapid convergence to their general relativistic counterparts for values of ω this large, and should therefore should not be expected to give any detectable difference on very large scales if the governing theory is to be compatible with solar system constraints. Nevertheless, in such cases the scalar field can still vary considerably in the vicinity of the masses themselves, and may also give potential deviations from general relativity in their future evolution, as more extreme environments are encountered. Theory

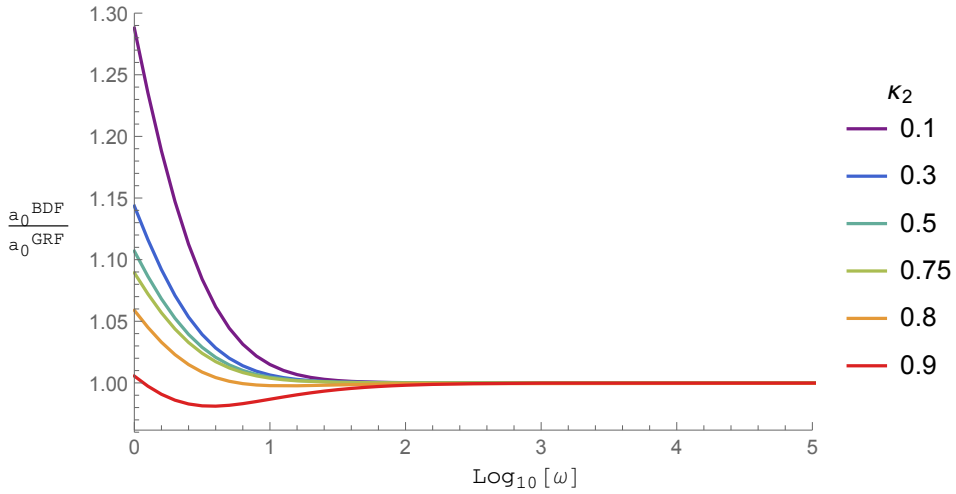

Figure 7.7: Ratio of scales of BD to GR Friedmann cosmologies for $m = 9.48$ and $\gamma = 1$.

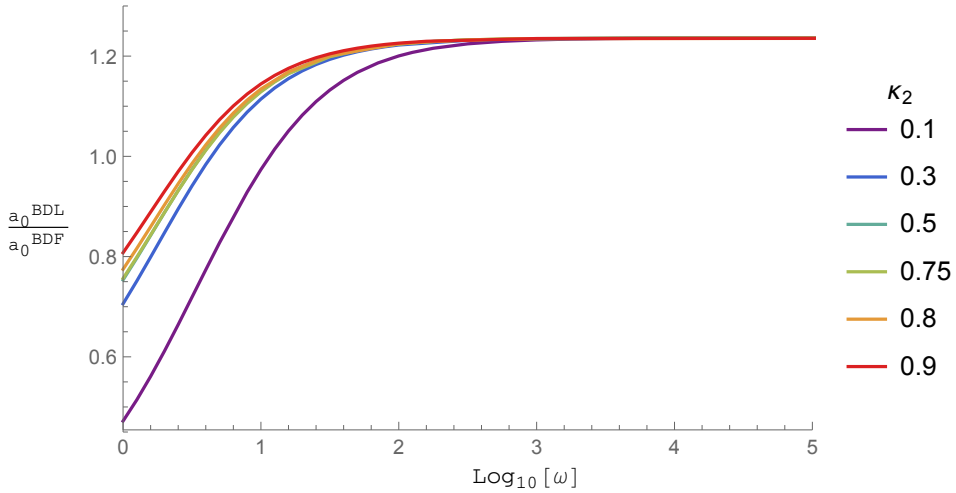

Figure 7.8: The ratio of scales, $a_0^{\text{BDL}}/a_0^{\text{BDF}}$, for Brans-Dicke Lattice and Friedmann cosmologies (with $m = 9.48$ and $\gamma = 1$).

independent variations on the Newton's constant can also be used to constrain these models [58, 59]. Such constraints tend to be imposed on the time variation of G, and are found from a number of different observations to be constrained at the level $\dot{G}/G \lesssim 10^{-12}$ per year. Numerical evolution of our initial data would allow us to investigate the behaviours that are compatible with these bounds, but this will be left for future studies.

7.6 Discussion

In this final chapter we have provided, for the first time, exact initial data for a cosmological model in a scalar-tensor theory of gravity that contains a regular array of point-like particles. This was achieved by first deriving the relevant constraint equations (in section 7.2), and then by imposing the condition that the extrinsic curvature vanishes on the initial hypersurface. We found a simple set of solutions to these constraint equations, in terms of a pair of conformal factors, which reduces in the appropriate limits to the known static, spherically symmetric vacuum Brans solution. Comparison to this exact solution then allowed us to derive expressions for the proper mass and scalar charge for each of the particles in our cosmologies. We found that the scalar charge of each of the black holes vanishes in the general relativistic limit, when $\omega \to \infty$, and that the spatial variation of Newton's constant depended on both the scalar charge of the individual bodies as well as a cosmological background value.

We considered both the general relativistic limit of a specific realisation of our lattice solutions, as well as a comparison between comparable discrete and continuous cosmological solutions in Brans-Dicke theory. In both cases it was found that our new solutions approached the expected limits as $\omega \to \infty$, and that order one deviations from the general relativistic results were possible when ω was small. In these latter cases the solutions were also found to be sensitive to the value of the parameter κ_2, which controls the background value of the scalar field.

8 Conclusions and Future Work

The black hole lattices in [3] were generalised and extended to include new phenomena, motivated by their use as inhomogeneous cosmological models. The lattices are constructed from a superposition of Schwarzschild masses, tessellating a 3-sphere. This choice of hypersurface solves the time-symmetric constraint equations of general relativity and therefore is an exact solution to the Einstein field equations, including all relativistic effects. The first generalisation was to include the effects of structuration. This was doing by splitting the masses up and moving them along well-defined paramaterised trajectories, where we could control the extent of clustering. The next generalisations involved the addition of extra fields, specifically a cosmological constant Λ and electric charge. Our final generalisation involved moving away from general relativity to consider the lattices in the context of a scalar-tensor theory of gravity - Brans-Dicke theory. This involved deriving the constraint equations and solving them with a suitable choice of initial data. In each of our generalisations we compared the lattices to their FLRW counterparts, and where appropriate, calculated interaction energies, proper masses, scalar charges, deceleration parameters, and the location of apparent horizons.

8.1 Summary of Key Findings

We summarise the key findings of this thesis below:

- Backreaction is found to decrease when either one of the following happens:
  - The number of masses in the black hole lattices increases regardless of the setting.
  - For structuration, when interaction energies between clustered masses are taken into account.
  - For charge, when the black holes are extremal.
  - For a cosmological constant, when the value of Λ is large ($\sim 100 M_T^{-2}$).

    - For Brans-Dicke gravity, when certain combinations of the coupling parameter ω and the scalar field background κ_2 are used ($\omega = 10, \kappa_2 = 0.1$).

- In the lattices with structuration, for black holes very close together, an extra apparent horizon appears, which gets smaller as the number of masses is increased. This horizon cannot be approximated by a spherical surface.

- This horizon appears for a certain critical value of the parameter λ. Within this, we can treat it as an effective n-mass model, where n is one of the 6 original black hole lattices.

- When interaction energies are not taken into account, the size of the lattice cosmology can be approximately 30% of its Friedmann counterpart.

- In the lattices with Λ, for a constant mean curvature slice through Schwarzschild-de Sitter, the intrinsic geometry of the hypersurface is the same as a time-symmetric slice through Schwarzschild.

- For some combinations of the number of masses and value of the cosmological constant Λ, the ratio of lattice to FLRW deceleration parameters can be less than zero.

- Inner and outer horizons can exist, in expanding or contracting hypersurfaces. The location of these are given by Equation (5.18), with extremal values for which this is satisfied tending to the Schwarzschild-de Sitter value as the number of masses increases.

- In the lattices with charge, antipodal black holes have the same mass but opposite charge.

- The apparent horizons disappear as the black holes become more extremal.

- Finally, in the lattices in Brans-Dicke gravity, a suitable time-symmetric ansatz for the hypersurface can solve the derived constraint equations.

- A new parameter κ_2 can be interpreted as the amount of background scalar field in the background cosmology.

- The appropriate general relativity values are recovered in the limit $\omega \to \infty$.

8.2 Future Work

As shown in this thesis, the original black hole lattices enjoy many extensions and generalisations, which are certainly not limited to what we have presented here. There are many ways in which they can be extended, some of which we will discuss here.

The first is a follow on from chapter 4, where we constructed a two-level hierarchy of structures - the individual masses themselves, and the clustered black hole mass. The Universe we observe contains many hierarchical levels of structure, see Equation (2.107), so an appropriate avenue of exploration would be to split the masses up again and perform a similar process, adding in an extra level of structuration. This would allow for a deeper understanding of the role of interaction energies, and shed light on whether they combine over many scales to alter the scale of the cosmology. Furthermore, when we considered the interaction energies between masses, we only took into account pairwise interactions. Further study could include a numerical analysis of many-body interaction energies between all masses inside a cluster, again to fully investigate the role of the interaction energies.

The lattices we considered were inhomogeneous, but isotropic. The cosmological principle states that the Universe is homogeneous and isotropic on large scales, therefore the latter of these could be relaxed in our cosmological models, meaning we would compare our lattices to Bianchi solutions. There are many of these, and can be classified according to their isometries. The simplest way of proceeding for our lattices would be to remove some of the black holes, to create a degree of anisotropy, and calculate the effects this has on the scales of the cosmologies.

Much progress regarding backreaction has been the use of the Buchert averaging scheme, introduced in section 2.4. It was used in [182] where the authors considered a perturbed Einstein-de Sitter model with periodic dust overdensities. This averaging scheme is not applicable to our black hole lattices, as the spatial volume of a domain containing a mass would be infinite. A way to circumvent this would be to construct an LTB version of the lattices, and smooth out the mass of the black holes into some region, whilst still keeping a degree of inhomogeneity. This would then allow the Buchert averaging scheme to used, and informative comparison between other approaches such as the one discussed above.

Finally, we note that the growing field of numerical cosmological can answer a lot of questions about backreaction that toy models cannot, due to their reliance on symmetries and highly idealised matter distributions. The models with a cosmological constant form a starting point for full numerical evolution, in that we showed a

criteria for eternal expansion based on the density parameters, Equation (5.28). Originally, the time evolution involves evolving towards a singularity. The addition of Λ prevents this and allows for the evolution of backreaction to be calculated.

Calculating the time evolution of the initial data allows for the propagation of light and therefore observables to be investigated, as we have seen in section 2.4.4. Although this was done in [149], the initial data was constructed numerically, and they found oscillations in the redshift due to tensor modes from the initial data construction. This arises from a lack of an asymptotically flat region, as there is no domain for the gravitational waves to escape to. Starting from an exact solution and then numerically evolving may reduce the noise from these modes if evolved, which our data may be capable of. The optical properties in the models with Λ would also be worthwhile to pursue, as these models expand eternally and do not collapse. Both of these would allow for further conclusions to be drawn about the effect of inhomogeneities on the propagation of light.

Bibliography

[1] T. W. Baumgarte and S. L. Shapiro, *Numerical Relativity: Solving Einstein's Equations on the Computer*. Cambridge University Press, New York, USA, 2010, 10.1017/CBO9781139193344.

[2] T. Clifton, D. Gregoris and K. Rosquist, *Piecewise Silence in Discrete Cosmological Models*, *Class. Quant. Grav.* **31** (2014) 105012 [1402.3201].

[3] T. Clifton, K. Rosquist and R. Tavakol, *An exact quantification of backreaction in relativistic cosmology*, *Phys. Rev. D* **86** (2012) 043506 [1203.6478].

[4] A. Einstein, *The Field Equations of Gravitation*, *Sitzungsber. Preuss. Akad. Wiss. Berlin (Math. Phys.)* **1915** (1915) 844.

[5] K. Schwarzschild, *On the Gravitational Field of a Mass Point According to Einstein's Theory*, *Abh. Konigl. Preuss. Akad. Wiss. Berlin (Math. Phys.)* **1916** (1916) 189 [physics/9905030].

[6] H. Reissner, *Über die Eigengravitation des elektrischen Feldes nach der Einsteinschen Theorie*, *Annalen der Physik* **355** (1916) 106.

[7] H. Weyl, *Zur Gravitationstheorie*, *Annalen der Physik* **359** (1917) 117.

[8] G. Nordström, *On the Energy of the Gravitation field in Einstein's Theory*, *Koninklijke Nederlandse Akademie van Wetenschappen Proceedings Series B Physical Sciences* **20** (1918) 1238.

[9] R. P. Kerr, *Gravitational field of a spinning mass as an example of algebraically special metrics*, *Phys. Rev. Lett.* **11** (1963) 237.

[10] F. W. Dyson, A. S. Eddington and C. Davidson, *A Determination of the Deflection of Light by the Sun's Gravitational Field, from Observations Made at the Total Eclipse of May 29, 1919*, *Philosophical Transactions of the Royal Society of London Series A* **220** (1920) 291.

[11] LIGO Scientific and Virgo collaboration, B. P. Abbott et al., *Observation of gravitational waves from a binary black hole merger*, *Phys. Rev. Lett.* **116** (2016) 061102.

[12] LIGO Scientific and Virgo collaboration, B. P. Abbott et al., *Gw170817: Observation of gravitational waves from a binary neutron star inspiral*, *Phys. Rev. Lett.* **119** (2017) 161101.

[13] E. Hubble, *A relation between distance and radial velocity among extra-galactic nebulae*, *Proceedings of the National Academy of Sciences* **15** (1929) 168.

[14] A. Friedmann, *Über die Krümmung des Raumes*, *Zeitschrift fur Physik* **10** (1922) 377.

[15] G. Lemaître, *Un Univers homogène de masse constante et de rayon croissant rendant compte de la vitesse radiale des nébuleuses extra-galactiques*, *Annales de la Société Scientifique de Bruxelles* **47** (1927) 49.

[16] H. P. Robertson, *Kinematics and World-Structure*, *ApJ* **82** (1935) 284.

[17] A. G. Walker, *On Milne's Theory of World-Structure*, *Proceedings of the London Mathematical Society, (Series 2)* **42** (1937) 90.

[18] D. W. Hogg et al., *Cosmic homogeneity demonstrated with luminous red galaxies*, *Astrophys. J.* **624** (2005) 54 [astro-ph/0411197].

[19] BOSS collaboration, S. Alam et al., *The clustering of galaxies in the completed SDSS-III Baryon Oscillation Spectroscopic Survey: cosmological analysis of the DR12 galaxy sample*, *Mon. Not. Roy. Astron. Soc.* **470** (2017) 2617 [1607.03155].

[20] DES collaboration, T. M. C. Abbott et al., *Dark Energy Survey year 1 results: Cosmological constraints from galaxy clustering and weak lensing*, *Phys. Rev. D* **98** (2018) 043526 [1708.01530].

[21] Planck collaboration, Y. Akrami et al., *Planck 2018 results. I. Overview and the cosmological legacy of Planck*, 1807.06205.

[22] Supernova Cosmology Project collaboration, S. Perlmutter et al., *Measurements of Omega and Lambda from 42 high redshift supernovae*, *Astrophys. J.* **517** (1999) 565 [astro-ph/9812133].

[23] Supernova Search Team collaboration, A. G. Riess et al., *Observational evidence from supernovae for an accelerating universe and a cosmological constant*, *Astron. J.* **116** (1998) 1009 [astro-ph/9805201].

[24] LIGO Scientific, Virgo, 1M2H, Dark Energy Camera GW-E, DES, DLT40, Las Cumbres Observatory, VINROUGE, Master collaboration, B. P. Abbott et al., *A gravitational-wave standard siren measurement of the Hubble constant*, *Nature* **551** (2017) 85 [1710.05835].

[25] W. L. Freedman, *Cosmology at a Crossroads*, *Nat. Astron.* **1** (2017) 0121 [1706.02739].

[26] A. Del Popolo and M. Le Delliou, *Small scale problems of the ΛCDM model: a short review*, *Galaxies* **5** (2017) 17 [1606.07790].

[27] S. R. Green and R. M. Wald, *How well is our universe described by an FLRW model?*, *Class. Quant. Grav.* **31** (2014) 234003 [1407.8084].

[28] T. Buchert et al., *Is there proof that backreaction of inhomogeneities is irrelevant in cosmology?*, *Class. Quant. Grav.* **32** (2015) 215021 [1505.07800].

[29] S. R. Green and R. M. Wald, *Comments on Backreaction*, 1506.06452.

[30] N. Kaiser, *Why there is no Newtonian backreaction*, *Mon. Not. Roy. Astron. Soc.* **469** (2017) 744 [1703.08809].

[31] T. Buchert, *On Backreaction in Newtonian cosmology*, *Mon. Not. Roy. Astron. Soc.* **473** (2018) L46 [1704.00703].

[32] "Euclid collaboration." http://sci.esa.int/euclid,.

[33] "Lsst collaboration." http://www.lsst.org,.

[34] V. A. A. Sanghai, P. Fleury and T. Clifton, *Ray tracing and Hubble diagrams in post-Newtonian cosmology*, *JCAP* **1707** (2017) 028 [1705.02328].

[35] J. Durk and T. Clifton, *A quasi-static approach to structure formation in black hole universes*, *JCAP* **10** (2017) 012 [1707.08056].

[36] J. Durk and T. Clifton, *Exact Initial Data for Black Hole Universes with a Cosmological Constant*, *Class. Quant. Grav.* **34** (2017) 065009 [1610.05635].

[37] R. Bibi, T. Clifton and J. Durk, *Cosmological Solutions with Charged Black Holes*, *Gen. Rel. Grav.* **49** (2017) 98 [1705.01892].

[38] J. Durk and T. Clifton, *Discrete Cosmological Models in the Brans-Dicke Theory of Gravity*, 1903.03043.

[39] C. M. Will, *The Confrontation between General Relativity and Experiment*, *Living Reviews in Relativity* **17** (2014) 4 [1403.7377].

[40] S. M. Carroll, *Lecture notes on general relativity*, gr-qc/9712019.

[41] R. M. Wald, *General relativity*. Chicago Univ. Press, 1984, 10.7208/chicago/9780226870373.001.0001.

[42] B. Schutz, *A First Course in General Relativity*. Cambridge University Press, 2nd ed., 2009, 10.1017/CBO9780511984181.

[43] C. M. Will, *Theory and Experiment in Gravitational Physics*. 1993, 10.1017/CBO9780511564246.

[44] G. F. R. Ellis, R. Maartens and M. A. H. MacCallum, *Relativistic Cosmology*. 2012, 10.1017/CBO9781139014403.

[45] G. D. Birkhoff and R. E. Langer, *Relativity and modern physics*. 1923.

[46] T. Clifton, P. G. Ferreira, A. Padilla and C. Skordis, *Modified Gravity and Cosmology*, *Phys. Rept.* **513** (2012) 1 [1106.2476].

[47] D. Lovelock, *The Einstein Tensor and Its Generalizations*, *Journal of Mathematical Physics* **12** (1971) 498.

[48] D. Lovelock, *The Four-Dimensionality of Space and the Einstein Tensor*, *Journal of Mathematical Physics* **13** (1972) 874.

[49] A. Joyce, B. Jain, J. Khoury and M. Trodden, *Beyond the Cosmological Standard Model*, *Phys. Rept.* **568** (2015) 1 [1407.0059].

[50] P. Jordan, *Formation of the Stars and Development of the Universe*, *Nature* **164** (1949) 637.

[51] P. Jordan, *The present state of Dirac's cosmological hypothesis*, *Z. Phys.* **157** (1959) 112.

[52] C. Brans and R. H. Dicke, *Mach's principle and a relativistic theory of gravitation*, *Phys. Rev.* **124** (1961) 925.

[53] P. G. Bergmann, *Comments on the scalar-tensor theory*, *International Journal of Theoretical Physics* **1** (1968) 25.

[54] R. V. Wagoner, *Scalar-tensor theory and gravitational waves*, *Phys. Rev. D* **1** (1970) 3209.

[55] K. Nordtvedt, Jr., *Post-Newtonian Metric for a General Class of Scalar-Tensor Gravitational Theories and Observational Consequences.*, *ApJ* **161** (1970) 1059.

[56] J. Polchinski, *String theory. Vol. 1: An introduction to the bosonic string*, Cambridge Monographs on Mathematical Physics. Cambridge University Press, 2007, 10.1017/CBO9780511816079.

[57] G. W. Horndeski, *Second-order scalar-tensor field equations in a four-dimensional space*, *International Journal of Theoretical Physics* **10** (1974) 363.

[58] J.-P. Uzan, *The fundamental constants and their variation: observational and theoretical status*, *Rev. Mod. Phys.* **75** (2003) 403.

[59] J.-P. Uzan, *Varying constants, gravitation and cosmology*, *Living Reviews in Relativity* **14** (2011) 2.

[60] S. Weinberg, *Gravitation and Cosmology: Principles and Applications of the General Theory of Relativity*. New York: Wiley, 1972.

[61] G. Darmois, *Les équations de la gravitation einsteinienne*. Gauthier-Villars, 1927.

[62] A. Lichnerowicz, *L'intégration des équations de la gravitation relativiste et le problème des n corps*, *J. Math. Pures Appl. (9)* **23** (1944) 37.

[63] Y. Fourès-Bruhat, *Sur l'intégration des équations de la relativité générale*, *Journal of Rational Mechanics and Analysis* **5** (1956) 951.

[64] R. Arnowitt, S. Deser and C. W. Misner, *Republication of: The dynamics of general relativity*, *General Relativity and Gravitation* **40** (2008) 1997.

[65] Y. Choquet-Bruhat and R. Geroch, *Global aspects of the cauchy problem in general relativity*, *Comm. Math. Phys.* **14** (1969) 329.

[66] Y. Choquet-Bruhat and J. W. York, Jr., *The Cauchy Problem*, in *General Relativity and Gravitation*. (A. Held, ed.), vol. 1, p. 99, 1980.

[67] J. A. V. Kroon, *Conformal Methods in General Relativity*. Cambridge University Press, 2016, 10.1017/CBO9781139523950.

[68] J. Valiente Kroon, "Mathematical problems of general relativity." Queen Mary University of London, London Taught Course Centre, London Mathematical Society, 2013, http://www.maths.qmul.ac.uk/~jav/LTCC.htm.

[69] J. W. York, *Gravitational degrees of freedom and the initial-value problem*, *Phys. Rev. Lett.* **26** (1971) 1656.

[70] J. W. York, *Conformal "thin-sandwich" data for the initial-value problem of general relativity*, *Phys. Rev. Lett.* **82** (1999) 1350.

[71] S. Hisa-aki, "Introduction to numerical relativity." Computational Science Division, The Institute of Physical and Chemical Research (RIKEN), Japan, APCTP Winter School Lecture on Gravitation and Cosmology, 2003, http://www.oit.ac.jp/is/shinkai/lecture/winterAPCTP/index.html.

[72] R. Bartnik and J. Isenberg, *The Constraint equations*, in *50 Years of the Cauchy Problem in General Relativity: Summer School on Mathematical Relativity and Global Properties of Solutions of Einstein's Equations*, 2002, gr-qc/0405092.

[73] J. Isenberg, R. Mazzeo and D. Pollack, *Gluing and wormholes for the Einstein constraint equations*, *Commun. Math. Phys.* **231** (2002) 529 [gr-qc/0109045].

[74] J. Isenberg, R. Mazzeo and D. Pollack, *On the topology of vacuum space-times*, *Annales Henri Poincare* **4** (2003) 369 [gr-qc/0206034].

[75] P. T. Chrusciel and E. Delay, *Existence of nontrivial, vacuum, asymptotically simple space-times*, *Class. Quant. Grav.* **19** (2002) L71 [gr-qc/0203053].

[76] J. Corvino, *Scalar Curvature Deformation and a Gluing Construction for the Einstein Constraint Equations*, *Communications in Mathematical Physics* **214** (2000) 137.

[77] J. Corvino and R. M. Schoen, *On the Asymptotics for the Vacuum Einstein Constraint Equations*, *J. Differential Geom.* **73** (2006) 185.

[78] A. Butscher, *Exploring the conformal constraint equations*, *The conformal structure of space-time: Geometry, analysis, numerics, Lect. Notes Phys.* **604** (2002) 195 [gr-qc/0111043].

[79] H. Friedrich, *Cauchy problems for the conformal vacuum field equations in general relativity*, *Communications in Mathematical Physics* **91** (1983) 445.

[80] J. A. V. Kroon and J. L. Williams, *A perturbative approach to the construction of initial data on compact manifolds*, 1801.07289.

[81] H. van Elst and C. Uggla, *General relativistic (1+3) orthonormal frame approach revisited*, *Class. Quant. Grav.* **14** (1997) 2673 [gr-qc/9603026].

[82] T. Clifton, D. Gregoris, K. Rosquist and R. Tavakol, *Exact Evolution of Discrete Relativistic Cosmological Models*, *JCAP* **1311** (2013) 010 [1309.2876].

[83] M. Shibata, *Apparent horizon finder for a special family of spacetimes in 3d numerical relativity*, *Phys. Rev. D* **55** (1997) 2002.

[84] A. Krasiński, *Inhomogeneous Cosmological Models*. Cambridge University Press, London, 1997, 10.1017/CBO9780511721694.

[85] H. Stephani, D. Kramer, M. MacCallum, C. Hoenselaers and E. Herlt, *Exact Solutions of Einstein's Field Equations*, Cambridge Monographs on Mathematical Physics. Cambridge University Press, 2nd ed., 2003, 10.1017/CBO9780511535185.

[86] V. Sanghai, *Post-Newtonian Gravity in Cosmology*, Ph.D. thesis, Queen Mary University of London, 2017.

[87] G. F. R. Ellis and H. van Elst, *Cosmological models: Cargese lectures 1998*, *NATO Sci. Ser. C* **541** (1999) 1 [gr-qc/9812046].

[88] K. Bolejko, A. Krasiński, C. Hellaby and M.-N. Célérier, *Structures in the Universe by Exact Methods: Formation, Evolution, Interactions*, Cambridge Monographs on Mathematical Physics. Cambridge University Press, 2009, 10.1017/CBO9780511657405.

[89] C. Hellaby, G. F. R. Ellis and N. Mustapha, *Large-scale inhomogeneity versus source evolution: can we distinguish them observationally?*, *Monthly Notices of the Royal Astronomical Society* **292** (1997) 817.

[90] V. Marra and A. Notari, *Observational constraints on inhomogeneous cosmological models without dark energy*, *Class. Quant. Grav.* **28** (2011) 164004 [1102.1015].

[91] P. Szekeres, *A class of inhomogeneous cosmological models*, *Communications in Mathematical Physics* **41** (1975) 55.

[92] R. A. Sussman and K. Bolejko, *A novel approach to the dynamics of Szekeres dust models*, *Class. Quant. Grav.* **29** (2012) 065018 [1109.1178].

[93] K. Bolejko, M.-N. Célérier and A. Krasinski, *Inhomogeneous cosmological models: Exact solutions and their applications*, *Class. Quant. Grav.* **28** (2011) 164002 [1102.1449].

[94] W. B. Bonnor and A. Chamorro, *Models of voids in the expanding universe*, *ApJ* **361** (1990) 21.

[95] M. Harwit, *Cosmic curvature and condensation*, *ApJ* **392** (1992) 394.

[96] P. Fleury, *Swiss-cheese models and the Dyer-Roeder approximation*, *JCAP* **1406** (2014) 054 [1402.3123].

[97] G. C. McVittie, *The mass-particle in an expanding universe*, *MNRAS* **93** (1933) 325.

[98] B. C. Nolan, *A point mass in an isotropic universe: II. Global properties*, *Classical and Quantum Gravity* **16** (1999) 1227.

[99] N. Kaloper, M. Kleban and D. Martin, *McVittie's Legacy: Black Holes in an Expanding Universe*, *Phys. Rev. D* **81** (2010) 104044 [1003.4777].

[100] T. Clifton, *Cosmology Without Averaging*, *Class. Quant. Grav.* **28** (2011) 164011 [1005.0788].

[101] A. Einstein and E. G. Straus, *The influence of the expansion of space on the gravitation fields surrounding the individual stars*, *Rev. Mod. Phys.* **17** (1945) 120.

[102] A. Einstein and E. G. Straus, *Corrections and additional remarks to our paper: The influence of the expansion of space on the gravitation fields surrounding the individual stars*, *Rev. Mod. Phys.* **18** (1946) 148.

[103] P. Fleury, *Light Propagation in Inhomogeneous and Anisotropic Cosmologies*, Ph.D. thesis, Institut d'astrophysique de Paris, 2015.

[104] S. D. Majumdar, *A Class of Exact Solutions of Einstein's Field Equations*, *Phys. Rev.* **72** (1947) 390.

[105] A. Papapetrou, *A static solution of the equations of the gravitational field for an arbitrary charge-distribution*, *Proceedings of the Royal Irish Academy. Section A: Mathematical and Physical Sciences* **51** (1945) 191.

[106] J. B. Hartle and S. W. Hawking, *Solutions of the Einstein-Maxwell equations with many black holes*, *Communications in Mathematical Physics* **26** (1972) 87.

[107] D. Kastor and J. H. Traschen, *Cosmological multi - black hole solutions*, *Phys. Rev. D* **47** (1993) 5370 [hep-th/9212035].

[108] W. B. Bonnor, *Non-radiative spacetimes*, *Classical and Quantum Gravity* **17** (2000) 3935.

[109] M. Čermák and M. Zouhar, *Cosmologically inspired Kastor-Traschen solution*, *Phys. Rev. D* **89** (2014) 084024 [1307.7508].

[110] W. Israel and K. A. Khan, *Collinear particles and bondi dipoles in general relativity*, *Il Nuovo Cimento (1955-1965)* **33** (1964) 331.

[111] O. J. C. Dias and J. P. S. Lemos, *Pair of accelerated black holes in anti-de Sitter background: AdS C-metric*, *Phys. Rev. D* **67** (2003) 064001 [hep-th/0210065].

[112] R. C. Myers, *Higher-dimensional black holes in compactified space-times*, *Phys. Rev. D* **35** (1987) 455.

[113] R. Emparan and H. S. Reall, *Generalized Weyl solutions*, *Phys. Rev. D* **65** (2002) 084025 [hep-th/0110258].

[114] D. Korotkin and H. Nicolai, *A Periodic analog of the Schwarzschild solution*, gr-qc/9403029.

[115] D. J. Fixsen, *The temperature of the cosmic microwave background*, *The Astrophysical Journal* **707** (2009) 916.

[116] A. Paranjape, *The Averaging Problem in Cosmology*, Ph.D. thesis, TIFR, Mumbai, Dept. Astron. Astrophys., 2009. 0906.3165.

[117] D. L. Wiltshire, *What is dust? - Physical foundations of the averaging problem in cosmology*, *Class. Quant. Grav.* **28** (2011) 164006 [1106.1693].

[118] C. Clarkson, G. Ellis, J. Larena and O. Umeh, *Does the growth of structure affect our dynamical models of the universe? The averaging, backreaction and fitting problems in cosmology*, *Rept. Prog. Phys.* **74** (2011) 112901 [1109.2314].

[119] T. Buchert, *On average properties of inhomogeneous fluids in general relativity I. Dust cosmologies*, *Gen. Rel. Grav.* **32** (2000) 105 [gr-qc/9906015].

[120] T. Buchert, *On average properties of inhomogeneous fluids in general relativity II: Perfect fluid cosmologies*, *Gen. Rel. Grav.* **33** (2001) 1381 [gr-qc/0102049].

[121] T. Buchert, *Is Dark Energy Simulated by Structure Formation in the Universe?*, *Proceedings of Science* **335** (2018) 038 [1810.09188].

[122] K. Bolejko and M. Korzyński, *Inhomogeneous cosmology and backreaction: Current status and future prospects*, *Int. J. Mod. Phys.* **D26** (2017) 1730011 [1612.08222].

[123] K. Bolejko, *Relativistic numerical cosmology with Silent Universes*, *Class. Quant. Grav.* **35** (2018) 024003 [1708.09143].

[124] K. Bolejko, *Evolution of cosmic structures in different environments in the quasispherical Szekeres model*, *Phys. Rev. D* **75** (2007) 043508 [astro-ph/0610292].

[125] R. A. Sussman, I. Delgado Gaspar and J. C. Hidalgo, *Coarse-grained description of cosmic structure from Szekeres models*, *JCAP* **1603** (2016) 012 [1507.02306].

[126] R. A. Sussman and I. Delgado Gaspar, *Multiple nonspherical structures from the extrema of Szekeres scalars*, *Phys. Rev. D* **92** (2015) 083533 [1508.03127].

[127] R. A. Sussman, J. C. Hidalgo, I. Delgado Gaspar and G. Germán, *Nonspherical Szekeres models in the language of cosmological perturbations*, *Phys. Rev. D* **95** (2017) 064033 [1701.00819].

[128] S. Nájera and R. A. Sussman, *Geometric and physical properties of closed ever expanding dust models*, *Gen. Rel. Grav.* **50** (2018) 94 [1804.06944].

[129] E. Bentivegna, T. Clifton, J. Durk, M. Korzyński and K. Rosquist, *Black-Hole Lattices as Cosmological Models*, *Class. Quant. Grav.* **35** (2018) 175004 [1801.01083].

[130] M. Korzyński, *Nonlinear effects of general relativity from multiscale structure*, *Class. Quant. Grav.* **32** (2015) 215013 [1412.3865].

[131] E. Bentivegna and M. Bruni, *Effects of nonlinear inhomogeneity on the cosmic expansion with numerical relativity*, *Phys. Rev. Lett.* **116** (2016) 251302 [1511.05124].

[132] H. J. Macpherson, P. D. Lasky and D. J. Price, *Inhomogeneous Cosmology with Numerical Relativity*, *Phys. Rev. D* **95** (2017) 064028 [1611.05447].

[133] H. J. Macpherson, P. D. Lasky and D. J. Price, *The trouble with Hubble: Local versus global expansion rates in inhomogeneous cosmological simulations with numerical relativity*, *Astrophys. J.* **865** (2018) [1807.01714].

[134] H. Macpherson, D. J. Price and P. D. Lasky, *Einstein's Universe: Cosmological structure formation in numerical relativity*, 1807.01711.

[135] J. T. Giblin, J. B. Mertens and G. D. Starkman, *Departures from the Friedmann-Lemaitre-Robertston-Walker Cosmological Model in an Inhomogeneous Universe: A Numerical Examination*, *Phys. Rev. Lett.* **116** (2016) 251301 [1511.01105].

[136] J. B. Mertens, J. T. Giblin and G. D. Starkman, *Integration of inhomogeneous cosmological spacetimes in the BSSN formalism*, *Phys. Rev. D* **93** (2016) 124059 [1511.01106].

[137] J. Adamek, D. Daverio, R. Durrer and M. Kunz, *General relativity and cosmic structure formation*, *Nature Phys.* **12** (2016) 346 [1509.01699].

[138] J. Adamek, D. Daverio, R. Durrer and M. Kunz, *gevolution: a cosmological N-body code based on General Relativity*, *JCAP* **1607** (2016) 053 [1604.06065].

[139] J. Adamek, C. Clarkson, L. Coates, R. Durrer and M. Kunz, *Bias and scatter in the Hubble diagram from cosmological large-scale structure*, 1812.04336.

[140] W. E. East, R. Wojtak and T. Abel, *Comparing Fully General Relativistic and Newtonian Calculations of Structure Formation*, *Phys. Rev. D* **97** (2018) 043509 [1711.06681].

[141] J.-P. Bruneton and J. Larena, *Dynamics of a lattice Universe: The dust approximation in cosmology*, *Class. Quant. Grav.* **29** (2012) 155001 [1204.3433].

[142] V. A. A. Sanghai and T. Clifton, *Post-Newtonian Cosmological Modelling*, *Phys. Rev. D* **91** (2015) 103532 [1503.08747].

[143] V. A. A. Sanghai and T. Clifton, *Cosmological backreaction in the presence of radiation and a cosmological constant*, *Phys. Rev. D* **94** (2016) 023505 [1604.06345].

[144] V. A. A. Sanghai and T. Clifton, *Parameterized Post-Newtonian Cosmology*, *Class. Quant. Grav.* **34** (2017) 065003 [1610.08039].

[145] J.-P. Bruneton and J. Larena, *Observables in a lattice Universe: the cosmological fitting problem*, *Classical and Quantum Gravity* **30** (2013) 025002 [1208.1411].

[146] P. Fleury, H. Dupuy and J.-P. Uzan, *Interpretation of the Hubble diagram in a nonhomogeneous universe*, *Phys. Rev. D* **87** (2013) 123526 [1302.5308].

[147] P. Fleury, J. Larena and J.-P. Uzan, *The theory of stochastic cosmological lensing*, *JCAP* **1511** (2015) 022 [1508.07903].

[148] T. Clifton and P. G. Ferreira, *Archipelagian Cosmology: Dynamics and Observables in a Universe with Discretized Matter Content*, *Phys. Rev. D* **80** (2009) 103503 [0907.4109].

[149] E. Bentivegna, M. Korzyński, I. Hinder and D. Gerlicher, *Light propagation through black-hole lattices*, *JCAP* **1703** (2017) 014 [1611.09275].

[150] R. W. Lindquist and J. A. Wheeler, *Dynamics of a Lattice Universe by the Schwarzschild-Cell Method*, *Rev. Mod. Phys.* **29** (1957) 432.

[151] H. M. S. Coxeter, *Regular Polytopes*. Methuen and Company Ltd., London, 1948.

[152] C. W. Misner, *The method of images in geometrostatics*, *Annals of Physics* **24** (1963) 102.

[153] J. A. Wheeler, *The geometrostatic lattice cell*, *Foundations of Physics* **13** (1983) 161.

[154] T. Clifton, D. Gregoris and K. Rosquist, *The Magnetic Part of the Weyl Tensor, and the Expansion of Discrete Universes*, *Gen. Rel. Grav.* **49** (2017) 30 [1607.00775].

[155] T. Clifton, B. Carr and A. Coley, *Persistent Black Holes in Bouncing Cosmologies*, *Class. Quant. Grav.* **34** (2017) 135005 [1701.05750].

[156] B. Carr, T. Clifton and A. Coley, *Black holes as echoes of previous cosmic cycles*, 1704.02919.

[157] C.-M. Yoo, H. Abe, K.-i. Nakao and Y. Takamori, *Black Hole Universe: Construction and Analysis of Initial Data*, *Phys. Rev. D* **86** (2012) 044027 [1204.2411].

[158] E. Bentivegna and M. Korzyński, *Evolution of a family of expanding cubic black-hole lattices in numerical relativity*, *Class. Quant. Grav.* **30** (2013) 235008 [1306.4055].

[159] M. Korzyński, *Backreaction and continuum limit in a closed universe filled with black holes*, *Class. Quant. Grav.* **31** (2014) 085002 [1312.0494].

[160] I. Bengtsson and I. Galstyan, *Black Hole Lattices Under the Microscope*, *Class. Quant. Grav.* **35** (2018) 145004 [1802.10396].

[161] S. W. Jolin and K. Rosquist, *Analytic Analysis of Irregular Discrete Universes*, *Gen. Rel. Grav.* **50** (2018) 115 [1802.07135].

[162] E. Bentivegna and M. Korzyński, *Evolution of a periodic eight-black-hole lattice in numerical relativity*, *Class. Quant. Grav.* **29** (2012) 165007 [1204.3568].

[163] S. Räsänen, *Structure formation as an alternative to dark energy and modified gravity*, *EAS Publ. Ser.* **36** (2009) 63 [0811.2364].

[164] A. Čadež, *Apparent horizons in the two-black-hole problem*, *Annals of Physics* **83** (1974) 449.

[165] L. P. Eisenhart, *Riemannian Geometry*. Princeton University Press, 1964.

[166] D. R. Brill and R. W. Lindquist, *Interaction energy in geometrostatics*, *Phys. Rev.* **131** (1963) 471.

[167] T. Clifton, *The Method of Images in Cosmology*, *Class. Quant. Grav.* **31** (2014) 175010 [1405.3197].

[168] T. Clifton, *What's the matter in cosmology?*, *MG14 Proceedings* **3** (2017) 2274 [1509.06682].

[169] C.-M. Yoo and H. Okawa, *Black hole universe with a cosmological constant*, *Phys. Rev. D* **89** (2014) 123502 [1404.1435].

[170] F. Estabrook, H. Wahlquist, S. Christensen, B. DeWitt, L. Smarr and E. Tsiang, *Maximally slicing a black hole*, *Phys. Rev. D* **7** (1973) 2814.

[171] K.-i. Nakao, K.-i. Maeda, T. Nakamura and K.-i. Oohara, *Constant-mean-curvature slicing of the Schwarzschild-de Sitter space-time*, *Phys. Rev. D* **44** (1991) 1326.

[172] R. Moradi, C. Stahl, J. Firouzjaee and S.-S. Xue, *Charged cosmological black hole*, *Phys. Rev. D* **96** (2017) 104007 [1705.04168].

[173] R. Bibi, T. Feroze and A. A. Siddiqui, *Solution of the Einstein - Maxwell equations with anisotropic negative pressure as a potential model of a dark energy star*, *Canadian Journal of Physics* **94** (2016) 758.

[174] D. Bancel and Y. Choquet-Bruhat, *Existence, uniqueness, and local stability for the Einstein-Maxwell-Boltzman system*, *Communications in Mathematical Physics* **33** (1973) 83.

[175] Y. Fujii and K. Maeda, *The scalar-tensor theory of gravitation*, Cambridge Monographs on Mathematical Physics. Cambridge University Press, 2007, 10.1017/CBO9780511535093.

[176] T. Clifton, D. F. Mota and J. D. Barrow, *Inhomogeneous gravity*, *Mon. Not. Roy. Astron. Soc.* **358** (2005) 601 [gr-qc/0406001].

[177] V. Faraoni and S. D. Belknap-Keet, *New inhomogeneous universes in scalar-tensor and f(R) gravity*, *Phys. Rev. D* **96** (2017) 044040 [1705.05749].

[178] G. Papallo and H. S. Reall, *On the local well-posedness of Lovelock and Horndeski theories*, *Phys. Rev.* **D96** (2017) 044019 [1705.04370].

[179] M. Salgado, *The Cauchy problem of scalar tensor theories of gravity*, *Class. Quant. Grav.* **23** (2006) 4719 [gr-qc/0509001].

[180] H. Dehnen and O. Obregón, *Exact cosmological solutions in Brans and Dicke's scalar-tensor theory, II*, **15** (1972) 326.

[181] B. Bertotti, L. Iess and P. Tortora, *A test of general relativity using radio links with the Cassini spacecraft*, *Nature* **425** (2003) 374.

[182] S. Sikora and K. Głód, *Example of an inhomogeneous cosmological model in the context of backreaction*, *Phys. Rev. D* **95** (2017) 063517 [1612.03604].